UNIVERSITY OF SILESIA IN KATOWICE

FACULTY OF NATURAL SCIENCES

Institute of Earth Sciences

JANUSZ GODZIEK

ANALYSIS AND MODELING OF REMOTE SENSING DATA TO AUTOMATE THE DETECTION OF WINDTHROWS, ROOT PLATES OF FALLEN TREES, AND PIT-MOUND TOPOGRAPHY

Doctoral Dissertation

Supervisor: Dr. hab. Łukasz Pawlik, Prof. UŚ

Auxiliary supervisor: Dr. Brian Buma

SOSNOWIEC 2025

I would like to thank:

Dr. hab. Łukasz Pawlik, prof. UŚ

for his constant support and inspiration, sharing research ideas and projects, inviting for different cooperations

Dr. Brian Buma

for his great support, knowledge sharing and invaluable help during my research internship in the U.S.

My wife and family

for their unconditional support and understanding

Janusz Godziek acknowledges the financial support of the project by National Science Centre, Poland (grant no. 2019/35/O/ST10/00032), and by the National Agency for Academic Exchange, Poland (agreement no. PPN/STA/2021/1/00081/U/00001)

Table of contents

Papers included in the doctoral dissertation

1. **Godziek J.**, Pawlik Ł., Buma B., 2025: The Mapping and Analysis of the Infrequent, Large-Scale Blowdown Event in the Colorado Front Range. Land Degradation & Development, 36(10), 3604-3620. https://doi.org/10.1002/ldr.5623 – *200 pts. Ministry of Science and Higher Education; IF: 3.7*

2. **Godziek J.**, 2024: Root plates of uprooted trees− Automatic detection and biotransport estimation using LiDAR data and field mapping. International Journal of Applied Earth Observation and Geoinformation, 131, 103992. https://doi.org/10.1016/10.1016/j.jag.2024.103992 - *140 pts. Ministry of Science and Higher Education; IF: 8.6*

3. **Godziek J.**, Pawlik Ł., 2023: Indicators of wind-driven forest disturbances–pit–mound topography, its automatic detection and significance. Catena, 221, 106757. https://doi.org/10.1016/j.catena.2022.106757 – *140 pts. Ministry of Science and Higher Education; IF: 5.7*

Other papers with contributions of the PhD student

4. Pawlik Ł., **Godziek J.**, Zawolik Ł., 2022: Forest Damage by Extra-Tropical Cyclone Klaus-Modeling and Prediction. Forests, 13(12), 1991. https://doi.org/10.3390/f13121991 - *100 pts. Ministry of Science and Higher Education; IF: 2.5*

5. **Godziek J.**, Gaidzik K., 2020: Assessment of tectonic control on the development of low mountains moderate relief in the Outer Carpathians (Southern Poland). Journal of Mountain Science, 17(10), 2297-2320. https://doi.org/10.1007/s11629-020-6121-4 – *70 pts. Ministry of Science and Higher Education; IF: 2.5*

6. **Godziek J.**, Szypuła B., 2020: Durability of forest cover in the Ochotnica Valley (Gorce Mts.) and in the Solinka Valley (Bieszczady Mts.) in the 18th-21st centuries. Geographia Polonica 93(1), 69 - 88. https://doi.org/10.7163/GPol.0163 - *100 pts. Ministry of Science and Higher Education; IF: 1.1*

7. **Godziek J.**, Szypuła B., 2018: A study of changes in forest cover in the Ochotnica Valley in the 19th-20th centuries based on cartographic materials. Dissertations of Cultural Landscape Commision 39(1), 189-206. https://doi.org/10.30450/201811 - *40 pts. Ministry of Science and Higher Education*

Summary

The formation of the wind damages (windthrow, blowdown) is controlled primarily by the occurrence of high-speed winds. Due to the strong wind impact, the tree can be broken or uprooted. In the 1st type of tree mortality, there are only minor geomorphic and pedogenic consequences. In the 2nd type of tree mortality, some of the soil material attached to its root system is lifted and deposited on the ground surface in the form of a root plate. These forms are unstable and subsequently deteriorate, leading to the formation of pit-mound topography, i.e., adjacent pit-mound pairs of various density per ha, where each pair represents remnants of one root plate. The tree uprooting process and its outcomes can be considered an expression of biomorphodynamics, i.e., changes in landforms, activity of geomorphological processes, and transport caused by living organisms.

The wind-driven forest damage, together with resulting landforms (root plates, pit-mound topography) can be studied in different spatio-temporal scales, with the use of various techniques and approaches, such as field mapping, soil sampling, geophysics, dendrochronology, and using digital approach through remote sensing (RS). The advantages of employing remote sensing over other approaches are: 1) substantial volume of RS data collected nowadays by national agencies, out of which a large part is available in an open domain, 2) the RS data consistency supporting a large variety of strategies, workflows, and analytical and modeling scenarios, and 3) defined intervals of RS data acquisition enabling analysis of the phenomena changeability over time.

The main objective of the thesis is to develop a quantitative and qualitative methodology for using remote sensing data to assess the impact of windthrows on the slope biomorphodynamics. This methodology was proposed for three components required in the analysis of wind-related biomorphodynamics, i.e., windthrow areas, root plates of fallen trees, and pit-mound topography. The author tested whether the RS data can be effectively applied to map these components with a high spatial precision, on the level of accuracy enabling to decipher the environmental aspects of the wind - trees - relief and soils interactions. Research was carried out for the mid-latitudes mountainous coniferous forests of the Polish Carpathians (Babia Góra National Park and Gorce National Park) and the American Rocky Mountains (Colorado Front Range).

The blowdown mapping in the Rocky Mountains was based on the change detection using pre- and post-event images. Using the change vector analysis, changes between images are described using two parameters: magnitude, representing the amount of change, and direction, referring to the type of change. The author computed the differential image composed of 12 bands, and then calculated *mgt* and *drct* rasters for 66 possible pairs of differential image bands. Different *mgt* and *drct* thresholds were tested to provide the best possible accuracy and the lowest false positive rate

(FPR). The final result was obtained by combining the direction and magnitude rasters. The most effective output was based on Sentinel-2 band pairs 11 and 12, together with 40° < drct < 47° and mgt > 0.1, having the TPR of 66.04% and FPR of only 0.89%. These results can be adjusted to higher TPR, however this is connected with the FPR increase.

Both root plates and pit-mound detection were based on LiDAR data and the raster models derived from them. For root plates, analyses were carried out in the 0.25 m resolution, while for pit-mound topography three DTMs with resolutions of 0.1, 0.25 and 0.5 m were tested. For root plates, the author created the differential model (DM) representing the height of root plates, fallen trunks, and dense understory vegetation by 1) creating the Digital Surface Model (DSM) through interpolation of the points being the last returns of the laser beam with a normalized height < 2 m, and 2) subtracting the DTM. For both methods the position of forms was extracted using closed contour lines, and applying various classification methods. For treethrow pits and mounds, the objects were labeled basing on the location of the highest and the lowest points within the closed contour line polygons. For root plates, the closed contour line polygons were labelled as "root plates" or "artefacts" using a set of parameters computed for each polygon and comparing multiple filtering rules to select the most effective one. Regarding the biotransport, the author proposed two approaches to estimate the volume of root plates using the above-described differential model. Having the most accurate root plate boundary, the volume was estimated using the contour lines (CNT) or zonal statistics (ZS) approach. The results were validated using root plate volumes calculated based on the field measurements (FM) and the equation for the volume of a half ellipsoid. This allowed to calculate the volume of the soil volume transported within root plates of uprooted trees. All described workflows were automated using R programming language. The root plate detection rate was 79.1%, 71.2% and 70.3% for three investigated 100x100 m study plots, respectively. The root plate volumes computed with the RS-based approaches were in a similar range to the ones estimated using the field data. The mean calculated biotransport was the highest when using ZS, lower for CNT, and the lowest for FM. Pit-mound pairs detection rate was at the level of 90.6% and 85.7% for two study areas, whereas the highest detection rate for pits reached 96.9 – 95.2%, and for mounds – 93.8% - 90.5%.

The methods proposed in this thesis are novel in several aspects, which include: 1) proposing the root plates and pit-mound topography mapping workflows based on LiDAR data, 2) developing the techniques of single root plate volume estimation, based on LiDAR data, 3) implementing the change vector analysis for the blowdown detection for the first time in North America, 4) preparing scripts in R programming language to automate all the workflows, and 5) presenting the detailed exploration and evaluation of factors affecting the quality of these methods outputs. The presented environmental insights contribute to the fields of geomorphology, soil science, and forest ecology through: 1) exploring and explaining the spatial distribution patterns of root plates and pit-mound topography, 2) quantifying the biotransport driven by tree uprooting, and 3) providing the analysis of to-date unexplored 2020 wind event in the Colorado Front Range.

Keywords: windthrow, tree uprooting, biomorphodynamics, LiDAR, Sentinel-2, change vector analysis, R programming

Streszczenie

Powstawanie zniszczeń spowodowanych przez wiatr (wiatrowałów, wiatrołomów) jest przede wszystkim uwarunkowane występowaniem wiatrów o dużej prędkości. Na skutek ich oddziaływania drzewo może zostać złamane lub wyrwane z korzeniami. W pierwszym typie śmiertelności drzew skutki geomorficzne i pedogeniczne są znikome. Natomiast w drugim typie system korzeniowy drzewa wraz z glebą zostaje uniesiony i zdeponowany na powierzchni terenu w postaci wykrotu. Formy te są nietrwałe i z czasem ulegają degradacji, co prowadzi do powstania charakterystycznej topografii kopców i zagłębień – sąsiadujących par form wklęsłych i wypukłych o zróżnicowanym zagęszczeniu na jednostkę powierzchni, z których każda para jest pozostałością po jednym wykrocie. Proces wyrywania drzew z korzeniami oraz jego skutki stanowią przejaw biomorfodynamiki, rozumianej jako zmiany w formach rzeźby terenu, aktywności procesów geomorfologicznych oraz transporcie materiału powodowane przez działalność organizmów żywych.

Zniszczenia w lasach spowodowane przez wiatr, wraz z towarzyszącymi im formami terenu (wykroty, topografia kopców i zagłębień), mogą być badane w różnych skalach przestrzennych i czasowych, przy użyciu zróżnicowanych metod, takich jak kartowanie terenowe, pobór próbek

glebowych, geofizyka, dendrochronologia oraz podejścia cyfrowe, oparte na teledetekcji. Zastosowanie danych teledetekcyjnych oferuje istotne korzyści w porównaniu do innych metod, w tym: 1) duży zasób danych pozyskiwanych obecnie przez instytucje krajowe, z których znaczna część jest publicznie dostępna; 2) wysoka spójność danych umożliwiająca realizację zróżnicowanych strategii badawczych, ścieżek analitycznych i scenariuszy modelowania; oraz 3) regularność pozyskiwania danych, umożliwiająca analizę zmienności zjawisk w czasie.

Celem pracy było opracowanie ilościowej i jakościowej metodologii wykorzystania danych teledetekcyjnych do oceny wpływu wiatrowałów na biomorfodynamikę stoków. Metodologia ta została opracowana dla trzech głównych komponentów istotnych w analizie biomorfodynamiki związanej z działalnością wiatru: obszarów wiatrowałowych, wykrotów oraz topografii kopców i zagłębień. Autor badał, czy dane teledetekcyjne mogą być skutecznie wykorzystane do mapowania wyżej wymienionych elementów z wysoką precyzją przestrzenną i dokładnością wystarczającą do prowadzenia analiz środowiskowych polegających na badaniu zależnośći między wiatrem, drzewami, a rzeźbą terenu i glebami. Badania przeprowadzono w umiarkowanej strefie klimatycznej, w lasach regla górnego z dominacją świerka w Karpatach Polskich (Babiogórski Park Narodowy i Gorczański Park Narodowy) oraz w lasach świerkowo-sosnowych w Górach Skalistych w USA (Colorado Front Range).

Kartowanie wiatrołomów w Górach Skalistych oparto na analizie zmian na obrazach sprzed zdarzenia i po zdarzeniu. Wykorzystano analizę wektorów zmian (change vector analysis), w której różnice pomiędzy obrazami opisano dwoma parametrami: magnituda (magnitude, mgt), oznaczającą intensywność zmiany, oraz kierunkiem (direction, drct), wskazującym jej charakter. Autor wygenerował obraz różnicowy złożony z 12 pasm spektralnych, a następnie obliczył rastry magnitudy i kierunku dla 66 możliwych par pasm. Testowano różne progi wartości mgt i drct w celu uzyskania jak najwyższej dokładności i minimalnego odsetka fałszywie pozytywnych detekcji (FPR). Ostateczny wynik uzyskano przez połączenie rastrów kierunku i magnitudy zmian. Najlepsze rezultaty osiągnięto dla pary kanałów Sentinel-2: 11 i 12, przy wartościach $40° < drct < 47°$ oraz $mgt > 0.1$, uzyskując wskaźnik wartości prawdziwie pozytywnych (TPR) równy 66,04% oraz bardzo niski FPR – 0,89%. Zwiększenie TPR jest możliwe, lecz wiąże się z podwyższeniem FPR.

Detekcja wykrotów oraz topografii kopców i zagłębień oparta była na danych LiDAR oraz na wyliczonych na podstawie tych danych modelach rastrowych. Analizę dla wykrotów prowadzono w rozdzielczości 0,25 m, natomiast dla topografii kopców i zagłębień testowano trzy numeryczne modele terenu (NMT) o rozdzielczościach 0,1, 0,25 i 0,5 m. Autor opracował model różnicowy, który uwzględniał wysokość wykrotów, powalonych pni oraz zwartego podszytu, poprzez: 1) utworzenie numerycznego modelu pokrycia terenu (NMPT) na podstawie interpolacji punktów ostatnich odbić impulsów laserowych o znormalizowanej wysokości < 2 m powyżej

powierzchni terenu, oraz 2) odjęcie NMT. Położenie form wyodrębniano na podstawie zamkniętych poziomic, a do klasyfikacji zastosowano różne metody. W przypadku kopców i zagłębień obiekty klasyfikowano w oparciu o lokalizację najwyższych i najniższych punktów w obrębie poligonów zamkniętych poziomic. Dla wykrotów, poligony zamkniętych poziomic klasyfikowano jako „wykroty" lub „artefakty" na podstawie zbioru parametrów wyliczonych dla każdego poligonu oraz zastosowania zestawu reguł filtrujących, w celu wyboru najbardziej efektywnej kombinacji. W kontekście biotransportu, autor zaproponował dwa podejścia do szacowania objętości wykrotów z wykorzystaniem opisanego modelu różnicowego: 1) metodę poziomicową (CNT), 2) podejście oparte na statystyce strefowej (ZS). Wyniki zostały zweryfikowane na podstawie pomiarów terenowych (FM) oraz wzoru na objętość półelipsoidy obrotowej, co pozwoliło oszacować ilość materiału glebowego przemieszczonego w formie wykrotów. Wszystkie etapy analizy zostały zautomatyzowane w języku R. Skuteczność wykrywania wykrotów wyniosła odpowiednio 79,1%, 71,2% i 70,3% dla trzech powierzchni badawczych o wymiarach 100×100 m. Uzyskane objętości były porównywalne z szacunkami opartymi na danych terenowych. Najwyższe wartości biotransportu zostały oszacowane przez metodę ZS, niższe przez metodę CNT, a najniższe przy zastosowaniu pomiarów terenowych (FM). Dokładność wykrywania par kopiec–zagłębienie wyniosła odpowiednio 90,6% i 85,7% dla dwóch analizowanych obszarów, przy czym detekcja samych zagłębień osiągnęła 95,2–96,9%, a kopców – 90,5–93,8%.

Zaprezentowane w pracy metody mają nowatorski charakter w kilku kluczowych aspektach, takich jak: 1) opracowanie sposobów przetwarzania danych LiDAR w celu mapowania wykrotów oraz topografii kopców i zagłębień, 2) opracowanie metod szacowania objętości pojedynczych wykrotów na podstawie danych teledetekcyjnych, 3) pierwsze dla obszaru Ameryki Północnej zastosowanie analizy wektorów zmian do detekcji wiatrołomów, 4) wdrożenie skryptów w języku R automatyzujących całość procesów analitycznych, 5) szczegółowa analiza czynników wpływających na jakość wyników. Wnioski wynikające z przeprowadzonych badań mają istotne znaczenie dla geomorfologii, gleboznawstwa i ekologii lasu, poprzez: 1) zbadanie przestrzennych wzorców rozmieszczenia wykrotów oraz topografii kopców i zagłębień, 2) ilościowe oszacowanie biotransportu spowodowanego wyrywaniem drzew z korzeniami, 3) analizę dotychczas nieopisanego zdarzenia wiatrowego z 2020 roku w rejonie Gór Skalistych w Kolorado, USA.

Słowa kluczowe: obszar wiatrowałowy, wyrywanie drzew z korzeniami, biomorfodynamika, LiDAR, Sentinel-2, analiza wektorów zmian, programowanie w R

Definitions

biomorphodynamics (*pol. biomorfodynamika*) – spatio-temporal changes in landforms, activity of geomorphological processes and soil material transport caused by living organisms (plants, animals, etc.)

biotransport (*pol. biotransport*) – movement of soil induced by living organisms

CVA (change vector analysis) – the method of change detection used to identify spectral changes between two images acquired at different times. CVA characterizes the change by computing the magnitude and direction of change vector. Magnitude corresponds to the amount of change, while direction refers to the type of change.

DSM (Digital Surface Model) – a raster model where pixel values represent the natural and built features on the Earth's surface

DTM (Digital Terrain Model) – a raster model where pixel values represent the ground surface.

LiDAR (Light Detection and Ranging) – the remote sensing technology that works through emitting laser pulses and measuring the time it takes for the reflected light to return

pit-mound topography (also: pit and mound topography, treethrow pit-mound forms; *pol. topografia kopców i zagłębień, rzeźba jamowo-kopczykowa, morfologia wykrotowa*) – the microtopography consisting of multiple pairs of adjacent pit and mound, originating from the tree uprooting; the pit is the place occupied by the tree-root system before uprooting, and the mound is the remnant of the decomposed root plate

point cloud – the set of points in space representing the laser beam reflections; the product of LiDAR scanning

root plate (also: root ball; *pol. wykrot*) – microrelief landform (or forest floor object) consisting of undecomposed tree root system and the attached soil and rock particles

windthrow, blowdown (*pol. obszar wiatrowałowy*) – the forest area with trees damaged by the high-speed wind, either with broken (snapped) or uprooted trees

Introduction

Wind damages (windthrow, blowdown) are among the most frequent and important types of forest disturbances around the world (Seidl et al., 2011; Gardiner, 2021). Their formation is controlled primarily by the occurrence of high-speed winds, related to the passage of low pressure systems (Mitchell, 2013). The key wind-related factors controlling the forest damage are the gust speed, direction and the duration of the strong wind. The spatial distribution of windthrow areas is also connected to other environmental factors, such as abiotic (topography, slope, soil and bedrock type) and biotic (stand type, species, tree height, etc.) (Senf and Seidl, 2021). Due to the strong wind impact, the tree can be broken or uprooted. In the 1st type of tree mortality, there are only minor geomorphic and pedogenic consequences. They include damming of the eroded material from the upper parts of the slope (Pawlik, 2013) and the geochemical changes in the soil profile beneath lying stems due to fungi activity during the stem decomposition (Fall et al., 2022). In the 2nd type of tree mortality, some of the soil material attached to its root system is lifted and deposited on the ground surface in the form of a root plate (Schaetzl et al., 1990; Šamonil et al., 2016). These forms are unstable and subsequently deteriorated, leading to the formation of pit-mound topography, i.e., adjacent pit-mound pairs of various density per ha, where each pair represents remnants of one root plate (Fig. 1) (Schaetzl et al., 1990; Ulanova, 2000). The tree uprooting process and its outcomes can be considered an expression of biomorphodynamics, i.e., changes in landforms, activity of geomorphological processes (Šamonil et al., 2015), and transport caused by living organisms (Phillips et al., 2008; Phillips, 2009). From the point of view of soil science, geomorphology, and forest ecology, these expressions of biomorphodynamics play a crucial environmental role through influencing the soil properties and development, shaping the slope microrelief, and affecting the local conditions of the forest functioning (Schaetzl et al., 1989; Rojan, 2010; Pawlik, 2013). In this context, interactions between fallen trees, soils, and slope microtopography should not be ignored (Fig. 1).

In most cases, wind disturbances interact with other types of forest disturbances, such as insects outbreaks, wildfires, droughts, and intense snowfall (Seidl et al., 2011). Stands affected by insects (e.g., bark beetle) or drought seem to be more likely to be damaged by wind (Havašová et al., 2017). Large volume of coarse woody debris (CWD) being an effect of a windstorm event is a potential fuel source for future wildfires (Kulakowski and Veblen, 2002). CWD presence also influences the forest nutrient cycle, as the dead wood is valuable source of organic carbon and various microelements (Joyce et al., 2019). The blowdown occurrence impacts the plant communities, driving the plant succession processes to its initial stage. Under the impact of environmental stress factors, windthrows may be a triggering mechanism of a forest type or plant community alteration (Kooch et al., 2012),

e.g., leading to transition from spruce monoculture to mixed beech-fir forest in the Polish Carpathians (Zadrożny et al., 2017). A pit-mound topography produced by tree uprooting (treethrow) affects the development of understory vegetation, soil processes, and supports small-scale retention in treethrow pits (Valtera and Schaetzl, 2017). Both root plates and pit-mound topography can act as geomorphic indicators of past wind-driven forest disturbances (Gerlach, 1960; Kotarba, 1970; Schaetzl et al., 1989). In addition, the investigation of root plates and treethrow pits and mounds (their spatial orientation and dimensions) enables reconstruction of wind direction. Estimation of the root plate volume offers an insight into the scale of slope material mobilization and transport due to uprooting (Gabet et al., 2003; Constantine et al., 2012). Considering the spatial distribution of these forms, the relationship between blowdowns and other components of the environment can be investigated (Pawlik, 2013). The tree uprooting process and resulting landforms seem to be strongly impacted by human activity due to forest management, as in managed forests root plates are removed or disturbed. Due to the former forest management in Central Europe, the spruce stands introduced in clear-cut beech-fir stands are more prone to disturbances (Holeksa et al., 2017). In managed forests mature trees are being cut before they reach a size making them very prone to wind damage, preventing the formation of root plates and pit-mound topography. Hence, the occurrence of root plates and pit-mound topography may be an indicator of unmanaged, old-growth forests (Faliński, 1976; Barker Plotkin et al., 2017).

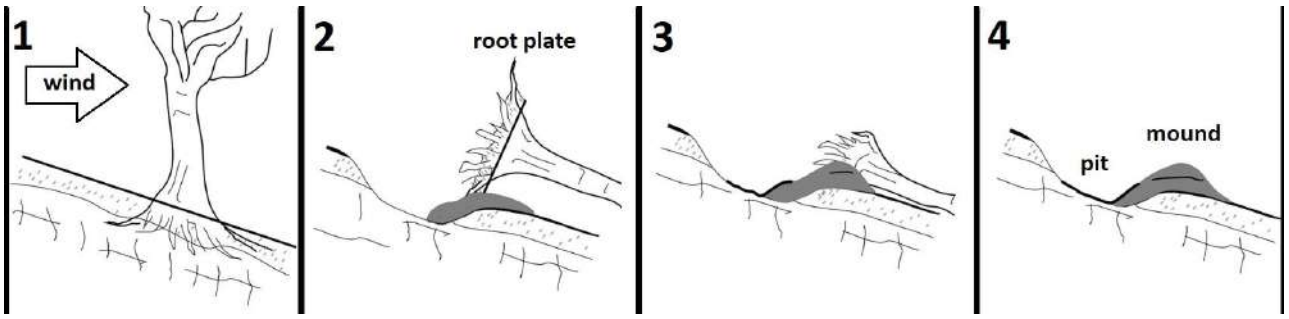

Fig. 1. The functioning of the wind-driven hillslope biomorphodynamics. After: Pawlik, 2013 (modified).

The wind-driven forest damage, together with resulting landforms (root plates, pit-mound topography) can be studied in different spatio-temporal scales with the use of various techniques and approaches, such as field mapping, soil sampling, geophysics, dendrochronology, and using digital approach (Kozak, 2022) through remote sensing (RS). The advantages of employing remote sensing over other approaches are: 1) substantial volume of RS data collected nowadays by national agencies, out of which large part is available in an open domain, 2) the RS data consistency supporting a large variety of strategies, workflows, and analytical and modeling scenarios, and 3) defined

intervals of RS data acquisition enabling to analyse the phenomena changeability over time (Hansen et al., 2013). To effectively analyse the RS data, new methods and detection algorithms and workflows are required. The automatization could enable performing the environmental studies for large areas, in the scale for which taking the fieldwork would take months or years (Hansen et al., 2013; Bonannella et al., 2022). Such an approach would allow to draw wider conclusions than in the case of sampling just several plots. To achieve such objectives, the applied methods should be as accurate as possible. The crucial issue is the output validation and assessment, which can be done using confusion matrices (Dalponte et al., 2020). Testing on smaller areas is required to produce the method applicable for a wide area. Minimizing the share of false positives and false negatives can be achieved by adjusting applied procedures and thresholds (Godziek, 2024).

The complex mapping of windthrows, root plates and pit-mound topography might be done by using custom automatic detection procedure. The assumption of its final output is obtaining the data accurate enough to draw solid environmental conclusions based on them. Such methods and workflows may vary and evolve, and preparing the most precise detection algorithm usually requires several attempts and repetitive evaluation of the obtained output. The automation of these procedures is crucial as enabling the big spatial data processing. Having the accurate detection methods

of blowdowns and related landforms would allow to investigate multiple windthrow-related environmental dependencies in a broad spatiotemporal perspective. An example of RS data that could be employed to detect blowdown areas and landforms are light detection and ranging (LiDAR) point clouds (Wężyk et al., 2019), and optical satellite imagery. These methods of data processing and analysis may involve the change analysis between pre- and post-event images, the heuristic approach based on finding thresholds basing on false positives rate minimalization, and the machine learning approach.

Several examples show that RS data can be applied to detect wind-driven forest damage (Forzieri et al., 2020; Lazecky et al., 2021). Optical satellite data and change vector analysis (CVA) have been applied to map the blowdowns in the Italian Alps, resulting in an accuracy above 80% (Dalponte et al., 2020). This approach has not been tested nor adapted for other forest regions, such as North America. For the Rocky Mountains, to date very little research attention has been paid to blowdown mapping. As the Southern Rockies region is characterized by low cloudiness, CVA together with optical RS data have the potential to be effectively used for windthrow areas mapping.

The RS data have been used to detect forest floor features understory objects. The experiments with LiDAR data processing indicated the possibility of fallen trees detection (Mücke et al., 2012). LiDAR data filtering allowed to detect fallen tree stems (CWD) for the area located in Minnesota, United States, with a detection rate of 23% (Joyce et al., 2019). Small microtopography forms

with similar dimensions to the pit-mound topography can be detected using LiDAR-derived Digital Terrain Models (DTMs) combined with the machine learning-based random forest approach (Niculiță, 2020). These examples show the potential of applying the RS to create automatic detection methods of blowdowns, root plates, and pit-mound topography. Although there have been different attempts for improving the ground classification algorithms for LiDAR data (Zhang et al., 2003, 2016a), no research has been conducted on the possibility of capturing the root plates of fallen trees nor the pit-mound topography using point clouds and their derivatives (elevation models). However, detection of these objects is important from a technical (accurate point cloud classification and conversion to other spatial objects) and the environmental research perspective (studies on the wind impact on the forested hillslopes microrelief). In addition, automation of the detection procedures is crucial for performing analyses in broad spatio-temporal scales.

The main objective of the thesis is to develop a quantitative and qualitative methodology for using remote sensing data to assess the impact of windthrows on the slope biomorphodynamics. This methodology was proposed for three components required in the analysis of wind-related biomorphodynamics, i.e., windthrow areas, root plates of fallen trees, and pit-mound topography. The author tested whether the RS data can be effectively applied to map these components with a high spatial precision, on the level of accuracy enabling to decipher the environmental aspects of the wind - trees - relief and soils interactions.

The methodological objectives of the thesis included:

1) testing and modifying the windthrow detection methods using optical satellite data,
2) proposing and testing the methods supporting the detection of forms resulted from strong wind impact on forest stands (i.e., root plates of fallen trees and pit-mound topography), together with the methods enabling estimation of transported soil-rock material, using the LiDAR data,
3) automation of all developed methods for the potential use in the large spatio-temporal scale analysis,
4) exploring the technical and environmental factors affecting the accuracy of the proposed methods.

As a result of the novel methodological approach presented above for studying windthrow as an environmental and geomorphic slope phenomenon, the following scientific (cognitive) objectives have been outlined:

1) assessment of the spatial distribution of windthrows, root plates, and pit-mound topography within the particular study area, which is crucial in terms of microrelief evolution, soil development, micro-scale hydrological processes, and forest regeneration,
2) quantitative assessment of the wind-driven biotransport, i.e., estimation of the volume of soil-

rock material displaced in root plates.

As an additional component, which is important for hillslope denudation rates assessment and landscape evolution modeling, the author performed time series analysis (meteorological and satellite data) to track the course of the September 2020 Rocky Mountains wind event. Regarding the spatial scope, all research was carried out for the mid-latitudes mountainous coniferous forests of the Polish Carpathians (Babia Góra National Park and Gorce National Park) and the American Rocky Mountains (Colorado Front Range) (Fig. 1 in (Godziek and Pawlik, 2023; Godziek, 2024; Godziek et al., 2025).

Methods

The hillslope biomorphodynamics can be studied using three components of the spatial and temporal scope of the process (Fig. 2). Firstly, windthrow areas should be identified and positioned in time. Secondly, for these areas the recent biotransport could be estimated using LiDAR data and root plates detection. Thirdly, the entire study area should be examined for signs of past biomorphodynamics using the pit-mound mapping approach.

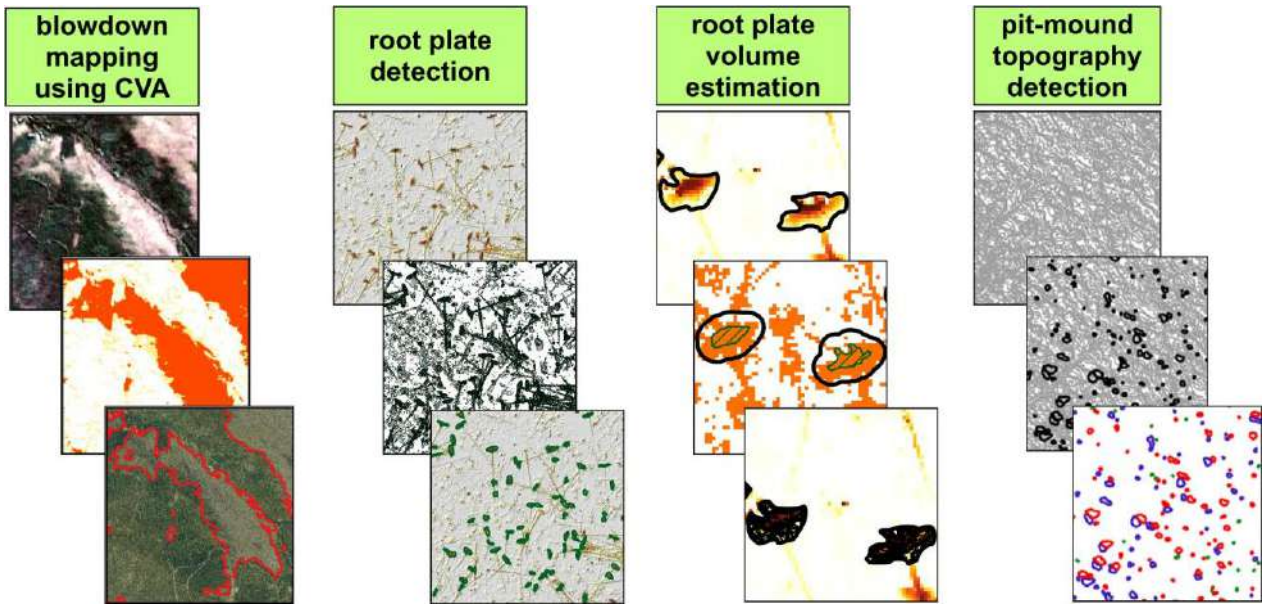

Fig. 2. The remote sensing approaches in the context of wind-driven hillslope biomorphodynamics. After: Godziek et al., 2025, Godziek 2024, Godziek and Pawlik, 2023 (modified).

To the author's best knowledge, the windthrow mapping workflow (Godziek et al., 2025), built upon the study conducted in the Italian Alps (Dalponte et al., 2020), is the first application of the change vector analysis (CVA) method (Solano-Correa et al., 2019) for forest damage detection in the North American context. The proposed approach is: 1) adjustable to study-specific needs like maximizing or minimizing false positives, true negatives, or other goals, and 2) the approach

is entirely based on the open data and scripting language available for future users, which secures the possibility of testing the method in other environmental conditions. The mapping was based on the change detection using pre- and post-event images. Using the CVA, changes between images are described using two parameters: magnitude (*mgt*) representing the amount of change, and direction (*drct*) referring to the type of change. The author computed the differential image composed of 12 bands, and then calculated *mgt* and *drct* rasters for 66 possible pairs of differential image bands. Different *mgt* and *drct* thresholds were tested to provide the best possible accuracy and the lowest false positive rate (FPR). The final result were obtained by combining the direction and magnitude rasters. The results were also compared with the Landsat-based, 30 m resolution Global Forest Change (GFC) dataset to find and describe differences (Godziek et al., 2025).

Both root plates and pit-mound detection were based on LiDAR data and the raster models derived from them. For root plates, analyses were carried out in the 0.25 m resolution, while for pit-mound topography three DTMs with resolutions of 0.1, 0.25 and 0.5 m were tested. For root plates, the author created the differential model (DM) representing the height of root plates, fallen trunks, and dense understory vegetation by: 1) creating the Digital Surface Model (DSM) through interpolation of the points being the last returns of the laser beam with a normalized height < 2 m, and 2) subtracting the DTM. For both methods the position of forms was extracted using closed contour lines. In the case of pit-mound topography, the length of each contour line within each study plot was computed. Then, three contour line intervals (0.05, 0.1 and 0.25 m) and three contour line length intervals (1.5 – 25 m, 2.5 – 20 m, 3.5 – 15 m) were tested. For root plates, the contour lines were delineated basing on the differential model, then selected at three heights (0.5, 1 and 1.5 m), polygonized and aggregated (Fig. 3 in (Godziek, 2024), Fig. 4 in (Godziek and Pawlik, 2023)). The form classification was different in both cases. For treethrow pits and mounds, the objects were labelled as “pit”, “mound”, or “unclassified” basing on the location of the highest and the lowest points within the closed contour line polygons. Then, pit-mound pairs were filtered basing on the distance criterion between adjacent pits and mounds (Fig. 5 in (Godziek and Pawlik, 2023)). For root plates, the closed contour line polygons were labelled as “root plates” or “artefacts” using a set of parameters computed for each polygon and comparing multiple filtering rules to select the most effective one (Tab. 2, Fig. 4 in (Godziek, 2024)). All described workflows were automated using R programming language (R Core Team, 2024).

Regarding the biotransport, the author proposed two approaches to estimate the volume of root plates using the above-described differential model. Having the most accurate root plate boundary, the volume was estimated using contour lines (CNT) or zonal statistics (ZS) approach. The results were validated using root plate volumes calculated based on the field measurements (FM) and the equation for the volume of a half ellipsoid. This allowed to calculate the approximate volume

of the soil transported within root plates of uprooted trees (Godziek, 2024).

To asses these methods performance, various validation strategies and metrics were applied. In the case of the blowdown detection, the true positives rate (TPR) and the false positives rate (FPR) were applied. The validation dataset was randomly distributed points labeled as “blowdown” or “no blowdown” using the high resolution ortophotomaps. Basing on this dataset, 1) TPR is the share of points correctly detected as blowdown in the overall number of “blowdown” points, and 2) FPR is the share of points misclassified as blowdown in the overall number of “no blowdown” points. The TPR-FPR plots allowed to find the most efficient parameters of the detection method (Fig. 3 in (Godziek et al., 2025)). In the case of blowdown mapping, the true negative (TN – areas correctly classified as “no blowdown”) and false negative (FN – areas being blowdown, but incorrectly classified as “no blowdown”) classes can be defined. For landforms (i.e., root plates and pit-mound topography) detection rate, only the metrics of three classes can be attributed: 1) true positive rate (TPR, forms detection rate), i.e., the share of correctly detected forms in the overall number of forms in the validation dataset (forms existing in the field), 2) false negative rate (FNR), i.e., the share of undetected forms in the overall number of forms in the validation dataset, and 3) false positive rate (FP, false positive share, share of artefacts), i.e., the share of incorrectly detected objects (artefacts) in the number of all detected objects.

For forms detection, there is no possibility to quantify the true negative (TN) class, as it should be considered as the entire area outside the detected forms. The TPR and FNR complement each other to 100%, so knowing the TPR, we also know the FNR. Hence, for the root plate detection, the author took into consideration the root plate detection rate and false positives share (Fig. 4 in (Godziek, 2024)). The validation was based on field measurements of root plates location and dimensions using GNSS receiver with < 5cm precision (Fig. 2 in (Godziek, 2024)). For pit-mound detection, the author validated the results using the forms location dataset created by manual recognition of pit-mound pairs using topographic position index (TPI). The mapping results (Tab. 1 in (Godziek and Pawlik, 2023)) refer to TPR (“detected”) and FNR (“undetected”). The “misrecognized” column is connected with the errors in recognition of convex (mound) and concave (pit) forms. For pit-mound pairs, the “partially detected” column refers to the cases, where only pit or only mound were detected.

The dissertation was complemented by the analysis of the environmental issues of the September 2020 Colorado Front Range blowdown (Godziek et al., 2025). As the potential future applications of all proposed RS methods require the environmental-perspective on windthrow investigation, this additional component acts as a valuable example of studying of the past and recent wind-driven forest disturbance events. The author 1) investigated the windthrow origin by exploring the meteorological time series, 2) studied the relationship between windthrow areas distribution and the topography using the United States Geological Survey 1 m resolution DTM resampled to 10

m pixel size, and 3) measured the tree fall directions and root plate dimensions at the sample blowdown patch to gain an insight into in-situ effects of the disturbance event (Godziek et al., 2025).

Results

The types of identified objects and the precision of their detection vary depending on the methods used. Regarding the blowdown mapping, the most effective output was based on Sentinel-2 band pairs 11 and 12, together with $40° < drct < 47°$ and $mgt > 0.1$, having the TPR of 66.04% and FPR of only 0.89%. These results can be adjusted to higher TPR, however this is connected with the FPR increase (Tab. 1 in (Godziek et al., 2025)). In case of the root plate mapping, the detection rate was 79.1%, 71.2% and 70.3% for three investigated 100x100 m study plots, respectively (Fig. 5 in (Godziek, 2024)). The root plate volumes computed with the RS-based approaches were in a similar range to the ones estimated using the field data. The mean calculated biotransport was the highest when using ZS, lower for CNT, and the lowest for FM (Tab. 4, Fig. 8 in (Godziek, 2024)). Pit-mound pairs detection rate was at the level of 90.6% and 85.7% for two study areas, whereas the highest detection rate for pits reached 95.2 – 96.9%, and for mounds – 90.5% - 93.8% (Tab. 1 in (Godziek and Pawlik, 2023)).

The detection rate of all proposed methods was influenced by different technical and environmental factors. Generally, tuning of all methods to achieve the best possible results confirmed that the growth of the true positives rate is always combined with the increase in the false positives rate, and low values of FPR are accompanied with lowering in the values of TPR. Hence, the key problem is to find the optimal parameters for each method to maximally increase the detection rate and maximally lower the share of false detections. Regarding the CVA-based windthrow mapping, when using only the magnitude parameter the TPR could be increased up to the 88.7%, however with the accompanying growth of the FPR to 17.8% (Tab. 1 in (Godziek et al., 2025)). For the root plate detection, the maximal detection rate of 89.6 – 86.1% is associated with the share of artefacts (false positives) at the level of 59.9 – 57.2% (Tab. 2 in (Godziek, 2024)). The detection procedures were also influenced by their geomorphometric features, i.e., the size and shape. Regarding the root plate detection, this impacted the choice of the DM contour line values (0.5, 1 and 1.5 m) used to extract polygons indicating true root plates (referred to as *cnt_plg* in (Godziek, 2024)). Regarding the pit and mound topography, the best detection results were obtained for the highest tested DTM resolution of 10 cm and the smallest adopted contour line interval of 5 cm (Tab. 1 in (Godziek and Pawlik, 2023)). In addition, the pit-mound pair filtering aiming at excluding forms of no-blowdown origin was performed by using the distance criterion of < 1.5 m between adjacent pits and mounds. For pits and mounds, the terrain slope also matters,

as most of the determined potential locations of these forms were situated at gentle slopes. (Fig. 6 in (Godziek and Pawlik, 2023)). This was partly confirmed by the statistical analysis of the topography properties of the study plots (Tab. 2, Figs. 3S – 8S in (Godziek and Pawlik, 2023)).

Another issue is connected to the source data properties and preprocessing procedures. Regarding the blowdown mapping, sites with damage smaller than the pixel size of the Sentinel-2 (10 m) cannot be detected. The spectral response of such sites is not clear, and blended with different site properties, not linked to damage (for instance, standing living trees that survived the windstorm). For root plates, the analysis of the impact of the point cloud density revealed that the detection rate was the highest for point clouds with densities of 8 – 20 pts/m^2 (Fig. 7 in (Godziek, 2024)). In the case of both root plates and pit-mound topography, the LiDAR ground points classification is crucial. The exploration of different point clouds revealed, that the reflections from the root plates and fallen tree stems are classified as low or medium vegetation (Godziek, 2024). The root plate detection was also impacted by the presence of various understory objects "impermeable" for the LiDAR laser beam, i.e., dense young conifers, fallen stems, and broken tree trunks. Moreover, some root plates were eroded, pinned by tree stems, or overgrown by vegetation, which made the detection and DM analysis task more complex (Tab. 3, Fig. 6 in (Godziek, 2024)).

The comparison between CVA-based windthrow mapping and the GFC data revealed that 1) large blowdown areas (> 1 ha) were detected by both approaches, 2) CVA was better in detecting small blowdowns with nearly all trees damaged (high damage intensity), 3) GFC was able to capture the blowdown areas with lower damage intensity (with a significant number of undamaged trees), uncaptured by CVA, and 4) both approaches were partly unsuccessful with detecting forest damages of the size around 0.25 ha or smaller (Fig. 6 in (Godziek et al., 2025)). The blowdown area was estimated to be 1,379.7 ha using CVA and 1,569 ha by using GFC data (Fig. 5 in (Godziek et al., 2025)). The wind direction and speed analysis revealed that the windthrow triggering factor was the Easterly wind blowing with maximal recorded speed of 30 $m \cdot s^{-1}$ through ca. 40 hours on September 7 - 9, 2020 (Fig. 4 in (Godziek et al., 2025)). The blowdown area followed the run of ridges and valleys, frequently occupying NE slopes (Fig. 5, Fig. 7 in (Godziek et al., 2025)). The tree fall direction measured during the field survey was NW, W or SW, which confirms the blowdown was triggered by the wind from the Eastern sector. The volumes of 60 measured root plates ranged from 0.1 to 1.29 m^3 (Fig. 8 in (Godziek et al., 2025)).

Discussion

Novelty and applications

The methods proposed in this thesis are novel in several aspects, which include: 1) proposing the root plates and pit-mound topography mapping workflows based on LiDAR data, 2) developing the techniques of single root plate volume estimation, based on LiDAR data, 3) implementing the change vector analysis for the blowdown detection for the first time in North America, 4) preparing scripts in R programming language to automate all the workflows, and 5) presenting the detailed exploration and evaluation of factors affecting the quality of these methods outputs. The presented environmental insights contribute to the fields of geomorphology, soil science, and forest ecology through: 1) exploring and explaining the spatial distribution patterns of root plates and pit-mound topography, 2) quantifying the biotransport driven by tree uprooting, and 3) providing the analysis of the to-date unexplored 2020 wind event in the Colorado Front Range. The new original results, together with their potential applications are presented in Table 1.

Table 1. Summary of the novel results of this thesis and their potential applications.

Aim →	**blowdown mapping workflow using CVA**	**root plates detection**	**root plates volume estimation**	**pit-mound topography detection**
Input RS data	Sentinel-2 optical imagery	LiDAR point cloud and elevation models		LiDAR-based Digital Terrain Model
Spatial scope	Western slope of the Colorado Front Range, Rocky Mts., U.S.	Babia Góra National Park & Gorce National Park, Western Carpathians, Poland		Babia Góra National Park, Western Carpathians, Poland
Results	TPR of 66.04% and FPR of 0.89% for Sentinel-2 band pairs 11 and 12, together with $40° < drct < 47°$ and $mgt > 0.1$	root plate detection rate of 79.1%, 71.2% and 70.3% for three investigated 100x100 m study plots	the overall mean biotransport ranging from 176.1 to 268.3 [m^3/ha], depending on the applied technique (FM, CNT, ZS)	pit-mound detection rate of 90.6% and 85.7% for two study areas; pits detection rate of 96.9 – 95.2%; mounds detection rate of 93.8% - 90.5%
Potential applications	investigating the blowdown distribution, researching the impact of environmental factors on blowdowns	spatial distribution of root plates, tracking root plates erosion through time, support during forestry works on the blowdown areas	exploring the scale of the uprooting-induced biotransport and factors influencing this process, studying impact of tree uprooting on soils	spatial distribution of pit-mound topography, reconstruction of former windthrow patches, studying impact of tree uprooting on soils
Research paper	Godziek, Pawlik, Buma, 2025	Godziek, 2024		Godziek, Pawlik , 2023

Abbreviations: CNT – contour lines, CVA – change vector analysis, *drct* – direction, FM – field measurements, FPR – false positives rate, *mgt* – magnitude, LiDAR – Light Detection and Ranging, TPR – true positives rate, ZS – zonal statistics

The presented methods pose a valuable contribution to the application of remote sensing data for studying the wind-induced forest disturbances and their geomorphic effects. To date, many studies focused on windthrow mapping using optical (Einzmann et al., 2017; Dalponte et al., 2020), and radar (SAR) data (Tanase et al., 2018; Lazecky et al., 2021). Our results on forest damage detection are based on the first application of the RS and CVA approach for North American blowdowns. The presented workflow can be further expanded and examined by testing for other study sites in the Rocky Mts. and beyond. These results are of a high quality due to a very low share of false positives, which enabled them to be used for environmental analysis. Although the study

was performed for a limited area and for one blowdown event, future analyses can be expanded to a greater number of windthrows. The root plate detection method is the first attempt to quantify these landforms using RS, as previous studies in this field focused only on employing LiDAR data to map logs of fallen and broken trees (Mücke et al., 2012; Nyström et al., 2014; Joyce et al., 2019). The achieved output is promising, but will be further improved by testing the workflow for new study sites and by testing new ideas to reduce the number of artefacts.

Similarly, the study on the pit-mound topography detection is also the first attempt to map these forms using detailed DTMs. Studies to-date on similar microforms have been focused on man-made features, such as burial mounds and pitfall traps (Freeland et al., 2016; Trier et al., 2019; Niculiță, 2020). The only previous attempt to quantify pit-mound pairs was a theoretical analysis basing on topographic roughness (Doane et al., 2021). The pit-mound topography mapping method presented in this dissertation is used for individual form detection. For the first time, the author proposes also the RS-based way to accurately estimate biotransport due to uprooting. Studies to-date on this matter have been based on modeling (Constantine et al., 2012) or estimations for the entire slopes (Doane et al., 2023). As based on a single landform detection, the methods developed by the author support accurate modeling of soil biotransport and biomorphodynamics caused by high winds. The examination of these processes at the level of single landforms provides high accuracy output and may shed new light on the understanding of complex interactions between strong wind, trees, and relief.

The application of the proposed methods include the following scientific disciplines: remote sensing, forest ecology, geomorphology, soil science, and natural environment reconstruction, and in the sectors of forestry and geotechnical engineering. Generally, these methods are complementary to each other, and applying all of them for a given study area can provide complex information on the present and past windthrow dynamics. Research perspectives include primarily the application of these methods for larger areas. The analyses performed in the small mountain range scale would shed new light on the relationships between wind, trees, and relief. Different potential factors influencing these relations may be taken into account to find hidden patterns and connections. Adding the volume calculation of root plates and pit-mound pairs positions would enable creating a map of soil disturbances during a blowdown event. Such data may then be applied to investigate the factors influencing blowdown-induced soil biotransport (hillslope biomorphodynamics). Potential factors may include: topography (aspect, slope, etc.), wind direction and speed, soil and bedrock properties, forest type, etc. To date, these methods have been applied only for spruce-dominated forests. As such, they should be tested for non-spruce central European forests and for forests from different parts

of the world to check the outputs and adjust the parameters to various conditions. A comparison of potential outputs may offer new hints on the evolution of forest ecosystems under wind-driven disturbances across the world.

Finally, the presented methods may be applied to investigate single windthrow events; such research should be combined with the analysis of meteorological conditions, topography, and soil disturbance effects. For the September 2020 event in the Colorado Front Range, the wind data exploration revealed the significance of the wind direction for the blowdown formation, and led to the conclusion that wind from atypical direction may be the main driver of forest damage. A similar event, however associated with 10 times more damage area, occurred in the Rockies in 1997, and was also associated with infrequent Easterly winds (Poulos et al., 2002; Kulakowski and Veblen, 2002). A high rate of damaged stands within areas featuring the NE aspect confirmed the impact of topography on the damage distribution. The study on root plates showed their different dimensions and properties in comparison to the results from Europe. This discrepancy is due to a higher number of tree species studied to date in the European context. However, it confirms the need of testing the method for different environmental conditions all over the world. The author did not perform the LiDAR data analysis for the Rocky Mts., as 1) the main aim of the study was to test the CVA approach, and 2) in the U.S., the LiDAR data access is restricted. However, there is a perspective for future studies with employing the point clouds for the Rocky Mts. and testing various aspects of this dissertation for environmental conditions that differ from those from the Western Carpathians.

Challenges

The development of each method faced similar difficulties and challenges, which included: 1) dealing with false positives, 2) managing the data quality and preprocessing issues, 3) applying various validation strategies, and 4) handling with the impact of different environmental properties and processes.

In the case of each detection workflow, choosing the parameters lowering the false positives rate as much as possible was crucial, because the desired end-use applications of the proposed methods include drawing environmental conclusions basing on the outputs. False positives are an important problem in RS-based detection (Forbes, 1995), and therefore even a small drop in the FPR is valuable for mapping purposes. The easiest solution to deal with a too high false positive rate is to use a semi- automated approach based on 1) running the detection algorithm, and then 2) assessing the results by "on-screen" analysis of landform shapes or comparison with other RS data (e.g., ortophotomaps or DTM-derived metrics and topographical indexes). The disadvantage of such approach is the need for evaluating all detection results, which may be time-consuming

in the case of mapping large areas. The alternative could be inventing and implementing other detection algorithms, e.g., based on artificial intelligence, machine learning or pattern recognition; these methodologies have already been applied for similar tasks (Hansen et al., 2013; Trier et al., 2019). However, with the current computing technology development level the author assumes that any method could produce false positives affecting results quality. Therefore, to drive the valid environmental conclusions basing on the method output, there is a need for assessing the obtained results by an expert in a given field of study.

Regarding the data quality and preprocessing, optical satellite imagery analysis for blowdown mapping faces the issues of atmospheric corrections, shadows, and cloud masking. The author used the Sentinel images at the level 2A, which are already corrected to the bottom of the atmosphere reflectance by the data provider (ESA, 2024). For the selected study area (Rocky Mts., Colorado), the author was able to find pre- and post-event images with the cloudiness below 10%, for which clouds occupied a very small part of the mapping area and could be masked manually using GIS tools. However, for other study areas the cloud masking may be a critical issue impacting the mapping accuracy. The data resolution also matters for windthrow mapping, as the lower resolution (e.g., 10 m, 30 m) disables detecting small-size blowdown patches. Hence, the output of the mapping based on the satellite data presents some level of generalizability of a given disturbance event extent, which can be the advantage or disadvantage depending on the study aim. However, knowing the data limitations, the author acknowledges here that this cutting-edge technology has already pushed forward many aspects of environmental studies. Similarly, the input LiDAR data quality affect the detection of pit-mound topography and root plates. The results have shown that the root plates detection is not possible for point clouds with densities below 8 pts. / m^2 (Fig. 7 in (Godziek, 2024)). The laser scanning results vary also depending on the leaf-off / leaf-on season (Moudrý et al., 2019), which may affect the possibility of detection in areas with dense understory vegetation – hence, using data acquired in leaf-off season is recommended. In the case of pit-mound topography, LiDAR ground points classification is the most crucial to avoid false positives related to misclassified reflections. Such classification may be difficult for the areas covered by dense vegetation. Different algorithms may be applied, such as progressive morphological filter (Zhang et al., 2003) or cloth simulation function (Zhang et al., 2016b). The way to eliminate the potential ground reflections classification errors would be 1) a visual inspection of the classified point cloud, and 2) using the validation data acquired in the field.

The validation strategies are the key for evaluating the performance of the proposed methods and each applied strategy has its advantages and disadvantages. For windthrow detection, placing the points randomly ensures the valid representation of the ground-truth information across the entire mapping area. However, even when setting the minimum distance between points to 20 m,

the information from some parts of the terrain may be underrepresented. There is also a problem of "blowdown" / "no-blowdown" class balance. As the majority of points belong to the "no-blowdown" class, the number of points has to be sufficient to ensure the "blowdown" class is well represented and high enough to validate the results. The blowdown patch size should be also taken into account during the attribution of the class (damage / no damage) to the validation points, because using the 10 m resolution imagery disables the detection of the wind damage area smaller than 100 m^2. Hence, while attributing the class to the validation point, the assessment of the RS image should be done for point buffer representing the pixel size of this image. Considering the root plates detection method, field mapping of all desired objects within a study plot is one of the key steps. In addition, re-validation (by the field inspection) of the obtained modelling results is quite important as it provides valuable insights into potential causes of artefacts occurrence. The root plate dimension measurements must follow the adopted scheme and measurement rules in all cases to ensure data consistency and effective validation of the results. For pit-mound topography, manual labeling of landforms based on the DTM derivatives must be based on confidence that all marked landforms are pit-mound pairs of windthrow origin. Conducting the studies in protected forests undisturbed by recent human activity ensures the natural origin of the investigated forms. Due to the unique and specific shape of pit-mound pairs produced by the tree uprooting process, the field validation is frequently not necessary. Also, in many cases the field inspection is not possible due to the area inaccessibility or due to formal restrictions. The detailed guidelines with the criteria for landforms to be included in the validation dataset could be produced basing on the experiences acquired during the DTM-derived raster data exploration.

Many outcomes and spatial representations of natural phenomena and features can be difficult to label and classify, as there are many intermediate states of their superficial forms. When dividing pixels into "blowdown" or "no blowdown" classes, there are areas with different damage intensities, and in case of binary classification (0-1) the threshold for the windthrow class for magnitude and direction rasters has to be somehow defined. This threshold must be a kind of compromise between the rates of correct and wrong detections (considering false negatives and false positives). For producing maps, the binary classification is essential in many cases. However, blowdown could be also mapped by non-binary classification by attributing the pixels with the amount of change, which is related to windthrow intensity (Dalponte et al., 2020). Such an approach may be more efficient for detecting small-scale damages and for acquiring a more accurate point of view. Regarding the root plates and pit-mound topography, the erosion and denudation processes are the main drivers of the variability of landform shapes (Schaetzl et al., 1990; Pawlik, 2013). Newly uprooted trees produce sharp, steep, and clearly recognizable root plates. Their height is subsequently lowered due to erosion (deterioration) as the soil material falls of and slips off and

tree trunk decomposes. Finally, they can be overgrown and transform into a pit-and-mound pair (Šamonil et al., 2010). Hence, the shape of a pit-mound pair is a derivative of the shape of a root plate, which is controlled primarily by tree-related factors (tree species and size) and by soil and bedrock properties. In addition, slope angle and the tree fall direction are important; for the downslope uprooting, the pit is clearly visible, and for the upslope uprooting, the root plate frequently rotates and slides into the pit (Šamonil et al., 2020). Also, root plates may be overgrown by vegetation (small trees, bushes) and hit by a neighboring tree stem that fell on it. Due to all these factors, shapes of root plates and pit-mound pairs may differ significantly, and it can pose difficulties in the detection process.

The way to handle this problem is to adjust the methods for detecting the "standard-shape" forms. Landforms with "non-standard" shapes could require further development of the presented methods; it may include extending the methods to 1) root plates (root balls) of deeply-rooted species (e.g., pines and beeches), and 2) pit-mound pairs related to upslope uprooting. Quantifying the volume of soil displaced during the windthrow event would be important to assess the geomorphic impact of wind-driven disturbances on slopes (Pawlik, 2013). The results of volume estimation for root plates using LiDAR-derived differential model are valid, as their values fit within the range of published root plate volume estimations (Dąbrowska, 2009; Richards et al., 2011; Rojan, 2012; Strzyżowski et al., 2018).

The meaningful volume differences between the three approaches (ZS > CNT > FM) suggest the methodological factors influencing the final results. There are also issues related to the root plate shape, e.g., the formation of overhang with an empty space underneath at the site opposite the fallen tree trunk. For such cases it increases the computed root plate volume. The equation applied in the FM approach is considered a close approximation of the root plate volume. However, to find which approach is the most accurate, root plate volumes should be investigated with more accurate tools, such as terrestrial laser scanning (TLS) or structure from motion (SfM). Then, such results could be compared with the estimations based on ZS, CNT and FM. This would allow to discover which approach is the most accurate and reliable in approximating the root plate volume.

The accuracy of all the workflows is the derivative of all above-described issues and applied method's parameters, such as satellite image bands, filtering thresholds, indices used for filtering, contour line intervals, data spatial resolution, etc. In addition, the main aims of these workflows automation was primarily 1) their practical applications in a wider spatial and temporal scale (e.g., the scale of the mountain ranges) to improve understanding of windthrows and related geomorphic processes, and 2) the possibility of fostering the research replicability by sharing the source code. All scripts were written using R programming language, however with present AI tools they can be translated to any other programming language providing the necessary functionalities.

Conclusions

The author invented, developed, and tested workflows for automatic detection of root plates of fallen trees and pit-mound topography. A detailed study was also carried out on employing the change vector analysis approach for blowdown mapping. The environmental aspect of the thesis included an investigation on spatial distribution patterns of root plates and pit-mound topography, detailed estimation of the amount of soil-rock material transported by tree uprooting (i.e., biotransport), and an examination of the 2020 blowdown in the Colorado Front Range. All the results are complementary, and their conclusions could be used in the future to foster the understanding of complex interplays between wind, trees, and relief. Automation proposed in R programming language is an additional value of the thesis, facilitating performing the analysis for larger areas. The dissertation presents new contribution to the fields of remote sensing, geomorphology, and forest ecology.

Literature

Barker Plotkin, A., Schoonmaker, P., Leon, B., Foster, D., 2017. Microtopography and ecology of pit-mound structures in second-growth versus old-growth forests. For. Ecol. Manag. 404, 14–23. https://doi.org/10.1016/j.foreco.2017.08.012

Bonannella, C., Hengl, T., Heisig, J., Parente, L., Wright, M.N., Herold, M., de Bruin, S., 2022. Forest tree species distribution for Europe 2000–2020: mapping potential and realized distributions using spatiotemporal Machine Learning (preprint). In Review. https://doi.org/10.21203/rs.3.rs-1252972/v3

Constantine, J.A., Schelhaas, M.-J., Gabet, E., Mudd, S.M., 2012. Limits of windthrow-driven hillslope sediment flux due to varying storm frequency and intensity. Geomorphology 175–176, 66–73. https://doi.org/10.1016/j.geomorph.2012.06.022

Dąbrowska, K., 2009. The morphogenetic impact of the bora type wind (19thNovember 2004) on the relief of Danielov dom area (The High Tatras). Landf. Anal. Vol. 11, 5–10.

Dalponte, M., Marzini, S., Solano-Correa, Y.T., Tonon, G., Vescovo, L., Gianelle, D., 2020. Mapping forest windthrows using high spatial resolution multispectral satellite images. Int. J. Appl. Earth Obs. Geoinformation 93, 102206. https://doi.org/10.1016/j.jag.2020.102206

European Space Agency (ESA). 2024. "Sentinel-2A MSI Level-2A. Distributed by Copernicus Data Space Ecosystem." https://dataspace. copernicus.eu/

Faliński, J.B., 1976. Trwałość reliktów lasu w krajobrazie rolniczym w świetle obserwacji na stałych powierzchniach. Phytocoenosis 5.4, 190–213.

Fall, A.F., Nakabonge, G., Ssekandi, J., Founoune-Mboup, H., Apori, S.O., Ndiaye, A., Badji, A., Ngom, K., 2022. Roles of Arbuscular Mycorrhizal Fungi on Soil Fertility: Contribution in the Improvement of Physical, Chemical, and Biological Properties of the Soil. Front. Fungal Biol. 3. https://doi.org/10.3389/ffunb.2022.723892

Forbes, A.D., 1995. Classification-algorithm evaluation: Five performance measures based onconfusion matrices. J. Clin. Monit. 11, 189–206. https://doi.org/10.1007/BF01617722

Forzieri, G., Pecchi, M., Girardello, M., Mauri, A., Klaus, M., Nikolov, C., Rüetschi, M., Gardiner, B., Tomaštík, J., Small, D., Nistor, C., Jonikavicius, D., Spinoni, J., Feyen, L., Giannetti, F., Comino, R., Wolynski, A., Pirotti, F., Maistrelli, F., Savulescu, I., Wurpillot-Lucas, S., Karlsson, S., Zieba-Kulawik, K., Strejczek-Jazwinska, P., Mokroš, M., Franz, S., Krejci, L., Haidu, I., Nilsson, M., Wezyk, P., Catani, F., Chen, Y.-Y., Luyssaert, S., Chirici, G., Cescatti,

A., Beck, P.S.A., 2020. A spatially explicit database of wind disturbances in European forests over the period 2000–2018. Earth Syst. Sci. Data 12, 257–276. https://doi.org/10.5194/essd-12-257-2020

Gabet, E.J., Reichman, O.J., Seabloom, E.W., 2003. The Effects of Bioturbation on Soil Processes and Sediment Transport. Annu. Rev. Earth Planet. Sci. 31, 249–273. https://doi.org/10.1146/annurev.earth.31.100901.141314

Gardiner, B., 2021. Wind damage to forests and trees: a review with an emphasis on planted and managed forests. J. For. Res. 26, 248–266. https://doi.org/10.1080/13416979.2021.1940665

Gerlach, T., 1960. Report on the origin of small earth hillocks on the Hala Długa in the Gorce range. Przegląd Geol. 32, 86–93.

Godziek, J., 2024. Root plates of uprooted trees − Automatic detection and biotransport estimation using LiDAR data and field mapping. Int. J. Appl. Earth Obs. Geoinformation 131, 103992. https://doi.org/10.1016/j.jag.2024.103992

Godziek, J., Pawlik, Ł., 2023. Indicators of wind-driven forest disturbances – pit–mound topography, its automatic detection and significance. CATENA 221, 106757. https://doi.org/10.1016/j.catena.2022.106757

Godziek, J., Pawlik, Ł., Buma, B., 2025. The Mapping and Analysis of the Infrequent, Large-Scale Blowdown Event in the Colorado Front Range. Land Degrad. Dev. 0, 1–17. https://doi.org/10.1002/ldr.5623

Hansen, M.C., Potapov, P.V., Moore, R., Hancher, M., Turubanova, S.A., Tyukavina, A., Thau, D., Stehman, S.V., Goetz, S.J., Loveland, T.R., Kommareddy, A., Egorov, A., Chini, L., Justice, C.O., Townshend, J.R.G., 2013. High-Resolution Global Maps of 21st-Century Forest Cover Change. Science 342, 850–853. https://doi.org/10.1126/science.1244693

Havašová, M., Ferenčík, J., Jakuš, R., 2017. Interactions between windthrow, bark beetles and forest management in the Tatra national parks. For. Ecol. Manag. 391, 349–361. https://doi.org/10.1016/j.foreco.2017.01.009

Holeksa, J., Jaloviar, P., Kucbel, S., Saniga, M., Svoboda, M., Szewczyk, J., Szwagrzyk, J., Zielonka, T., Żywiec, M., 2017. Models of disturbance driven dynamics in the West Carpathian spruce forests. For. Ecol. Manag., Ecology of Mountain Forest Ecosystems in Europe 388, 79–89. https://doi.org/10.1016/j.foreco.2016.08.026

Joyce, M.J., Erb, J.D., Sampson, B.A., Moen, R.A., 2019. Detection of coarse woody debris using airborne light detection and ranging (LiDAR). For. Ecol. Manag. 433, 678–689. https://doi.org/10.1016/j.foreco.2018.11.049

Kooch, Y., Hosseini, S.M., Mohammadi, J., Hojjati, S., 2012. Effects of uprooting tree on herbaceous

species diversity, woody species regeneration status and soil physical characteristics in a temperate mixed forest of Iran. J. For. Res. 23. https://doi.org/10.1007/s11676-012-0236-6

Kotarba, A., 1970. The morphogenetic role of foehn wind in the Tatra Mts. Stud. Geomorphol. Carpatho-Balc. 4, 171–188.

Kozak, J., 2022. Geography: a digital approach. Institute of Geography and Spatial Management, the Jagiellonian University, Kraków.

Kulakowski, D., Veblen, T.T., 2002. Influences of fire history and topography on the pattern of a severe wind blowdown in a Colorado subalpine forest. J. Ecol. 90, 806–819. https://doi.org/10.1046/j.1365-2745.2002.00722.x

Lazecky, M., Wadhwa, S., Mlcousek, M., Sousa, J.J., 2021. Simple method for identification of forest windthrows from Sentinel-1 SAR data incorporating PCA. Procedia Comput. Sci., CENTERIS 2020 - International Conference on ENTERprise Information Systems / ProjMAN 2020 - International Conference on Project MANagement / HCist 2020 - International Conference on Health and Social Care Information Systems and Technologies 2020, CENTERIS/ProjMAN/HCist 2020 181, 1154–1161. https://doi.org/10.1016/j.procs.2021.01.312

Mitchell, S.J., 2013. Wind as a natural disturbance agent in forests: a synthesis. Forestry 86, 147–157. https://doi.org/10.1093/forestry/cps058

Moudrý, V., Gdulová, K., Fogl, M., Klápště, P., Urban, R., Komárek, J., Moudrá, L., Štroner, M., Barták, V., Solský, M., 2019. Comparison of leaf-off and leaf-on combined UAV imagery and airborne LiDAR for assessment of a post-mining site terrain and vegetation structure: Prospects for monitoring hazards and restoration success. Appl. Geogr. 104, 32–41. https://doi.org/10.1016/j.apgeog.2019.02.002

Mücke, W., Hollaus, M., Pfeifer, N., 2012. Identification of dead trees using small footprint full- waveform airborne laser scanning data 9.

Niculiță, M., 2020. Geomorphometric Methods for Burial Mound Recognition and Extraction from High-Resolution LiDAR DEMs. Sensors 20, 1192. https://doi.org/10.3390/s20041192

Pawlik, Ł., 2013. The role of trees in the geomorphic system of forested hillslopes — A review. Earth-Sci. Rev. 126, 250–265. https://doi.org/10.1016/j.earscirev.2013.08.007

Phillips, J.D., 2009. Biological energy in landscape evolution. Am. J. Sci. 309, 271–289. https://doi.org/10.2475/04.2009.01

Phillips, J.D., Marion, D.A., Turkington, A.V., 2008. Pedologic and geomorphic impacts of a tornado blowdown event in a mixed pine-hardwood forest. CATENA 75, 278–287. https://doi.org/10.1016/j.catena.2008.07.004

R Core Team. 2024. R: A Language and Environment for Statistical Computing. R Foundation for Statistical Computing. https://www.r-project.org/.

Richards, P.J., Hohenthal, J.M., Humphreys, G.S., 2011. Bioturbation on a south-east Australian hillslope: estimating contributions to soil flux: BIOTURBATION: ESTIMATING CONTRIBUTIONS TO SOIL FLUX. Earth Surf. Process. Landf. 36, 1240–1253. https://doi.org/10.1002/esp.2149

Rojan, E., 2012. Mikrorzeźba jamowo-kopczykowa w granicach wiatrowału w słowackich Tatrach Wysokich. Pit-and-mound microrelief in the windthrow area in the Slovak High Tatras. Pr. Stud. Geogr. 49, 173–183.

Rojan, E., 2010. Rola silnych wiatrów w przekształcaniu rzeźby terenu w piętrze leśnym gór, na przykładzie wiatrowału w słowackich Tatrach Wysokich. Czas. Geogr.

Šamonil, P., Daněk, P., Schaetzl, R.J., Vašíčková, I., Valtera, M., 2015. Soil mixing and genesis as affected by tree uprooting in three temperate forests. Eur. J. Soil Sci. 66, 589–603. https://doi.org/10.1111/ejss.12245

Šamonil, P., Egli, M., Steinert, T., Norton, K., Abiven, S., Daněk, P., Hort, L., Brandová, D., Christl, M., Tikhomirov, D., 2020. Soil denudation rates in an old-growth mountain temperate forest driven by tree uprooting dynamics, Central Europe. Land Degrad. Dev. 31, 222–239. https://doi.org/10.1002/ldr.3443

Šamonil, P., Král, K., Hort, L., 2010. The role of tree uprooting in soil formation: A critical literature review. Geoderma 157, 65–79. https://doi.org/10.1016/j.geoderma.2010.03.018

Šamonil, P., Valtera, M., Schaetzl, R.J., Adam, D., Vašíčková, I., Daněk, P., Janík, D., Tejnecký, V., 2016. Impacts of old, comparatively stable, treethrow microtopography on soils and forest dynamics in the northern hardwoods of Michigan, USA. CATENA 140, 55–65. https://doi.org/10.1016/j.catena.2016.01.006

Schaetzl, R.J., Burns, S.F., Small, T.W., Johnson, D.L., 1990. Tree Uprooting: Review of Types and Patterns of Soil Disturbance. Phys. Geogr. 11, 277–291. https://doi.org/10.1080/02723646.1990.10642407

Schaetzl, R.J., Johnson, D.L., Burns, S.F., Small, T.W., 1989. Tree uprooting: review of terminology, process, and environmental implications. Can. J. For. Res. https://doi.org/10.1139/x89-001

Seidl, R., Schelhaas, M.-J., Lexer, M.J., 2011. Unraveling the drivers of intensifying forest disturbance regimes in Europe: DRIVERS OF FOREST DISTURBANCE INTENSIFICATION. Glob. Change Biol. 17, 2842–2852. https://doi.org/10.1111/j.1365-2486.2011.02452.x

Senf, C., Seidl, R., 2021. Mapping the forest disturbance regimes of Europe. Nat. Sustain. 4, 63–70. https://doi.org/10.1038/s41893-020-00609-y

Solano-Correa, Y.T., Bovolo, F., Bruzzone, L., 2019. An Approach to Multiple Change Detection in VHR Optical Images Based on Iterative Clustering and Adaptive Thresholding. IEEE Geosci. Remote Sens. Lett. 16, 1334–1338. https://doi.org/10.1109/LGRS.2019.2896385

Strzyżowski, D., Fidelus-Orzechowska, J., Żelazny, M., 2018. Sediment transport by uprooting in the forested part of the Tatra Mountains, southern Poland. CATENA 160, 329–338. https://doi.org/10.1016/j.catena.2017.09.019

Trier, Ø.D., Cowley, D.C., Waldeland, A.U., 2019. Using deep neural networks on airborne laser scanning data: Results from a case study of semi-automatic mapping of archaeological topography on Arran, Scotland. Archaeol. Prospect. 26, 165–175. https://doi.org/10.1002/arp.1731

Ulanova, N.G., 2000. The effects of windthrow on forests at different spatial scales: a review.- Forest Ecology and Management 135.

Valtera, M., Schaetzl, R.J., 2017. Pit-mound microrelief in forest soils: Review of implications for water retention and hydrologic modelling. For. Ecol. Manag. 393, 40–51. https://doi.org/10.1016/j.foreco.2017.02.048

Wężyk, P., Hawryło, P., Szostak, M., Zięba-Kulawik, K., Winczek, M., Siedlarczyk, E., Kurzawiński, A., Rydzyk, J., Kmiecik, J., Gilewski, W., Szparadowska, M., Warchoł, A., Turowska, A., 2019. Using LiDAR Point Clouds in Determination of the Scots Pine Stands Spatial Structure Meaning in the Conservation of Lichen Communities in "Bory Tucholskie" National Park. Arch. Photogramm. Cartogr. Remote Sens. 31, 85–103. https://doi.org/10.2478/apcrs-2019-0007

Zadrożny, P., Krużel, J., Lamorski, T., Nicia, P., Kozina, P., 2017. Changes of the monitoring windfallen area on the Babia Góra Mountain. J. Ecol. Eng. 18, 193–199. https://doi.org/10.12911/22998993/67097

Zhang, K., Chen, S.-C., Whitman, D., Shyu, M.-L., Yan, J., Zhang, C., 2003. A progressive morphological filter for removing nonground measurements from airborne LIDAR data. IEEE Trans. Geosci. Remote Sens. 41, 872–882. https://doi.org/10.1109/TGRS.2003.810682

Zhang, W., Qi, J., Wan, P., Wang, H., Xie, D., Wang, X., Yan, G., 2016a. An Easy-to-Use Airborne LiDAR Data Filtering Method Based on Cloth Simulation. Remote Sens. 8, 501. https://doi.org/10.3390/rs8060501

Zhang, W., Qi, J., Wan, P., Wang, H., Xie, D., Wang, X., Yan, G., 2016b. An Easy-to-Use Airborne LiDAR Data Filtering Method Based on Cloth Simulation. Remote Sens. 8, 501. https://doi.org/10.3390/rs8060501

Land Degradation & Development

WILEY

RESEARCH ARTICLE

The Mapping and Analysis of the Infrequent, Large-Scale Blowdown Event in the Colorado Front Range

Janusz Godziek[1,2] | Łukasz Pawlik[1,3] | Brian Buma[4,5]

[1]Faculty of Natural Sciences, Institute of Earth Sciences, University of Silesia, Sosnowiec, Poland | [2]International Environmental Doctoral School, University of Silesia, Sosnowiec, Poland | [3]Department of Forest Ecology, The Silva Tarouca Research Institute, Brno, Czech Republic | [4]Department of Integrative and Systems Biology, University of Colorado Denver, Denver, Colorado, USA | [5]Environmental Defense Fund, Boulder, Colorado, USA

Correspondence: Janusz Godziek (janusz.godziek@us.edu.pl)

Received: 21 December 2024 | **Revised:** 17 March 2025 | **Accepted:** 13 April 2025

Funding: This study was supported by the Polish National Science Centre—Narodowe Centrum Nauki (grant no. 2019/35/O/ST10/00032) and by the Polish National Agency for Academic Exchange—Narodowa Agencja Wymiany Akademickiej (internship agreement no. PPN/STA/2021/1/00081/U/00001).

Keywords: change vector analysis | Colorado Rocky Mountains | Global Forest Change | Sentinel 2 | soil disturbance | windthrow

ABSTRACT

Wind disturbance (blowdown, windthrow) results from particular meteorological conditions, where wind gust speed is a key factor. We map and analyze the 2020 blowdown in the Colorado Front Range (CFR), US. We (1) develop and test a tunable blowdown mapping workflow based on Sentinel 2 data and change vector analysis (CVA) and compare its output with the Global Forest Change (GFC) data, (2) explore soil disturbance patterns, and (3) analyze the impact of topography on blowdown occurrence. The CVA mapping is based on (1) the difference image computed using post- and pre-event images and (2) the parameters calculated using two bands of the difference image: magnitude representing the amount of change and direction referring to the type of change. The methodology is tunable for desired error characteristics, for example, true positive vs. false positive rates. For our test analysis, we balanced the CVA output and GFC data at a true positive rate (TPR) of 66%–67%, with a false positive rate (FPR) of 0.9% and 3%, respectively. The CVA can be adjusted to achieve a TPR up to 88.7%, which increases the FPR to 17.8%. In our test landscape, the blowdown led to soil disturbances, with root plate volumes of 0.1–0.8 m^3.

1 | Introduction

Wind is one of the most frequent drivers of forest disturbance (Mitchell 2013; Gardiner 2021). Fire, snow, drought, tree diseases, and insect outbreaks can act synergistically with wind (Seidl et al. 2011; Sommerfeld et al. 2018) in various forest regions leading to landscape changes and, in some cases, land degradation (Sturtevant and Fortin 2021; Urquiza-Haas et al. 2007; Thom et al. 2013). The overall disturbance regime is the cumulative effect of many interacting and independent disturbance processes (Buma 2015; Denman et al. 2022). Wind, drought, fire, and insect outbreaks are the main disturbance processes in most temperate forests (Senf and Seidl 2021; Tran et al. 2020; Velasco Hererra et al. 2022). Wind damage influences future disturbances as, for instance, insect outbreaks are more likely to occur in areas affected by strong wind (Baker and Veblen 1990). Blown-down trees can increase subsequent fire severity (Kulakowski and Veblen 2007). Therefore, understanding wind disturbance occurrence, location, and severity is crucial to grasp the processes of forest ecosystem recovery and transformation (Everham and Brokaw 1996).

Wind disturbance (hereafter blowdowns or windthrows) distribution is controlled by multiple biotic and abiotic factors. Blowdown originates during particular meteorological conditions, where wind gust speed is a key factor (Mitchell 2013). This overall weather pattern then interacts with topography to control localized wind speed. Tree susceptibility to blowdown for

a given wind speed is then controlled by abiotic factors like soil moisture, soil depth, and bedrock condition, which influence root strength (Mayer et al. 2005; Kenderes et al. 2007). Biotic factors influencing windthrows include stand density, tree species and height, the proportion of stem with/without branches, and stand health (Bzowski and Dziewolski 1973; Dobbertin 2002). Diseased trees might be more prone to damage by wind than healthy trees (Havašová et al. 2017).

Windthrows, common in mountainous subalpine forests around the world (Jenkins 1995; Martin and Ogden 2006; Zielonka et al. 2010; Meng et al. 2015; Iwamoto et al. 2018; Ilies et al. 2022; Dalponte et al. 2023), have been rarely studied in the Rocky Mountains (Meyers et al. 2003; Momodu 2019; Wohl 2013). In the Rockies, forest disturbance research mostly focuses on wildfires and wildfire history (e.g., (Henderson et al. 2005; Rother and Veblen 2016; Calder and Shuman 2017)), insect outbreaks (e.g., (Vorster et al. 2017; Ye et al. 2021)) and drought (e.g., (Bigler et al. 2007)). However, in these mountains, small windthrows (with area of 0.2 to several hectares) occur relatively frequently (Veblen et al. 1991). Storms do sporadically cause broad-scale, stand-replacement blowdowns, especially in the high-elevation subalpine forests (Alexander 1964; Meyers et al. 2003; Veblen et al. 1989). These events are infrequent, but due to the significant scale of damages, they can have a meaningful influence on forest structure and functioning (Veblen 2000).

There are a few examples of well-studied blowdowns in the Rocky Mountains. For example, a 1987 tornado damaged 6000 ha of forest in the Teton and Yellowstone, northwestern Wyoming (Fujita 1989; Knight 1994). Several studies investigated the October 24–26th 1997 blowdown in the Park Range, northwestern Colorado, when unexpectedly strong easterly winds (speed above 200 $km \cdot h^{-1}$) damaged over 10,000 ha of forest on the western slopes (Lindemann and Baker 2001; Kulakowski and Veblen 2002; Poulos et al. 2002; Meyers et al. 2003). The relationship between wind speed, topography, and windthrow has been studied in the Canadian Rocky Mountains (Momodu 2019). Landsat imagery was used to map small-scale forest disturbances caused by insects for two areas in Colorado (Ye et al. 2021). Small windthrow patches were studied for their impact on forest carbon distribution (Wohl 2013), and subsequently, post-blowdown channel logjams were studied in the context of hydrological impacts of blowdown (Wohl 2022). However, compared to fire or insects, relatively little is known about the context and direct impacts of blowdown in the Rocky Mountains.

One documented consequence of forest blowdowns in other regions is soil disturbance by tree uprooting (Šamonil et al. 2017) conditioned by the architecture of the root system, soil type, and the level of soil and bedrock saturation (Byrne and Mitchell 2007). In dry soils, for example, trees are more likely to snap, which causes mortality but does not disturb the soil to the same extent. Uprooting influences soil processes, soil erosion, and the slope microtopography (Šamonil et al. 2010; Pawlik 2013). Uprooting results in intact (or semi-intact) root systems exposed above the soil, along with soil and rock pieces entangled in the roots (Schaetzl et al. 1990). These mounds, along with the hole where the roots were once located, erode over time and eventually form what is known as "pit–mound topography" (Ulanova 2000; Doane et al. 2021) which may be used as an indicator of past windthrows (Schaetzl et al. 1989; Godziek and Pawlik 2023). In some regions, the mounds can take up to 6000 years before their complete disappearance (treethrow mound flattening, and treethrow pit infilling), for example, in Michigan, USA (Šamonil et al. 2013). This is important ecologically and biophysically—the pits and mounds form distinct micro-landscapes. The pits are typically wetter, the mounds drier, and they can support unique ecological communities. Pit–mound topography is also relevant to disturbance detection and mapping, as the upturned soil also impacts reflectance values and thus the appearance of the landscape on remote sensing imagery.

The location and severity of disturbances are key to understanding their prevalence and impact. Remote sensing (RS) data are invaluable for forest disturbance research. Validation and evaluation are crucial for the output reliability. RS data are frequently used to map forest disturbances (Hansen et al. 2013; Potapov et al. 2015), including blowdowns (Forzieri et al. 2020; Dalponte et al. 2020, 2023; Lazecky et al. 2021). Errors are quantified during that process and reported to help interpret the results. For example, the Global Forest Change (GFC) data (30-m horizontal resolution, Hansen et al. 2013) based on Landsat imagery identify the location and year of occurrence of forest damage globally. However, because it is a global algorithm designed and validated at global scales, it cannot be tailored for specific locations or events or for specific error characteristics (e.g., commission vs. omission errors). Evaluating new disturbance mapping workflows based on different RS data and alternative methodologies is important for improving detection accuracy, building products more useful at local scales, and assessing the reliability of the already published data.

Newly occurring disturbances need to be investigated in terms of their origin, extent, and consequences to enhance their full understanding. For this study, the GFC data indicated the presence of a 2020 damage event in the Colorado Front Range (CFR), on the western side of the Continental Divide. Using high resolution RS data (U.S. Department of Agriculture 2024), we identified the damage as a blowdown. To both better understand the soil impacts of blowdowns and test a new flexibility methodology for RS mapping of disturbances, we mapped the blowdown and conducted a targeted field survey of soil impacts. The CVA-based mapping has not yet been applied for windthrows in North America nor compared to global products, such as GFC data. Such an approach can be valuable for both accurate mapping and further development of existing RS data classification algorithms. Investigating for the first time the 2020 CFR blowdown may also shed new light on the present wind-driven forest damages, especially in terms of damage-initiating wind event characteristics, relief impact, and blowdown-induced soil disturbance. Therefore, in this study we (1) identify the meteorological conditions which caused a large blowdown in the CFR, (2) develop a blowdown mapping workflow based on Sentinel 2 data and compare this workflow with the GFC product, (3) improve the understanding of the influence of topography on blowdowns, and (4) explore the relationship between soil disturbance and tree size for this blowdown.

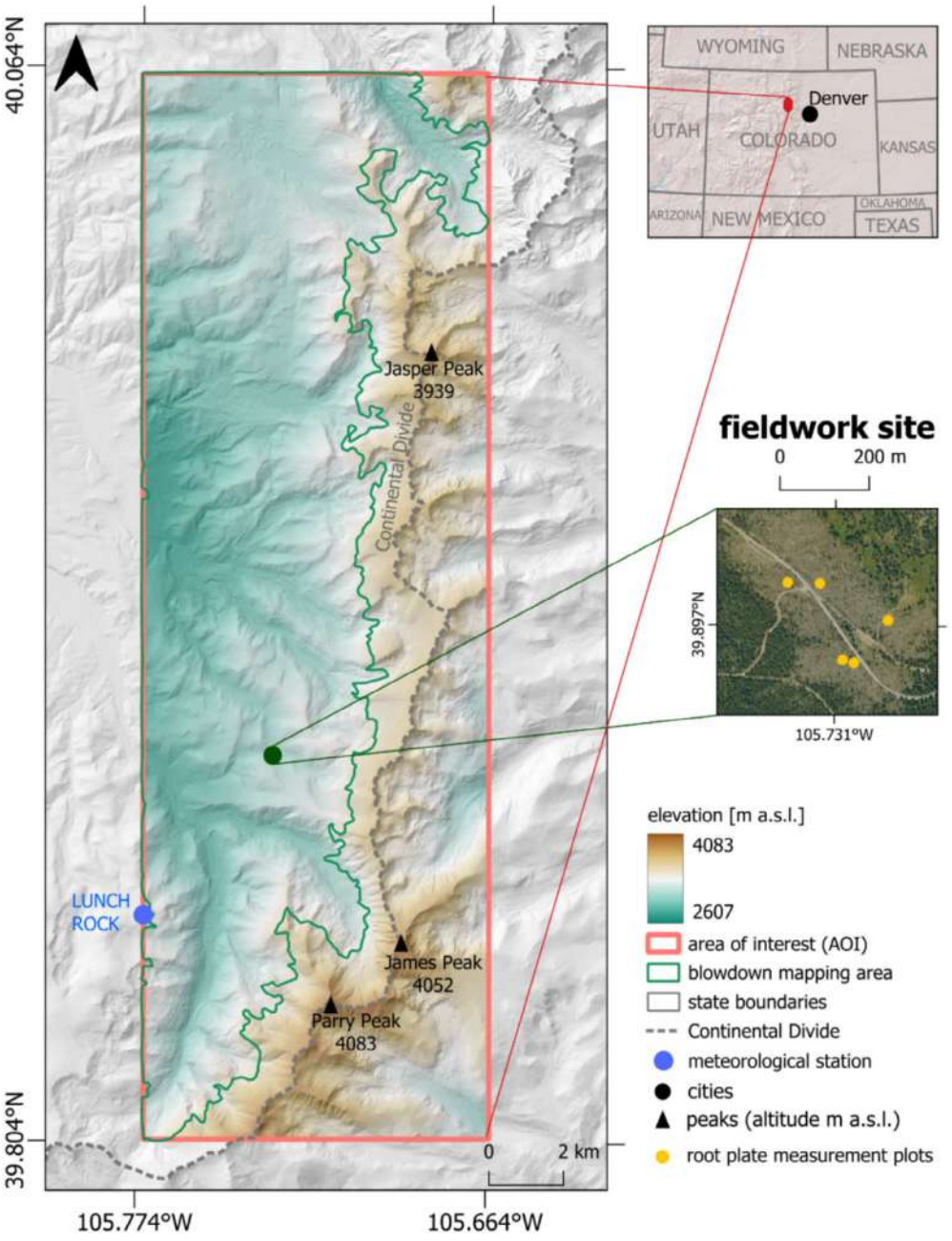

FIGURE 1 | Study area—location and topography. [Colour figure can be viewed at wileyonlinelibrary.com]

2 | Materials and Methods

2.1 | Study Area

The area of interest (AOI) is a 9 × 29 km region (39.80° N, 105.77° W and 40.06° N, 105.67° W) located in the Colorado Front Range, south of Rocky Mountain National Park and north of Berthoud Pass (max elevation: 4083 m; Figure 1). The AOI location was determined to fully encompass the blowdown region. The blowdown mapping was performed for subalpine forest growing on the western side of the Continental Divide, bounded by the AOI extent and the upper treeline (Figure 1). Forested areas cover 160.6 km^2 of the region, at an altitude of 2600–3600 m a.s.l. Using the Köppen climate classification, the climate is Subarctic (Dfc) in the higher elevation, and warm-summer humid continental (Dfb) in the lower elevation (PRISM 2024). Prevailing winds are westerly. Forest stands are mixed, dominated by Engelmann spruce (*Picea engelmannii* Parry ex. Engelm.) and lodgepole pine (*Pinus contorta var. latifolia* Douglas C. Lawson). A mountain pine beetle (*Dendroctonous ponderosae*) outbreak occurred in the nearby forests in the years 2002–2012 (Tishmack et al. 2005; Lester 2020). The AOI is also affected by wildfires, for example, the 2023 Devil's Thumb wildfire (NIFC 2024).

2.2 | Methods

2.2.1 | Windthrow Event Analysis

For the initial disturbance event analysis, we used the Global Forest Change data (version 1.10; Hansen et al. 2013). This dataset (2000 to present) is based on 30-m Landsat imagery and is updated

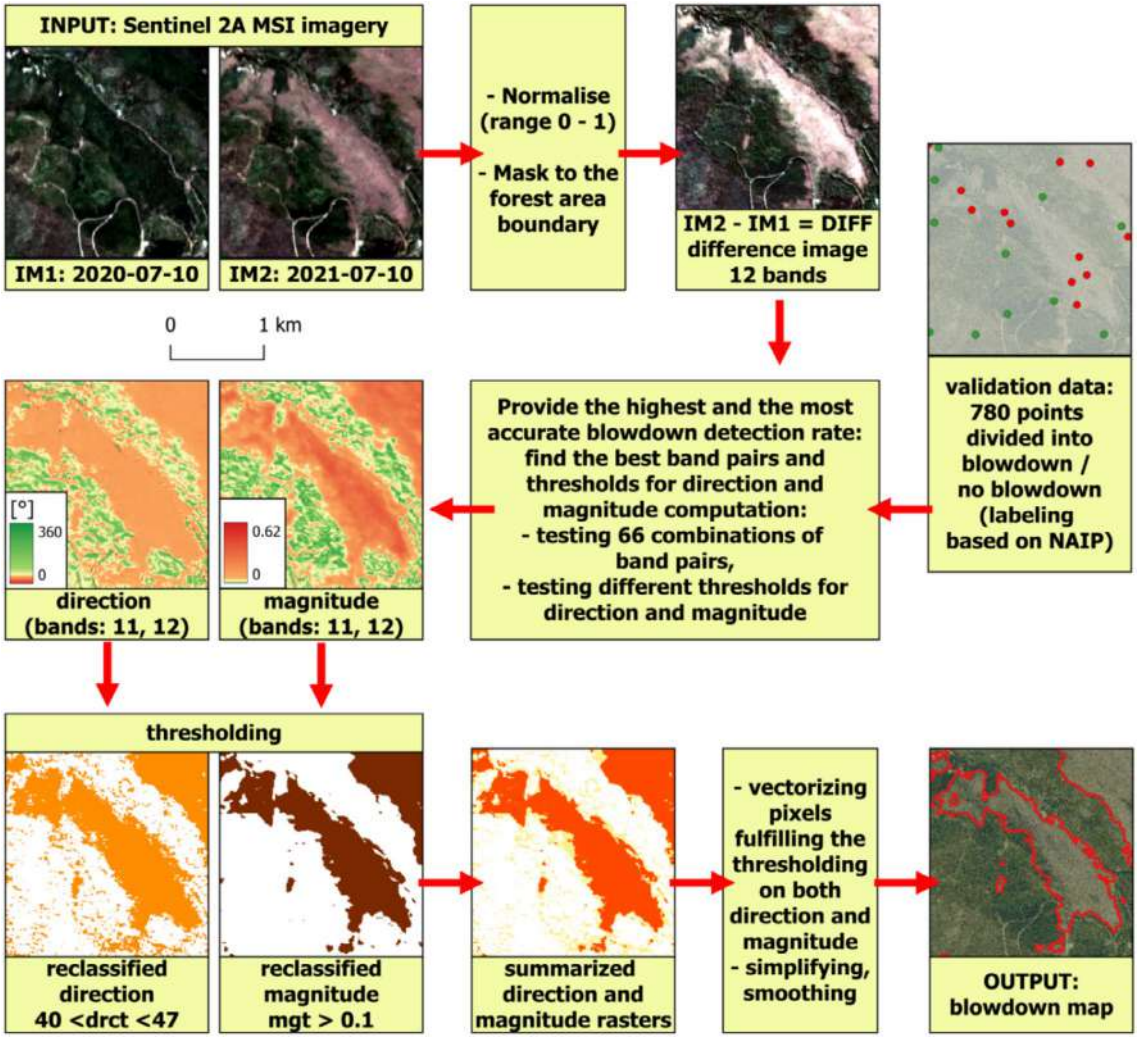

FIGURE 2 | The workflow of the change vector analysis (CVA) approach. [Colour figure can be viewed at wileyonlinelibrary.com]

yearly. This indicated a disturbance formation in 2020, but not the specific time, date, or cause. The cause (wind—blowdown) and the year of disturbance were confirmed using detailed orthophotomaps for the years 2019, 2021, and 2023 with a spatial resolution of 0.3 m or 0.6 m obtained from the National Agriculture Imagery Program (NAIP) (U.S. Department of Agriculture 2024). In the second step, the time of possible blowdown occurrence was narrowed to several days by exploring the Sentinel 2 Multispectral Instrument (MSI) satellite imagery provided by the European Space Agency (ESA) (European Space Agency (ESA) 2024). To find the particular date and time and explore wind conditions of the disturbance event, in the third step, we analyzed the meteorological data provided by the ski station Winter Park (Winter Park 2024). The data were acquired at Lunch Rock automatic meteorological station (39.858667° N, 105.7725° W) situated at an altitude of 3420 m a.s.l., slightly below the tree line. We focused especially on wind parameters (mean speed, gust speed, direction), measured at a 20-min time interval.

2.2.2 | Windthrow Mapping

We mapped the Colorado Front Range 2020 blowdown using the change detection between pre- and post-event images (Dalponte et al. 2020). We used two Sentinel 2 MSI images (European Space Agency (ESA) 2024), acquired during the same vegetation season on July 10th (pre-event image in 2020 and post-event image in 2021), to avoid the influence of the seasonality-related vegetation spectral response changes (Figure 2). We checked for additional blowdown between the dates of the pre- and post-event images and confirmed there were no further blowdowns nor other major changes to confound the analysis. We downloaded the images using R (*rsi* library) (Mahoney 2024). Each image consisted of 12 spectral bands. The analysis was performed at a 10-m spatial resolution. Bands 2, 3, 4, and 5 were available at this resolution, while all other bands were resampled from the 20- and 60-m resolution.

To map the blowdown, we built on the change vector analysis (CVA) method (Solano Correa et al. 2014; Zanetti et al. 2015). Rather than simply noting change, this method quantifies change using a vector composed of two components: direction/angle (*dir*) and magnitude (*mgt*). The direction (angle) component is derived from relative change between the brightness of the multiple, individual bands (e.g., a scene may shift more green with a reduction in some bands and brightening in others). This is interpreted as information on the type of change that occurred as a result of the disturbance (e.g.,

a wildfire, windthrow, insect outbreak, etc.). The magnitude component explains the amount of change on the continuous scale (Bovolo and Bruzzone 2007; Solano-Correa et al. 2019), and refers to the amount of change seen along the vector (e.g, the amount of greening, or the amount of browning, etc.). This is interpreted as the magnitude of change as a result of the disturbance.

The CVA method has been used for different kinds of RS data analysis (Roemer et al. 2010; Singh and Talwar 2014), including windthrows (Wang and Xu 2010; Dalponte et al. 2023). This method is well-suited for exploring single disturbance events, as it is based on the analysis of pre- and post-event images. CVA can achieve high accuracy when analyzing the images from the same vegetation period (e.g., acquired with an 1-year interval) to ensure the greatest possible similarity of pixel values for areas where land cover changes have not occurred (Dalponte et al. 2020). One advantage of the CVA technique over global methods like the GFC data is the ability to specify which two dates are used for the change analysis. We selected the CVA method and Sentinel 2 optical data to study the 2020 CFR blowdown, as the change detection approach is well-suited for exploring the single, large-scale disturbance events, and optical data are widely available for Colorado due to the low cloudiness. We aimed at testing and improving the CVA-based approach for blowdowns (Dalponte et al. 2020).

For validation, we used the NAIP orthophotomaps. Within the blowdown mapping area, we randomly located 780 validation points using the random points inside polygons tool in QGIS3 (QGIS Development Team 2024). This tool places each random point independently, and there is the same likelihood of choosing any location in the polygon. To reduce clustering and provide a more even distribution of points across the mapping area, we set the minimum distance between points to 20 m. We manually labeled each point as "blowdown" or "no blowdown" using the high-resolution NAIP photoimagery.

To apply the CVA method, several processing steps were required (Figure 2). The Sentinel 2 images were downloaded at the level 2A (bottom of atmosphere reflectance), so no further radiometric nor atmospheric corrections were applied. We normalized both Sentinel 2 images to the range 0–1, as the normalization was noticed to enhance the detection of small-magnitude changes (Johnson and Kasischke 1998). To analyze only changes in forests, both images were clipped to the forest extent using the GFC treecover raster (representing the tree cover for year 2000). Then we calculated the multispectral difference image (DIFF) as follows:

$$\mathrm{DIFF} = \mathrm{post\_IM} - \mathrm{pre\_IM} \tag{1}$$

where:

DIFF – difference image,

post_IM – post-event image,

pre_IM – pre-event image.

The DIFF image consisting of 12 bands was a basis for computation of direction and magnitude rasters. The CVA method assumes the possibility of *drct* and *mgt* calculation for N-dimensional space (where a single dimension is considered as single DIFF band) (Solano-Correa et al. 2019; Dalponte et al. 2020). However, using two dimensions is recommended when detecting only one type of change and due to the simplicity and usability (Dalponte et al. 2020). Hence, we used two DIFF bands for each *drct* and *mgt* computation. The direction and magnitude rasters are calculated using the following equations:

$$drct = \mathrm{atan2}\left(B_1 / B_2\right) \tag{2}$$

$$mgt = \mathrm{sqrt}\left(B_1{}^2 + B_2{}^2\right) \tag{3}$$

where:

drct—direction,

mgt—magnitude,

B_1—first band applied for computation,

B_2—second band applied for computation.

Direction is initially computed in radians, and then converted to degrees on the interval 0–360. The pixels of the output direction and magnitude rasters were divided into blowdown/no blowdown classes using threshold values. However, this still leaves two significant questions:

1. How does band choice influence calculated direction and magnitude?
2. How does threshold choice influence mapping (and error in mapping) of the blowdown area?

We explored all possible variants of DIFF band pairs and thresholds. There were 66 possible combinations of DIFF band pairs, and hence, 66 possible *drct* and *mgt* rasters. To explore how band choice influences mapping error and accuracy, we took several steps: for each raster we (1) extracted maximal and minimal values, (2) tested the thresholds using the step of 0.1, for example, 0.1, 0.2, 0.3, etc. We classified all pixels higher than a given *mgt* threshold as a blowdown. For the *mgt* we did not use the upper threshold, as the data exploration showed that there is no need of doing so. In the case of direction, we computed the histogram and extracted the information about the intervals where most of the *drct* values occurred (*freq_dir*). Then, for the *freq_drct* we reclassified the direction raster using the classification intervals. Each of these intervals had an amplitude of 7, and the step between intervals was 1, for example, 1–7, 2–8, 3–9, etc. If the pixels were within the given classification interval, they were classified as a blowdown. We compared each classification output with the validation points based on NAIP data. For each case, we computed the number of true positives (TP), false positives (FP), false negatives (FN) and true negatives (TN) and calculated the true positives rate (TPR) and false positives rate (FPR). For both *drct* and *mgt*, we compared the results on the TPR-FPR plot and selected the cases with the possibly highest TPR and possibly lowest FPR. For simplicity, we show

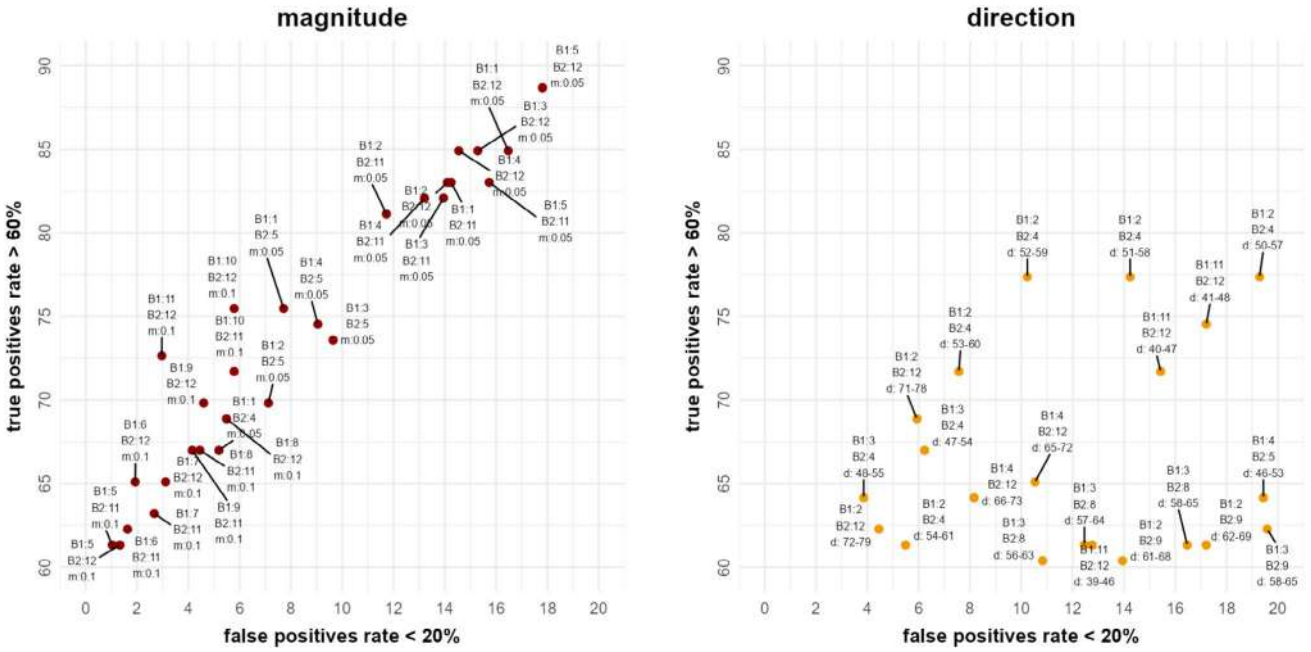

FIGURE 3 | The best cases of true positive rate and false positive rate for the magnitude and direction parameters. [Colour figure can be viewed at wileyonlinelibrary.com]

TABLE 1 | The true positive and false positive rates for CVA approach (based on Sentinel 2) and GFC data (based on Landsat).

CVA approach + parameters / GFC data	True positive rate (%)	False positive rate (%)
CVA output raster—bands: 11 and 12; $40 < drct < 47$; $mgt > 0.1$	66.04	0.89
CVA; bands: 11 and 12; $mgt > 0.1$	72.64	2.97
CVA; bands: 10 and 12; $mgt > 0.1$	75.47	5.79
CVA; bands: 5 and 12; $mgt > 0.05$	88.68	17.80
CVA; bands: 6 and 12; $mgt > 0.1$	65.09	1.93
CVA; bands: 3 and 4; $48 < drct < 55$	64.15	3.86
GFC data	66.98	2.97

Abbreviations: *drct*, direction; *mgt*, magnitude.

only cases with TPR > 60% and FPR < 20% (Figure 3). Visual inspection of the output rasters indicated that the *mgt* is better in accurate delineation of blowdown patches borders than the *drct*. Hence, based on the TPR-FPR plot for magnitude, we selected the *mgt* thresholds with TPR of 72.64% and FPR of 2.97%, that is, bands 11 and 12, $mgt > 0.1$ (Figure 3, Table 1). We chose this *mgt* output as it has the highest TPR of the outputs with a low FPR (< 4%). As we wanted to consider the *drct* in the final mapping output, we selected the direction thresholds having the lowest FPR for the same bands (11 and 12), that is, $40 < drct < 47$ (Figure 3, Table 1). Obtaining the band pairs and thresholds in that way, we created the output CVA blowdown map by adding the reclassified *drct* and *mgt* rasters and extracting only pixels satisfying simultaneously the conditions for *drct* and *mgt*. The windthrow mask was vectorized and its boundaries were simplified and smoothed (Figure 2). We applied a high-pass filter by computing the polygons area and deleting all polygons with an area smaller than the 3rd quantile of area. To provide possibly the highest accuracy, we compared the resulting blowdown mask with the NAIP orthophotomap and deleted several dozen of small polygons not related to the blowdown. Then, we converted the data to raster, labeling pixel values as 2 (blowdown) and 0 (no blowdown). We compared the CVA blowdown raster with the validation points and computed the TPR and FPR. These processes were automated in R (R Core Team 2024).

We compared the final CVA blowdown mapping raster with the Global Forest Change forest cover loss data version 1.10 (Hansen et al. 2013). These data are updated yearly since 2012. GFC version 1.10 provides information about the year of the forest cover loss, where the pixels are encoded as 0 (no loss) or 1–22 to label the forest cover loss detected in years 2001–2022, respectively. We were interested only in forest cover loss that occurred in 2020. The visual analysis of the GFC data and comparison with Sentinel data indicated most of the pixels representing the forest cover loss due to the 2020 blowdown were labelled as 21, and some as 20 on the GFC forest cover loss raster. Hence, we created the GFC damage raster by reclassifying the pixel values of 21 and 20 to 1 (damage), and the rest of the pixels to 0 (no damage). We resampled this raster to 10 m resolution using QGIS and bilinear interpolation for consistency with CVA. We evaluated the GFC damage raster using validation points and calculated the TPR and FPR. To compare the CVA and GFC output rasters, we created the comparison raster by adding them. The values of

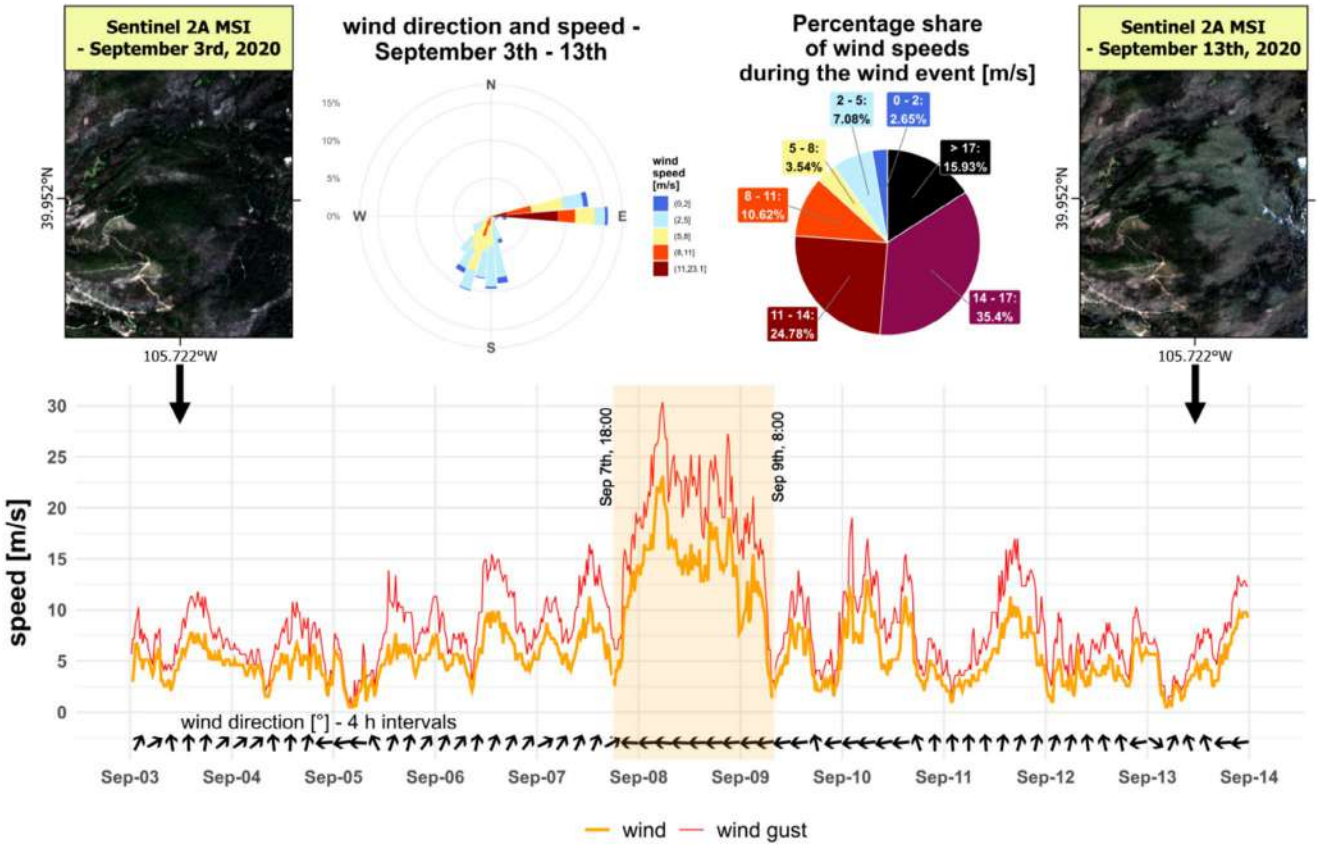

FIGURE 4 | The characteristics of the September 7th–9th wind event. Note the wind speed and direction change starting at 18:00 on September 7th. [Colour figure can be viewed at wileyonlinelibrary.com]

the comparison raster represented damages detected by both CVA and GFC (3), only by CVA (2), only by GFC (1) and no detected or without damage (0). We calculated the area occupied by each class, together with its percentage share (where 100% was the mapping area) (Figure 5).

2.2.3 | Terrain Analysis

For the terrain analysis, we considered three basic variables: elevation, slope, and aspect. We used the digital terrain model (DTM) with the 1-m spatial resolution provided by the United States Geological Survey (USGS 2024). The DTM was resampled to a 10-m resolution. We divided the entire mapping area into "blowdown" and "no blowdown" areas using the windthrow extent obtained in the mapping procedure. For these two areas, we presented the distribution of values of each analyzed variable using density plots. For slope and aspect, we calculated the statistical significance of differences between "blowdown" and "no blowdown" class. Due to the lack of normal distribution, we used the nonparametric Kruskal–Wallis test (Hollander and Wolfe 1973). The p value level was set to 0.05. To reduce the potential bias caused by the larger extent of "no blowdown" area (e.g., low elevation valleys), we took into consideration only the area located within 300 m from blowdown patch boundaries. In the case of elevation, which was similar between blowdown and non-blowdown points as a result of the above procedure, we present the descriptive statistics for "blowdown" and "no blowdown."

2.2.4 | Soil Disturbance Exploration

To quantify the relationship between soil disturbance and blowdown magnitude, we focused on tree size (DBH) and volume of soil disturbed. The field survey was carried out on only the road-accessible area of the blowdown area (9.4 ha patch) located in the central part of the AOI, at an altitude of 3070–3120 m a.s.l (Figure 1, Figure 8). We randomly selected 5-m radius plots, enough to encompass approximately 15 blown down mature trees per plot. We measured several parameters of the uprooted trees, that is, the tree fall direction, the diameter at breast height (DBH) and the root plate size. We measured three dimensions of each root plate (height, width, and depth), using the methodology described in (Godziek 2024). If a root plate was connected to multiple trees (e.g., neighboring trees fell together), we summed the basal areas of these trees. Because the sites could not be placed randomly within the blowdown extent due to accessibility, this data is illustrative only, and should not be considered a representative of the entire blowdown event.

3 | Results

3.1 | Windthrow Event Analysis

Sentinel data identified the September 3rd–September 13th, 2020 date range as the time of the event (clear before–after disturbance) (Figure 4). The analysis of the wind data

39:1691990239

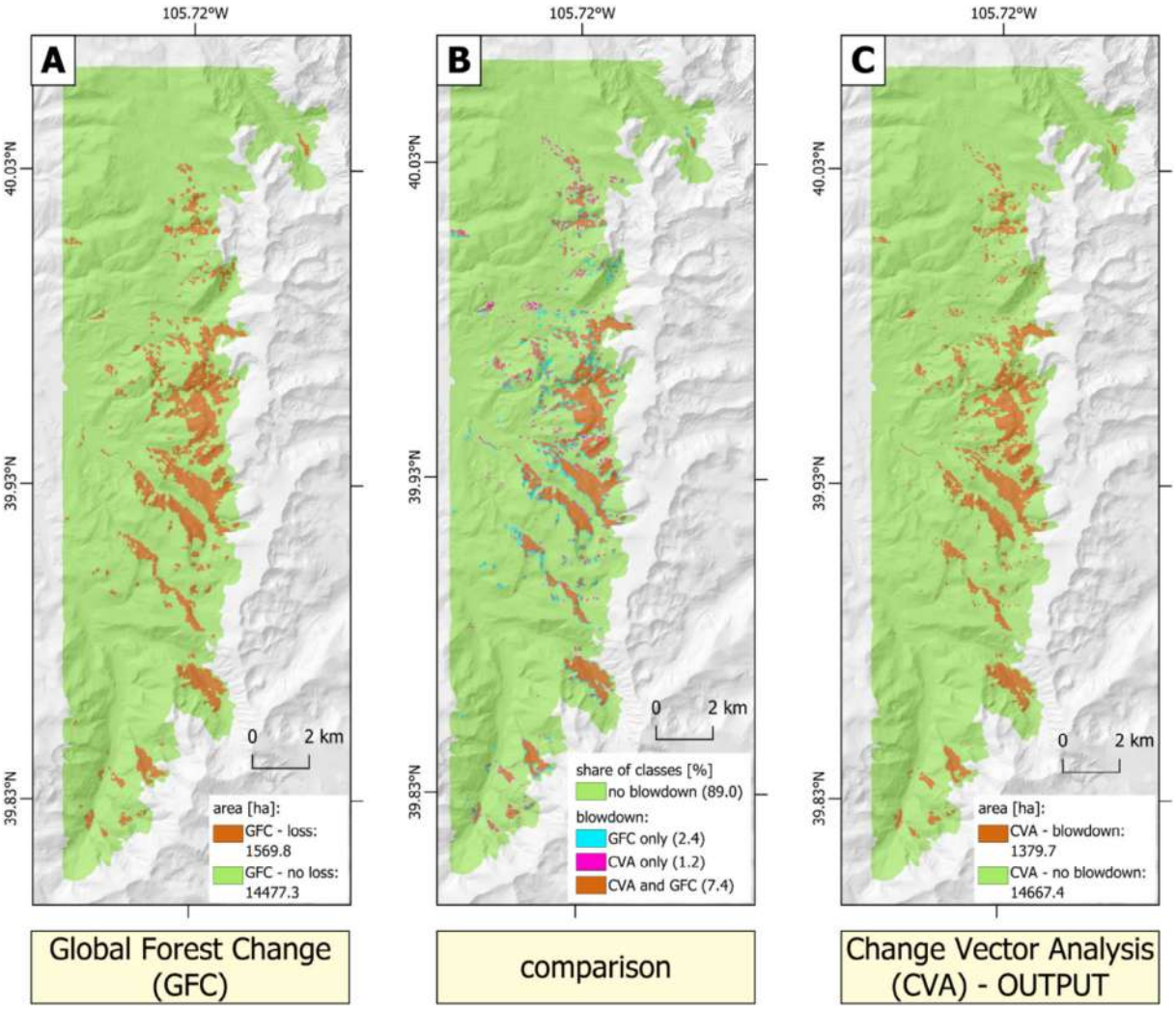

FIGURE 5 | Comparison between the mapping results (CVA technique) and Global Forest Change (GFC) data. [Colour figure can be viewed at wileyonlinelibrary.com]

from the Lunch Rock station showed that the highest wind speeds were recorded for the period between September 7th, 6:00 pm and September 9th, 8:00 am, that is, 40 h. During half of that period, the mean wind speed was above 14 $m \cdot s^{-1}$, and only for 1/10 of time was the mean wind speed below 5 $m \cdot s^{-1}$ (Figure 4); most of this period the wind gusts were above 20 $m \cdot s^{-1}$. For the entire period, the wind was blowing from the east. The highest wind speed was measured on September 8th at 5:40 am, reaching 23 $m \cdot s^{-1}$ with gusts to 30 $m \cdot s^{-1}$. Hence, the forest damage was caused by the strong wind event on September 7th, 8th, and 9th. High wind speed was associated with the passage of the cold front through Colorado on September 8th, 2020 (BoulderCAST Team 2024). The NAIP orthomap after that date clearly showed blowdown, with large areas of parallel fallen trees and no sign of any other disturbance agent.

3.2 | Windthrow Mapping

For the analysis of the TPR-FPR plots, we selected the cases with TPR > 60% and FPR < 20%, that is, 28 cases for magnitude and 21 cases for direction (Figure 3). To create the final CVA output blowdown raster, we used the bands 11 and 12 (short wave infrared), together with $40 < drct < 47$ and $mgt > 0.1$. This CVA output estimated the blowdown area to be 1379.7 ha, that is, 8.6% of the mapping area. The GFC data assessed the forest cover loss area to be 1569.8 ha (9.8% of the mapping area). The damage area detected by both CVA and GFC covered 1183.5 ha, approximately 7.4% of the mapping area (Figure 5).

We primarily focus on bands 11 and 12, as it was the best for mapping the blowdown extent (above). The TPR was nearly identical for both CVA output raster and GFC data (66%–67%), but the FPR was much lower for CVA output raster (0.89%) in comparison to GFC data (2.97%) (Table 1). In the case of the CVA technique, the TPR and FPR differed for selected band pairs and *mgt* and *drct* thresholds (Figure 3, Table 1). For the same input parameters as the CVA output raster, but without the *drct*, the TPR increased to 72.6%, with FPR of 2.7%. Generally, better results were obtained when using the magnitude parameter only, without the direction parameter (Figure 3, Table 1). The higher TPR (88.7%) was accompanied by a higher FPR (17.8%) for bands 5 and 12, and $mgt > 0.05$. The

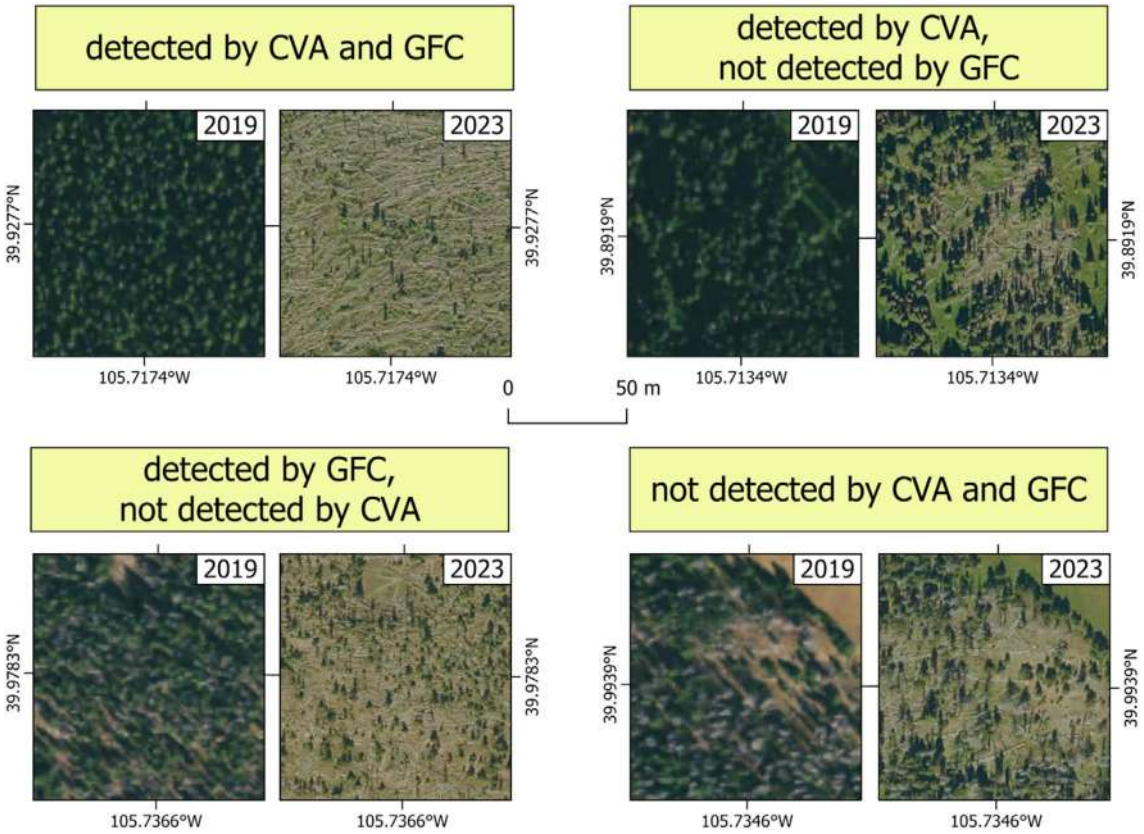

FIGURE 6 | Different cases of blowdown detection—CVA versus GFC. [Colour figure can be viewed at wileyonlinelibrary.com]

CVA technique was also able to obtain a similar TPR (65.1%, 64.2%) to GFC data, when using only magnitude or only direction (Table 1).

Blowdown patches generally followed the run of the valleys and ridges descending from the Continental Divide, that is, SE–NW. Large blowdown patches were also situated in the southern part of the mapping area (Figures 1 and 5). In the northern part of the mapping area, the patches were smaller and more dispersed (Figure 5). Within the mapping area, there were forest damage patches detected by both CVA and GFC, only by CVA, only by GFC, and by neither (Figure 6). Large patches were easily detected by both approaches. CVA was better at extracting the location of small patches with intensive damage. GFC indicated the location of patches with lower damage intensity, with numerous standing trees and a lower amount of fallen logs. We did note that some disturbance patches detected only by GFC were also related to other changes, for example, to house construction. Small patches, with dispersed fallen logs, standing healthy trees, and previous changes presumably related to beetle activity, were not always detected by GFC nor CVA (Figure 6).

3.3 | Terrain Analysis

For all three analyzed relief-related variables, there were differences in the distribution of their values for blowdown and no blowdown areas (Figure 7). Most of the blowdown patches occurred within the altitude interval of 3000–3300 m a.s.l, with the highest concentration within 3170–3250 m a.s.l. Not damaged forests were dominant at the altitudes below 3000 m a.s.l. and above 3350 m a.s.l. The descriptive statistics revealed the 1st qu., median, and the 3rd qu. were higher for blowdowns (3053, 3156, and 3239 m a.s.l.) than for not damaged forests (2952, 3098, and 3222 m a.s.l.). The distribution of slope for blowdown and no blowdown areas was similar, which was confirmed by the lack of statistical significance with $p = 0.098$. For aspect, there were significant differences between blowdown and no blowdown areas, with $p < 0.0001$. Blowdown patches frequently occupied North-eastern slopes, within the exposition azimuth range of 15°–50°. Blowdown areas were also quite frequent on North and Northwestern slopes (Figure 7).

3.4 | Fieldwork and Soil Disturbance

Fieldwork was located in the main accessible stand, which experienced nearly 100% mortality and contained dispersed snags and rare occurring living trees (Figure 8). Species included both Engelmann spruce and lodgepole pine. Most of the trees were uprooted (Figure 8A–C); however, some were snapped. Other blowdown patches were clearly visible from the Winter Park–Rollins Pass road (Figure 8D,E), as well as from Hwy 40 (Figure 8F). We measured 60 root plates, of which five were created by the fall of two trees, and three by three trees. Most of the measured root plates had a volume of 0.1–0.8 m^3. There were also a lot of small root plates with a volume below 0.1 m^3. In two cases, there were root systems

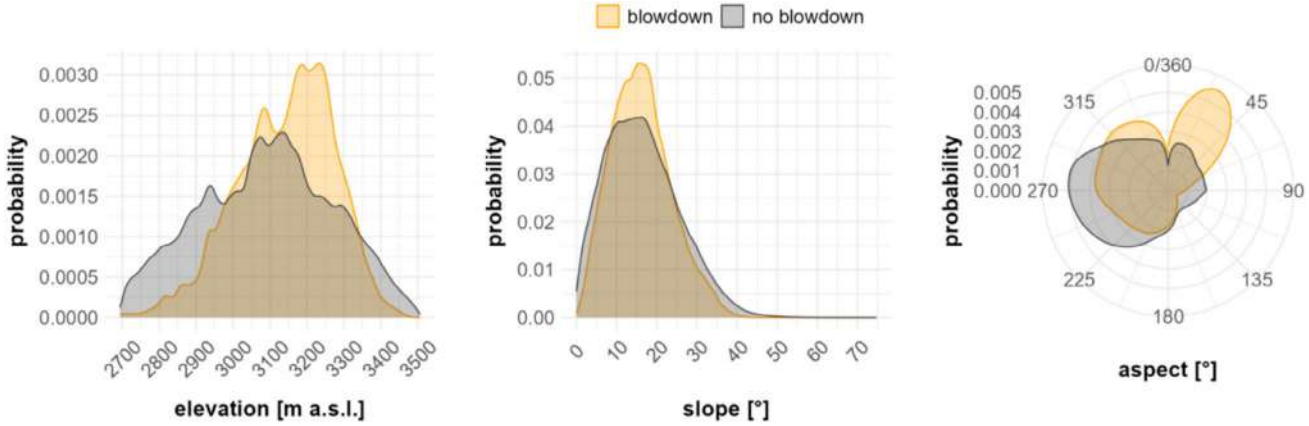

FIGURE 7 | The distribution of elevation, slope, and aspect values for blowdown and no blowdown areas. [Colour figure can be viewed at wileyonlinelibrary.com]

without soil (recorded as volume of 0 m^3). The largest root plate had a volume of 1.29 m^3 and was related to two trees. The root plate size was directly proportional to the fallen tree (or trees) basal area, with $R^2 = 0.7$ (Figure 8). We measured the azimuth of 75 fallen logs (71 related to root plates, and 4 snapped). Nearly all logs toppled in the NW, SW, or W direction, and the most frequent azimuth intervals were 275–305 and 245–255 (Figure 8).

4 | Discussion

4.1 | The Analyzed Blowdown Event in the Light of Previous Blowdowns in Colorado and Worldwide

Wind-driven disturbance should not be underestimated in the region, which is more well known for fires (Lindemann and Baker 2001; Buma and Wessman 2011; Momodu 2019). There are many examples of small-scale blowdowns across the CFR, such as within Rocky Mountain NP (Veblen et al. 1989; Veblen 2000; Wohl 2013; Fujita 1989). Large-scale blowdowns are infrequent, but still important ecologically in the CFR (Veblen 2000; Kulakowski and Veblen 2002, 2007). They are usually associated with the occurrence of unusual meteorological conditions (e.g., unusual wind directions, Poulos et al. 2002; Meyers et al. 2003). These events are rare but not unprecedented.

The 1997 Routt Forest blowdown is the only well described large-scale windthrow event in the southern Rockies similar to the one analyzed in this paper (Lindemann and Baker 2001; Kulakowski and Veblen 2002; Poulos et al. 2002; Meyers et al. 2003). The 1997 blowdown was caused by a powerful winter storm which lasted over 3 days of 24th—26th October. The event was caused by the deep, cutoff low pressure system, which led to long-lasting, anomalous, and strong easterly winds over some parts of the Colorado Rocky Mountains (Poulos et al. 2002). The September 7th—9th 2020 windstorm analyzed here shares a few similarities with the 1997 event, that is, (1) the cold front moving southwards in the late summer/early autumn (September and October), (2) strong, anomalous easterly winds, and (3) greater precipitation and snowfall on the eastern side of the Continental Divide in comparison to the western side (Poulos et al. 2002; Colorado Climate Center 2024). Both easterly winds and precipitation predominantly on eastern aspects are unusual, as westerly winds prevail in the region (Pepin 2000; Poulos et al. 2002; Sheppard et al. 2002).

Severity and snowfall differed between the two events. In 1997, the peak wind gusts recorded close to the windthrow area reached up to 51 $m \cdot s^{-1}$ (Poulos et al. 2002), while in 2020, speeds were less, up to 30 $m \cdot s^{-1}$ (Winter Park 2024), though we note the observation station is not located directly inside the blowdown area. During the 1997 windstorm, over 150 cm of snow was recorded on the CFR foothills (Poulos et al. 2002), while during the 2020 event, the CFR foothills obtained 8–22 cm of snow (BoulderCAST Team 2024). Damage was also less in the event studied here. The 1997 event damaged > 10,000 ha of forest (Lindemann and Baker 2001; Kulakowski and Veblen 2002) vs. our estimate of > 1300 ha of forest for 2020 event (Figure 5). However, the events cannot be perfectly compared due to differing soils, topography, and other factors which played a role in forest blowdown occurrence.

We suggest the most important factor both events have in common was the unusually strong easterly winds. During both events the easterly winds were > 20 $m \cdot s^{-1}$ and lasted for several hours (Poulos et al. 2002) (Figure 4). Blowdown likelihood in these conditions may be higher due to root systems being unadapted to the rare wind direction (Quine and Gardiner 2007; Moore 2014). Root systems (and presumably tree stability) are known to be correlated with dominant wind directions (Danjon et al. 2005). Hence, an unusual wind direction presumably increases the likelihood of blowdown occurrence (Meyers et al. 2003; Quine and Gardiner 2007). The consistent direction of the fallen trees (Figure 8) supports this hypothesis, as they essentially all fell in the same direction consistent with easterly wind. The proximity of the high montane ridge (the Continental Divide, in this case) also generates higher localized wind speeds by funneling air through low passes in the ridge (Miller and Durran 1991; Sun 2013), with possible functioning of anemo-orographic systems (Jeník 1961). There are many examples of similar dynamics in mountains worldwide (McGowan 1997; Nkemdirim 1997; Richner and Hächler 2013; Lepri et al. 2017). Both 1997 and 2020 blowdowns formed on the western slopes adjacent to the Continental Divide. It is important to note that forest conditions may also condition a location

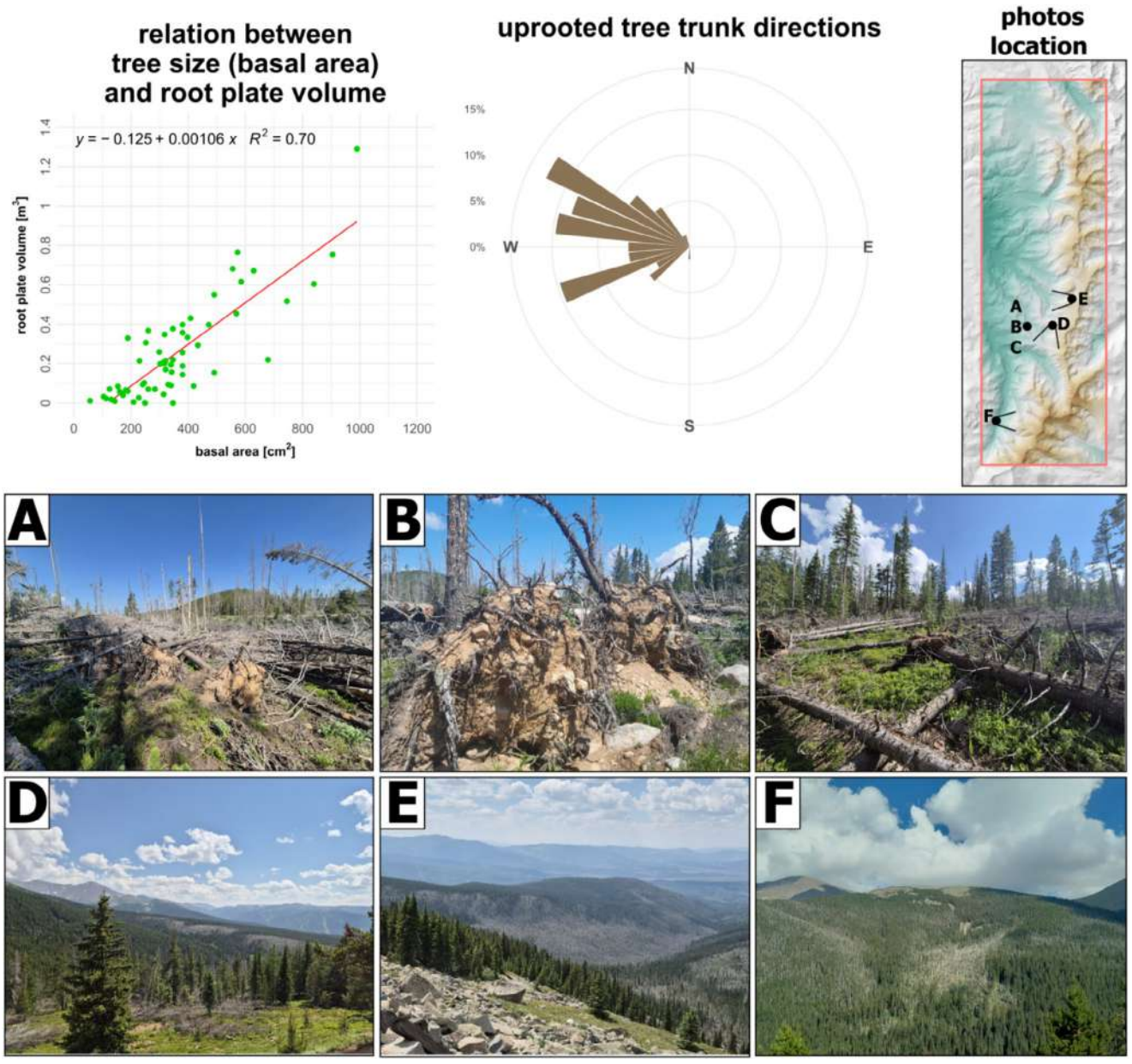

FIGURE 8 | The results of the fieldwork (Photo. J. Godziek). [Colour figure can be viewed at wileyonlinelibrary.com]

for blowdown. As disturbance ecology studies often reveal, especially for large events, we cannot eliminate the potential that some pre-existing condition (e.g., bark beetle damage, Tishmack et al. 2005; Lester 2020) made these sites more likely to blow down. However, in this case there was no record of significant insect mortality prior to the blowdown.

4.2 | Issues Related to Automatic Windthrow Detection

The tunable CVA methodology appears valuable for blowdown mapping. Both CVA and GFC techniques identified most of the big blowdown patches, with the TPR of 66%–67% limited mainly by undetected small patches. Identification of the smallest patches was further limited by the resolution of the datasets (10 m and 30 m, respectively). When comparing to GFC data, using the CVA technique with both *mgt* and *drct* parameters lowered the FPR for windthrow detection by about 3 times (0.89% vs. 2.97%; Table 1). False positives can be a significant problem in disturbance analysis (Forbes 1995), so even small decreases in the FPR are valuable for blowdown mapping. Further, a low FPR is important for conservative conclusions, as it reduces the risk of spurious correlations. This may be the advantage of the CVA approach over the GFC data. The similar level of TPR (66%–67%; Table 1) for the output CVA blowdown map and GFC forest cover loss product is related to (1) the selected bands and thresholds on *mgt* and *drct* for CVA, and (2) the way the GFC algorithm works (Hansen et al. 2013).

Determining the classification parameters is crucial for CVA performance (Solano Correa et al. 2014). The multiple metric (direction and magnitude), vector-based CVA analysis indicated the changes within the mapping area were caused by

blowdown only. As the direction provides information about the type of change, for example, blowdown, wildfire, logging, etc. (Solano Correa et al. 2014; Dalponte et al. 2020), we targeted values aimed at extracting the values of the direction parameter optimal for blowdown detection. We note that if one assumes all changes are caused by the same disturbance event, the magnitude parameter representing the amount of changes can be sufficient (Bovolo and Bruzzone 2007). Testing the CVA using only the magnitude parameter revealed a higher TPR (up to 88.7%), which was, however, frequently accompanied by an FPR increase (up to 17.8%; Table 1). Without the direction parameter, the TPR would rise to 72.6% (higher than the GFC dataset), with the FPR increasing to a level similar to GFC data (Table 1). Computing the direction parameter gives additional information helpful to lower the FPR (Table 1). The larger value of the CVA methodology is the tunability—the ability to adjust the FPR and TPR to the task at hand. Testing different cases of parameters for CVA (Figure 3) illustrates the potential of (1) adjusting the CVA to the particular detection problem, and (2) selecting the CVA settings depending on the goal of the analysis. To maximize the CVA performance, we recommend analyzing images from the same vegetation season and with minimal or no cloud cover. To date, research on RS-based windthrow detection methods has been conducted mostly in Europe (Einzmann et al. 2017; Tanase et al. 2018; Dalponte et al. 2020; Senf and Seidl 2021; Bonannella et al. 2024). Also, other types of disturbances (wildfires, bark beetle outbreaks) have been studied using RS data and CVA in Euroasia and Africa (Adelabu et al. 2012; Verde and Tsakiri-Strati 2014; Santi et al. 2022). Hence, our research is unique as it applies RS data and CVA in Northern America.

The Global Forest Change dataset is obtained by analyzing the timeseries of Landsat imagery and employing a set of metrics considering the statistical description of reflectance values and the image acquisition time (Hansen et al. 2013). The value of the GFC data is its global coverage and automatic algorithm. (Galiatsatos et al. 2020). GFC data may face different inaccuracies resulting from (1) the processing and classification methods, and (2) the input data, that is, their resolution, acquisition date, cloudiness, etc. (Potapov et al. 2015; Galiatsatos et al. 2020). Also, the forest loss year data can be inaccurate, as a small part of the September 2020 blowdown was attributed to 2020 by the GFC, and a larger part to 2021 (University of Maryland 2022; European Space Agency (ESA) 2024). Such inaccuracies may result from data-related factors, such as the acquisition dates, data availability, or high cloud cover percentage after September 2020. GFC data also lack the information about the origin of forest disturbance, which is crucial for many applications (Sturtevant and Fortin 2021).

The CVA approach has been used in previous studies related to windthrow mapping (Vorovencii 2014; Dalponte et al. 2020), and for other applications, including fire detection, and vegetation, wetland, and agriculture monitoring (Johnson and Kasischke 1998; Roemer et al. 2010; Singh and Talwar 2014). This study applied the CVA for a new case study, related to different environmental conditions than the previous research. This approach should be useful for multiple disturbance types, such as fires, the mapping of blowdowns and other features related to the changes between two images, such as any type of forest disturbances, mass movements (landslides, debris flows), land use change, etc. (Lambin and Strahlers 1994; Chen et al. 2011).

We were able to test the workflow proposed by Dalponte et al. (2020) for the Italian Alps in the Rocky Mountains of North America. However, we note several differences in our workflow and the steps performed by Dalponte et al. (2020). We did not have blowdown maps provided by the forest service, which could be relevant for use as validation data. Therefore, we prepared our own validation dataset from very high spatial resolution photos (the NAIP imagery). We also used our validation dataset to check the performance of the method, without dividing the AOI into training and test sets. The detection thresholds applied to map the blowdown in this study vary from the ones used by (Dalponte et al. 2020). These differences can be related to (1) different distribution of pixel values within the satellite image bands and (2) different environmental conditions (variation of climatic and vegetation zones). Hence, the CVA technique is not yet suitable for unsupervised or automated detection. Despite this limitation, the CVA has many advantages, as this method (1) is unsupervised and hence does not require a training dataset and (2) is not computationally demanding for small and medium-sized study areas. The workflow we shared in R (Supporting Information, R Script) can be easily adapted to other forest disturbances.

4.3 | Insights Related to Terrain Analysis and Soil Disturbance

The blowdown was concentrated within a relatively narrow altitudinal belt. Such events often result in high-speed winds hitting the surface of the mountain slope within a constrained elevation range, driven by the combination of ridge elevation, topography, and meteorological conditions (Kwiatkowski 1969; Sun 2013). This results in severe damage within this belt, while forests growing at higher and lower elevations remain untouched (Miller and Durran 1991). A well-documented example is the large scale, but elevationally constrained, 2004 blowdown on southern slopes of the Slovakian Tatra Mts. due to northern bora-type wind (Simon et al. 2015; Balon and Maciejewski 2005). In the case of the 2020 blowdown, intense downslope winds likely occurred on the leeward side, especially through small gaps or low points in the ridge (Miller and Durran 1991; Sun 2013). There are many such low points on the ridge of the Continental Divide, mostly located in the central part of the AOI, between Jasper Peak and James Peak (Figure 1). This may be the cause of the presence of multiple large blowdown patches in the central part of the mapping area (Figure 5). The large blowdown patches in the valleys in the southern part of the mapping area can be related to the impact of wind blowing through local low points in the main ridge. In this case, deep valleys surrounded by high ridges might force the strong wind currents to hit the ground at local flattenings in the valley bottom. Slope did not appear to have a meaningful effect ($p = 0.098$) on the spatial distribution of blowdown patches (Figure 7), which was unexpected. However, the high share of blowdown patches on NE aspects reflects the overall wind direction. The strip-shaped blowdown patches in the central part of the AOI follow the run of the ridges, with wind damage located at NE slopes (Figure 5). If these major blowdowns are associated with easterly winds, as suggested by this event and the Routt event,

it may be feasible to explain blowdown patches distribution as a function of topography. More research is needed, especially a focus on finding analogous, high-elevation easterly wind events that did or did not produce similar blowdown events.

Soil disturbance cannot be well assessed from satellite data at present. Orthophotomaps, despite a much higher spatial resolution, are not acquired often enough to support recognition of changes at the level of individual trees, for example, whether a tree has been uprooted or broken. Field surveys are often required, and notably also provide substantial contextual data generally unavailable from satellites (e.g., species, damage type, etc.: Pawlik et al. 2016; Phillips et al. 2017). We presume the 2020 blowdown disturbed a great amount of soil, as most of the trees surveyed were uprooted rather than broken (which would not disturb the soil). The estimated root plate volumes fit into the volume range documented by recent research (Gallaway et al. 2009; Phillips et al. 2008; Strzyżowski et al. 2018). The measured root plates are small compared to European root plates (Šamonil et al. 2009; Pawlik 2013; Godziek 2024), likely due to tree species and a generally smaller tree size and thinner soils at high elevations, though unknown prior (historical) disturbances which may have driven smaller tree sizes cannot be excluded. The comparison between the tree size (basal area) and root plate volume did show a strong correlation between those two variables (Figure 8). This agrees with other wind-soil studies (Schaetzl et al. 1989; Pawlik 2013). The specifics of the CFR subalpine forest blowdown are many root plates being related to more than one tree. This may result from the small size of conifers and too small distances between trees (Veblen et al. 1991), or soil conditions at the time of the event. Although the number of measured plots is small, the collected data provide valuable insight into the impact of the CFR blowdown on soil disturbance and tree fall direction.

5 | Conclusions

Wind-driven disturbances can be significant, even where they are not considered a dominant disturbance type, such as the Rocky Mountains. We explored in detail a large-scale blowdown event in the Colorado Front Range. Strong winds from an unusual direction seem to be crucial to the blowdown formation.

Methodologically, the blowdown mapping approach used is the first application of the CVA method for forest damage detection in the North American context. The approach is entirely based on the open data and scripting language available for future users, which secures the possibility of testing the method in other environmental conditions. Our mapping approach achieved high true positive detection accuracy and a lower false positive rate than the commonly used GFC data. Importantly, it is tunable to study-specific needs like maximizing or minimizing false positives, true negatives, or other goals. The presented method can be easily applied and does not require a training dataset, which for some areas can be challenging to obtain (with no orthophotomaps or detailed forest maps). The 2020 CFR blowdown was primarily associated with exposed aspects within a relatively narrow elevational band and caused soil disturbance, with root plates smaller than those measured in Europe. Our study presents a useful methodology for further investigations on (1) blowdown mapping techniques using RS data, (2) a means to improve on the accuracy of GFC data, (3) factors leading to blowdown formation in the Rocky Mts., (4) blowdown-related soil disturbance, and (5) the interplay between potentially damaging high wind currents and local and regional topography.

Acknowledgments

This study was supported by the Polish National Science Centre—Narodowe Centrum Nauki (grant no. 2019/35/O/ST10/00032) and by the Polish National Agency for Academic Exchange—Narodowa Agencja Wymiany Akademickiej (internship agreement no. PPN/STA/2021/1/00081/U/00001). The authors would like to thank Brendan Irving from the Winter Park Ski Resort for sharing the meteorological data. The authors would also like to thank two anonymous reviewers for providing insightful comments that significantly improved the quality of the manuscript. The authors are grateful to Izabela Godziek for the help during the fieldwork.

Data Availability Statement

The data that support the findings of this study are available from the corresponding author upon reasonable request.

References

Adelabu, S., O. Mutanga, and M. A. Cho. 2012. "A Review of Remote Sensing of Insect Defoliation and Its Implications for the Detection and Mapping of Imbrasia Belina Defoliation of Mopane Woodland." *African Journal of Plant Science and Biotechnology* 6: 1–13.

Alexander, R. R. 1964. "Minimizing Windfall Around Clear Cuttings in Spruce-Fir Forests." *Forest Science* 10: 130–142.

Baker, W. L., and T. T. Veblen. 1990. "Spruce Beetles and Fires in the Nineteenth-Century Subalpine Forests of Western Colorado, U.S.A." *Arctic and Alpine Research* 22: 65. https://doi.org/10.2307/1551721.

Balon, J., and W. Maciejewski. 2005. "Wpływ Huraganowego Wiatru z Dnia 19 Listopada 2004 na Krajobraz Południowego Skłonu Tatr." *Problemy Ekologii Krajobrazu* 17: 92–100. (In Polish).

Bigler, C., D. G. Gavin, D. G. Gavin, et al. 2007. "Drought Induces Lagged Tree Mortality in a Subalpine Forest in the Rocky Mountains." *Oikos* 116: 1983–1994. https://doi.org/10.1111/j.2007.0030-1299.16034.x.

Bonannella, C., L. Parente, S. de Bruin, and M. Herold. 2024. "Multi-Decadal Trend Analysis and Forest Disturbance Assessment of European Tree Species: Concerning Signs of a Subtle Shift." *Forest Ecology and Management* 554: 121652.

BoulderCAST Team. 2024. "Hot, Cold and Snowy: A Look Back at the Record-Shattering Wild Week of Summer Weather." https://bouldercast.com/hot-cold-snowy-a-recap-of-our-record-shattering-wild-week-of-summertime-weather/.

Bovolo, F., and L. Bruzzone. 2007. "A Theoretical Framework for Unsupervised Change Detection Based on Change Vector Analysis in the Polar Domain." *IEEE Transactions on Geoscience and Remote Sensing* 45: 218–236. https://doi.org/10.1109/TGRS.2006.885408.

Buma, B. 2015. "Disturbance Interactions: Characterization, Prediction, and the Potential for Cascading Effects." *Ecosphere* 6, no. 4: 1–15. https://doi.org/10.1890/ES15-00058.1.

Buma, B., and C. A. Wessman. 2011. "Disturbance Interactions Can Impact Resilience Mechanisms of Forests." *Ecosphere* 2: art64. https://doi.org/10.1890/ES11-00038.1.

Byrne, K. E., and S. J. Mitchell. 2007. "Overturning Resistance of Western Redcedar and Western Hemlock in Mixed-Species Stands in Coastal

British Columbia." *Canadian Journal of Forest Research* 37: 931–939. https://doi.org/10.1139/X06-291.

Bzowski, M., and J. Dziewolski. 1973. "Damages Caused by Foehn in the Spring of 1968 in Forests of the Tatra National Park." *Ochrona Przyrody* 38: 115–154.

Calder, W. J., and B. Shuman. 2017. "Extensive Wildfires, Climate Change, and an Abrupt State Change in Subalpine Ribbon Forests, Colorado." *Ecology* 98: 2585–2600. https://doi.org/10.1002/ecy.1959.

Chen, J., X. Chen, X. Cui, and J. Chen. 2011. "Change Vector Analysis in Posterior Probability Space: A New Method for Land Cover Change Detection." *IEEE Geoscience and Remote Sensing Letters* 8: 317–321. https://doi.org/10.1109/LGRS.2010.2068537.

Colorado Climate Center. 2024. *Access Colorado Data*. Colorado State University. https://climate.colostate.edu/data_access_new.html.

Dalponte, M., S. Marzini, Y. T. Solano-Correa, G. Tonon, L. Vescovo, and D. Gianelle. 2020. "Mapping Forest Windthrows Using High Spatial Resolution Multispectral Satellite Images." *International Journal of Applied Earth Observation and Geoinformation* 93: 102206. https://doi.org/10.1016/j.jag.2020.102206.

Dalponte, M., Y. T. Solano-Correa, D. Marinelli, S. Liu, N. Yokoya, and D. Gianelle. 2023. "Detection of Forest Windthrows With Bitemporal COSMO-SkyMed and Sentinel-1 SAR Data." *Remote Sensing of Environment* 297: 113787. https://doi.org/10.1016/j.rse.2023.113787.

Danjon, F., T. Fourcaud, and D. Bert. 2005. "Root Architecture and Wind-Firmness of Mature *Pinus pinaster*." *New Phytologist* 168: 387–400. https://doi.org/10.1111/j.1469-8137.2005.01497.x.

Denman, S., N. Brown, E. Vanguelova, and B. Crampton. 2022. "Temperate Oak Declines: Biotic and Abiotic Predisposition Drivers." In *Forest Microbiology*, edited by F. O. Asiegbu and A. Kovalchuk, 239–263. Elsevier. https://doi.org/10.1016/B978-0-323-85042-1.00020-3.

Doane, T. H., D. Edmonds, B. J. Yanites, and Q. Lewis. 2021. "Topographic Roughness on Forested Hillslopes: A Theoretical Approach for Quantifying Hillslope Sediment Flux From Tree Throw." *Geophysical Research Letters* 48: e2021GL094987. https://doi.org/10.1029/2021GL094987.

Dobbertin, M. 2002. "Influence of Stand Structure and Site Factors on Wind Damage Comparing the Storms Vivian and Lothar." *Forest Snow and Landscape Research* 19: 187–205.

Einzmann, K., M. Immitzer, S. Böck, O. Bauer, A. Schmitt, and C. Atzberger. 2017. "Windthrow Detection in European Forests With Very High-Resolution Optical Data." *Forests* 8: 21. https://doi.org/10.3390/f8010021.

European Space Agency (ESA). 2024. "Sentinel-2A MSI Level-2A. Distributed by Copernicus Data Space Ecosystem." https://dataspace.copernicus.eu/.

Everham, E. M., and N. V. L. Brokaw. 1996. "Forest Damage and Recovery From Catastrophic Wind." *Botanical Review* 62: 113–185. https://doi.org/10.1007/BF02857920.

Forbes, A. D. 1995. "Classification-Algorithm Evaluation: Five Performance Measures Based Onconfusion Matrices." *Journal of Clinical Monitoring* 11: 189–206. https://doi.org/10.1007/BF01617722.

Forzieri, G., M. Pecchi, M. Girardello, et al. 2020. "A Spatially Explicit Database of Wind Disturbances in European Forests Over the Period 2000–2018." *Earth System Science Data* 12: 257–276. https://doi.org/10.5194/essd-12-257-2020.

Fujita, T. T. 1989. "The Teton-Yellowstone Tornado of 21 July 1987." *Monthly Weather Review* 117: 1913–1940.

Galiatsatos, N., D. N. M. Donoghue, P. Watt, et al. 2020. "An Assessment of Global Forest Change Datasets for National Forest Monitoring and Reporting." *Remote Sensing* 12: 1790. https://doi.org/10.3390/rs12111790.

Gallaway, J. M., Y. E. Martin, and E. A. Johnson. 2009. "Sediment Transport due to Tree Root Throw: Integrating Tree Population Dynamics, Wildfire and Geomorphic Response." *Earth Surface Processes and Landforms* 34: 1255–1269. https://doi.org/10.1002/esp.1813.

Gardiner, B. 2021. "Wind Damage to Forests and Trees: A Review With an Emphasis on Planted and Managed Forests." *Journal of Forest Research* 26: 248–266. https://doi.org/10.1080/13416979.2021.1940665.

Godziek, J. 2024. "Root Plates of Uprooted Trees – Automatic Detection and Biotransport Estimation Using LiDAR Data and Field Mapping." *International Journal of Applied Earth Observation and Geoinformation* 131: 103992. https://doi.org/10.1016/j.jag.2024.103992.

Godziek, J., and Ł. Pawlik. 2023. "Indicators of Wind-Driven Forest Disturbances – Pit–Mound Topography, Its Automatic Detection and Significance." *Catena* 221: 106757. https://doi.org/10.1016/j.catena.2022.106757.

Hansen, M. C., P. V. Potapov, R. Moore, et al. 2013. "High-Resolution Global Maps of 21st-Century Forest Cover Change." *Science* 342: 850–853. https://doi.org/10.1126/science.1244693.

Havašová, M., J. Ferenčík, and R. Jakuš. 2017. "Interactions Between Windthrow, Bark Beetles and Forest Management in the Tatra National Parks." *Forest Ecology and Management* 391: 349–361. https://doi.org/10.1016/j.foreco.2017.01.009.

Henderson, D. E., J. B. Milford, and S. L. Miller. 2005. "Prescribed Burns and Wildfires in Colorado: Impacts of Mitigation Measures on Indoor Air Particulate Matter." *Journal of the Air and Waste Management Association (1995)* 55: 1516–1526. https://doi.org/10.1080/10473289.2005.10464746.

Hollander, M., and D. A. Wolfe. 1973. *Nonparametric Statistical Methods*. John Wiley & Sons.

Ilies, G., M. Ilies, M. Hotea, et al. 2022. "Integrating Forest Windthrow Assessment Data in the Process of Windscape Reconstruction: Case of the Extratropical Storms Downscaled for the Gutai Mountains (Romania)." *Frontiers in Environmental Science* 10: 926430. https://doi.org/10.3389/fenvs.2022.926430.

Iwamoto, K., S. Ugawa, M. Araki, D. Kabeya, M. Ishizuka, and T. Kajimoto. 2018. "Changes of Above- and Below-Ground Biomass Forty-Three Years After a Typhoon Disturbance in a Subalpine Wave Regeneration Forest on Mt. Shimagare." https://doi.org/10.20756/ffpri.17.2_117.

Jeník, J. 1961. *Alpinská Vegetace Krkonoš, Králického Sněžníku a Hrubého Jeseníku: Teorie Anemo-Orografických Systémů*. Československá Akademie Věd.

Jenkins, J. 1995. "Notes on the Adirondack Blowdown of July 15th, 1995—Scientific Background, Observations, and Policy Issues." Wild Life Conservation Society.

Johnson, R. D., and E. S. Kasischke. 1998. "Change Vector Analysis: A Technique for the Multispectral Monitoring of Land Cover and Condition." *International Journal of Remote Sensing* 19: 411–426. https://doi.org/10.1080/014311698216062.

Kenderes, K., R. Aszalós, J. Ruff, Z. Barton, and T. Standovár. 2007. "Effects of Topography and Tree Stand Characteristics on Susceptibility of Forests to Natural Disturbances (Ice and Wind) in the Börzsöny Mountains (Hungary)." *Community Ecology* 8: 209–220. https://doi.org/10.1556/ComEc.8.2007.2.7.

Knight, D. H. 1994. *Mountains and Plains: The Ecology of Wyoming Landscapes*. Yale Univ. Press.

Kulakowski, D., and T. T. Veblen. 2002. "Influences of Fire History and Topography on the Pattern of a Severe Wind Blowdown in a Colorado Subalpine Forest." *Journal of Ecology* 90: 806–819. https://doi.org/10.1046/j.1365-2745.2002.00722.x.

Kulakowski, D., and T. T. Veblen. 2007. "Effects of Prior Disturbances on the Extent and Severity of Wildfire in Colorado Subalpine Forests." *Ecology* 88: 759–769. https://doi.org/10.1890/06-0124.

Kwiatkowski, J. 1969. “Klimatologiczna Geneza Wyłomów Leśnych w Karkonoszach.” *Czasopismo Geograficzne* 40, no. 3: 365–373. (In Polish).

Lambin, E. F., and A. H. Strahlers. 1994. “Change-Vector Analysis in Multitemporal Space: A Tool to Detect and Categorize Land-Cover Change Processes Using High Temporal-Resolution Satellite Data.” *Remote Sensing of Environment* 48: 231–244. https://doi.org/10.1016/0034-4257(94)90144-9.

Lazecky, M., S. Wadhwa, M. Mlcousek, and J. J. Sousa. 2021. “Simple Method for Identification of Forest Windthrows From Sentinel-1 SAR Data Incorporating PCA.” *Procedia Computer Science* 181: 1154–1161. https://doi.org/10.1016/j.procs.2021.01.312. CENTERIS 2020—International Conference on ENTERprise Information Systems/ProjMAN 2020—International Conference on Project MANagement/HCist 2020—International Conference on Health and Social Care Information Systems and Technologies 2020, CENTERIS/ProjMAN/HCist 2020.

Lepri, P., Z. Vecenaj, H. Kozmar, and B. Grisogono. 2017. “Bora Wind Characteristics for Engineering Applications.” *Wind Engineering and Structural Dynamics* 24: 579–611. https://doi.org/10.12989/WAS.2017.24.6.579.

Lester, M. B. 2020. *2019 Report on the Health of Colorado's Forests*. Colorado State Forest Service.

Lindemann, J. D., and W. L. Baker. 2001. “Attributes of Blowdown Patches From a Severe Wind Event in the Southern Rocky Mountains, USA.” *Landscape Ecology* 16: 313–325.

Mahoney, M. 2024. “rsi: Efficiently Retrieve and Process Satellite Imagery.” https://doi.org/10.32614/CRAN.package.rsi.

Martin, T. J., and J. Ogden. 2006. “Wind Damage and Response in New Zealand Forests: A Review.” *New Zealand Journal of Ecology* 30: 16.

Mayer, P., P. Brang, M. Dobbertin, et al. 2005. “Forest Storm Damage is More Frequent on Acidic Soils.” *Annals of Forest Science* 62: 303–311. https://doi.org/10.1051/forest:2005025.

McGowan, H. A. 1997. “Meteorological Controls on Wind Erosion During Foehn Wind Events in the Eastern Southern Alps, New Zealand.” *Canadian Journal of Earth Sciences* 34: 1477–1485. https://doi.org/10.1139/e17-120.

Meng, Y., L. Zhou, W. Zhou, et al. 2015. “Characteristics of Plant Species Diversity in a Windthrow Area on Changbai Mountain After 26 Years of Natural Recovery.” *Acta Ecologica Sinica* 35: 142–149. https://doi.org/10.5846/stxb201405301109.

Meyers, M. P., J. S. Snook, D. A. Wesley, and G. S. Poulos. 2003. “A Rocky Mountain Storm. Part II: The Forest Blowdown Over the West Slope of the Northern Colorado Mountains—Observations, Analysis, and Modeling.” *Weather and Forecasting* 18: 662–674. https://doi.org/10.1175/1520-0434(2003)018<0662:armspi>2.0.co;2.

Miller, P. P., and D. R. Durran. 1991. “On the Sensitivity of Downslope Windstorms to the Asymmetry of the Mountain Profile.” *Journal of the Atmospheric Sciences* 48, no. 12: 1457–1473. https://doi.org/10.1175/1520-0469(1991)048<>2.0.CO;2.

Mitchell, S. J. 2013. “Wind as a Natural Disturbance Agent in Forests: A Synthesis.” *Forestry* 86: 147–157. https://doi.org/10.1093/forestry/cps058.

Momodu, P. A. 2019. “Terrain Susceptibility to Windthrow of Trees in Subalpine Forests, Canadian Rockies.”

Moore, G. M. 2014. “Wind-Thrown Trees: Storms or Management?” *Arboriculture and Urban Forestry* 40: 53–69. https://doi.org/10.48044/jauf.2014.007.

NIFC. 2024. *WFIGS Interagency Fire Perimeters*. National Interagency Fire Center. https://data-nifc.opendata.arcgis.com/datasets/5e72b1699bf74eefb3f3aff6f4ba5511_0/explore?location=0.000000%2C0.000000%2C1.41.

Nkemdirim, L. C. 1997. “On the Frequency and Sequencing of Chinook Events.” *Physical Geography* 18: 101–113. https://doi.org/10.1080/02723646.1997.10642610.

Pawlik, Ł. 2013. “The Role of Trees in the Geomorphic System of Forested Hillslopes—A Review.” *Earth Science Reviews* 126: 250–265. https://doi.org/10.1016/j.earscirev.2013.08.007.

Pawlik, Ł., P. Migoń, and M. Szymanowski. 2016. “Local- and Regional-Scale Biomorphodynamics due to Tree Uprooting in Semi-Natural and Managed Montane Forests of the Sudetes Mountains, Central Europe: Biomorphodynamics due to Tree Uprooting.” *Earth Surface Processes and Landforms* 41: 1250–1265. https://doi.org/10.1002/esp.3950.

Pepin, N. 2000. “Twentieth-Century Change in the Climate Record for the Front Range, Colorado, U.S.A.” *Arctic, Antarctic, and Alpine Research* 32: 135–146. https://doi.org/10.1080/15230430.2000.12003349.

Phillips, J. D., D. A. Marion, and A. V. Turkington. 2008. “Pedologic and Geomorphic Impacts of a Tornado Blowdown Event in a Mixed Pine-Hardwood Forest.” *Catena* 75: 278–287. https://doi.org/10.1016/j.catena.2008.07.004.

Phillips, J. D., P. Šamonil, Ł. Pawlik, J. Trochta, and P. Daněk. 2017. “Domination of Hillslope Denudation by Tree Uprooting in an Old-Growth Forest.” *Geomorphology* 276: 27–36. https://doi.org/10.1016/j.geomorph.2016.10.006.

Potapov, P. V., S. A. Turubanova, A. Tyukavina, et al. 2015. “Eastern Europe's Forest Cover Dynamics From 1985 to 2012 Quantified From the Full Landsat Archive.” *Remote Sensing of Environment* 159: 28–43. https://doi.org/10.1016/j.rse.2014.11.027.

Poulos, G. S., D. A. Wesley, J. S. Snook, and M. P. Meyers. 2002. “A Rocky Mountain Storm. Part I: The Blizzard—Kinematic Evolution and the Potential for High-Resolution Numerical Forecasting of Snowfall.” *Weather and Forecasting* 17: 955–970. https://doi.org/10.1175/1520-0434(2002)017<0955:ARMSPI>2.0.CO;2.

PRISM. 2024. “1991–2000 Climate Normals From PRISM Climate Group, Oregon State University.” https://prism.oregonstate.edu/.

QGIS Development Team. 2024. “QGIS Geographic Information System.” *Open Source Geospatial Foundation Project*. http://qgis.org.

Quine, C., and B. Gardiner. 2007. “Understanding How the Interaction of Wind and Trees Results in Windthrow, Stem Breakage, and Canopy Gap Formation.” In *Plant Disturbance Ecolology—The Process and the Response*, 103–155. Academic Press Cambridge.

R Core Team. 2024. *R: A Language and Environment for Statistical Computing*. R Foundation for Statistical Computing. https://www.r-project.org/.

Richner, H., and P. Hächler. 2013. “Understanding and Forecasting Alpine Foehn.” In *Mountain Weather Research and Forecasting: Recent Progress and Current Challenges*, edited by F. K. Chow, S. F. J. de Wekker, and B. J. Snyder, 219–260. Springer Netherlands. https://doi.org/10.1007/978-94-007-4098-3_4.

Roemer, H., G. Kaiser, H. Sterr, and R. Ludwig. 2010. “Using Remote Sensing to Assess Tsunami-Induced Impacts on Coastal Forest Ecosystems at the Andaman Sea Coast of Thailand.” *Natural Hazards and Earth System Sciences* 10: 729–745. https://doi.org/10.5194/nhess-10-729-2010.

Rother, M. T., and T. T. Veblen. 2016. “Limited Conifer Regeneration Following Wildfires in Dry Ponderosa Pine Forests of the Colorado Front Range.” *Ecosphere* 7: e01594. https://doi.org/10.1002/ecs2.1594.

Šamonil, P., L. Antolík, M. Svoboda, and D. Adam. 2009. “Dynamics of Windthrow Events in a Natural Fir-Beech Forest in the Carpathian Mountains.” *Forest Ecology and Management* 257: 1148–1156. https://doi.org/10.1016/j.foreco.2008.11.024.

Šamonil, P., P. Daněk, D. Adam, and J. D. Phillips. 2017. “Breakage or Uprooting: How Tree Dearth Type Affects Hillslope Processes in

Old-Growth Temperate Forests." *Geomorphology* 299: 74–76. https://doi.org/10.1016/j.geomorph.2017.09.023.

Šamonil, P., K. Král, and L. Hort. 2010. "The Role of Tree Uprooting in Soil Formation: A Critical Literature Review." *Geoderma* 157: 65–79. https://doi.org/10.1016/j.geoderma.2010.03.018.

Šamonil, P., R. J. Schaetzl, M. Valtera, et al. 2013. "Crossdating of Disturbances by Tree Uprooting: Can Treethrow Microtopography Persist for 6000 Years?" *Forest Ecology and Management* 307: 123–135. https://doi.org/10.1016/j.foreco.2013.06.045.

Santi, N. A., I. N. S. Jaya, M. B. Saleh, L. Syaufina, and B. Kuncahyo. 2022. "Detecting Burnt Severity and Vegetation Regrowth Classes Using a Change Vector Analysis Approach: A Case Study in the Southern Part of Sumatra, Indonesia." *International Journal of Wildland Fire* 31, no. 12: 1114–1128.

Schaetzl, R. J., S. F. Burns, T. W. Small, and D. L. Johnson. 1990. "Tree Uprooting: Review of Types and Patterns of Soil Disturbance." *Physical Geography* 11: 277–291. https://doi.org/10.1080/02723646.1990.10642407.

Schaetzl, R. J., D. L. Johnson, S. F. Burns, and T. W. Small. 1989. "Tree Uprooting: Review of Terminology, Process, and Environmental Implications." *Canadian Journal of Forest Research* 19: 1–11. https://doi.org/10.1139/x89-001.

Seidl, R., P. M. Fernandes, T. F. Fonseca, et al. 2011. "Modelling Natural Disturbances in Forest Ecosystems: A Review." *Ecological Modelling* 222: 903–924. https://doi.org/10.1016/j.ecolmodel.2010.09.040.

Senf, C., and R. Seidl. 2021. "Mapping the Forest Disturbance Regimes of Europe." *Nature Sustainability* 4: 63–70. https://doi.org/10.1038/s41893-020-00609-y.

Sheppard, P. R., A. C. Comrie, G. D. Packin, K. Angersbach, and M. K. Hughes. 2002. "The Climate of the US Southwest." *Climate Research* 21: 219–238. https://doi.org/10.3354/cr021219.

Simon, A., Á. Horváth, and J. Vivoda. 2015. "Case Study and Numerical Simulations of the November 19, 2004 Severe Windstorm in Central Europe." *Időjárás—Quarterly Journal of the Hungarian Meteorological Service* 110: 91–123.

Singh, S., and R. Talwar. 2014. "A Comparative Study on Change Vector Analysis Based Change Detection Techniques." *Sadhana* 39: 1311–1331. https://doi.org/10.1007/s12046-014-0286-x.

Solano Correa, Y. T., F. Bovolo, and L. Bruzzone. 2014. "Change Detection in Very High Resolution Multisensor Optical Images." *In Proceedings Image and Signal Processing for Remote Sensing XX; 924410*, Vol 9244. https://doi.org/10.1117/12.2068171.

Solano-Correa, Y. T., F. Bovolo, and L. Bruzzone. 2019. "An Approach to Multiple Change Detection in VHR Optical Images Based on Iterative Clustering and Adaptive Thresholding." *IEEE Geoscience and Remote Sensing Letters* 16: 1334–1338. https://doi.org/10.1109/LGRS.2019.2896385.

Sommerfeld, A., C. Senf, B. Buma, et al. 2018. "Patterns and Drivers of Recent Disturbances Across the Temperate Forest Biome." *Nature Communications* 9, no. 1: 4355. https://doi.org/10.1038/s41467-018-06788-9.

Strzyżowski, D., J. Fidelus-Orzechowska, and M. Żelazny. 2018. "Sediment Transport by Uprooting in the Forested Part of the Tatra Mountains, Southern Poland." *Catena* 160: 329–338. https://doi.org/10.1016/j.catena.2017.09.019.

Sturtevant, B. R., and M.-J. Fortin. 2021. "Understanding and Modeling Forest Disturbance Interactions at the Landscape Level." *Frontiers in Ecology and Evolution* 9: 653647. https://doi.org/10.3389/fevo.2021.653647.

Sun, W.-Y. 2013. "Numerical Study of Severe Downslope Windstorm." *Weather and Climate Extremes* 2: 22–30. https://doi.org/10.1016/j.wace.2013.10.002.

Tanase, M. A., C. Aponte, S. Mermoz, A. Bouvet, T. Le Toan, and M. Heurich. 2018. "Detection of Windthrows and Insect Outbreaks by L-Band SAR: A Case Study in the Bavarian Forest National Park." *Remote Sensing of Environment* 209: 700–711. https://doi.org/10.1016/j.rse.2018.03.009.

Thom, D., R. Seidl, G. Steyrer, H. Krehan, and H. Formayer. 2013. "Slow and Fast Drivers of the Natural Disturbance Regime in Central European Forest Ecosystems." *Forest Ecology and Management* 307: 293–302. https://doi.org/10.1016/j.foreco.2013.07.017.

Tishmack, J., S. A. Mata, and J. M. Schmid. 2005. *Mountain Pine Beetle Emergence From Lodgepole Pine at Different Elevations Near Fraser, CO (No. RMRS-RN-27)*. U.S. Department of Agriculture, Forest Service, Rocky Mountain Research Station. https://doi.org/10.2737/RMRS-RN-27.

Tran, B. N., M. A. Tanase, L. T. Bennett, and C. Aponte. 2020. "High-Severity Wildfires in Temperate Australian Forests Have Increased in Extent and Aggregation in Recent Decades." *PLoS One* 15: e0242484. https://doi.org/10.1371/journal.pone.0242484.

U.S. Department of Agriculture. 2024. "National Agriculture Imagery Program (NAIP) Orthoimagery." *Distributed by USGS*. https://www.usgs.gov/centers/eros/science/usgs-eros-archive-aerial-photography-national-agriculture-imagery-program-naip.

Ulanova, N. G. 2000. "The Effects of Windthrow on Forests at Different Spatial Scales: A Review." *Forest Ecology and Management* 135: 155–167.

University of Maryland. 2022. "Global Forest Change (GFC) Data." https://storage.googleapis.com/earthenginepartners-hansen/GFC-2022-v1.10/download.html.

Urquiza-Haas, T., P. M. Dolman, and C. A. Peres. 2007. "Regional Scale Variation in Forest Structure and Biomass in the Yucatan Peninsula, Mexico: Effects of Forest Disturbance." *Forest Ecology and Management* 247: 80–90. https://doi.org/10.1016/j.foreco.2007.04.015.

USGS. 2024. "3DEP LidarExplorer." https://apps.nationalmap.gov/lidar-explorer/#/.

Veblen, T. T. 2000. "Disturbance Patterns in Southern Rocky Mountain Forests." In *Forest Fragmentation in the Southern Rocky Mountains*, edited by R. L. Knight, 31–54. Colorado University Press.

Veblen, T. T., K. S. Hadley, and L. M. Reid. 1991. "Disturbance and Stand Development of a Colorado Subalpine Forest." *Journal of Biogeography* 18: 707–716.

Veblen, T. T., K. S. Hadley, L. M. Reid, and A. J. Rebertus. 1989. "Blowdown and Stand Development in a Colorado Subalpine Forest." *Canadian Journal of Forest Research* 19: 1218–1225.

Velasco Hererra, V. M., W. Soon, C. Pérez-Moreno, et al. 2022. "Past and Future of Wildfires in Northern Hemisphere's Boreal Forests." *Forest Ecology and Management* 504: 119859. https://doi.org/10.1016/j.foreco.2021.119859.

Verde, N., and M. Tsakiri-Strati. 2014. "Change Detection and Fire Risk Assessment Model Using Landsat Imagery for the Forest of Gerania Mountains." *South-Eastern European Journal of Earth Observation and Geomatics* 3: 75–82.

Vorovencii, I. 2014. "Detection of Environmental Changes due to Windthrows Using Landsat 7 ETM+ Satellite Images." *Environmental Engineering and Management Journal* 13: 565–576. https://doi.org/10.30638/eemj.2014.060.

Vorster, A. G., P. H. Evangelista, T. J. Stohlgren, et al. 2017. "Severity of a Mountain Pine Beetle Outbreak Across a Range of Stand Conditions in Fraser Experimental Forest, Colorado, United States." *Forest Ecology and Management* 389: 116–126. https://doi.org/10.1016/j.foreco.2016.12.021.

Wang, F., and Y. J. Xu. 2010. "Comparison of Remote Sensing Change Detection Techniques for Assessing Hurricane Damage to Forests." *Environmental Monitoring and Assessment* 162: 311–326. https://doi.org/10.1007/s10661-009-0798-8.

Winter Park. 2024. “Weather Data From Automatic Meteorological Station Lunch Rock.”

Wohl, E. 2013. “Redistribution of Forest Carbon Caused by Patch Blowdowns in Subalpine Forests of the Southern Rocky Mountains, USA.” *Global Biogeochemical Cycles* 27: 1205–1213. https://doi.org/10.1002/2013GB004633.

Wohl, E. 2022. “Logjam Fluctuations During the Decade After a Major Blowdown Along a Mountain Stream in the US Southern Rockies.” *Earth Surface Processes and Landforms* 47: 699–705. https://doi.org/10.1002/esp.5330.

Ye, S., J. Rogan, Z. Zhu, et al. 2021. “Detecting Subtle Change From Dense Landsat Time Series: Case Studies of Mountain Pine Beetle and Spruce Beetle Disturbance.” *Remote Sensing of Environment* 263: 112560. https://doi.org/10.1016/j.rse.2021.112560.

Zanetti, M., F. Bovolo, and L. Bruzzone. 2015. “Rayleigh-Rice Mixture Parameter Estimation via EM Algorithm for Change Detection in Multispectral Images.” *IEEE Transactions on Image Processing* 24: 5004–5016. https://doi.org/10.1109/TIP.2015.2474710.

Zielonka, T., J. Holeksa, P. Fleischer, and P. Kapusta. 2010. “A Tree-Ring Reconstruction of Wind Disturbances in a Forest of the Slovakian Tatra Mountains, Western Carpathians.” *Journal of Vegetation Science* 21: 31–42. https://doi.org/10.1111/j.1654-1103.2009.01121.x.

Supporting Information

Additional supporting information can be found online in the Supporting Information section.

International Journal of Applied Earth Observation and Geoinformation 131 (2024) 103992

Contents lists available at ScienceDirect

International Journal of Applied Earth Observation and Geoinformation

journal homepage: www.elsevier.com/locate/jag

Root plates of uprooted trees – Automatic detection and biotransport estimation using LiDAR data and field mapping

Janusz Godziek [a,b]

[a] University of Silesia, Faculty of Natural Sciences, Institute of Earth Sciences, ul. Będzińska 60, 41-200 Sosnowiec, Poland
[b] University of Silesia, International Environmental Doctoral School, ul. Będzińska 60, 41-200 Sosnowiec, Poland

ARTICLE INFO

Keywords:
Root plate detection
Root plate volume estimation
Sediment transport
Automation using R
Windthrow

ABSTRACT

The availability of LiDAR data (including open-source data), combined with specialized algorithms, allows the use of these data to automatically detect landforms, vegetation and other objects. LiDAR point clouds have been frequently applied for the detection and evaluation of living trees but never for root plates of uprooted trees. However, tree uprooting is one of the most important biotic-abiotic interactions in temperate forests. This process leads to the formation of root plates, i.e., microrelief forms consisting of undecomposed tree root systems and the attached soil and rock particles. Root plates are involved in biotransport, i.e., the movement of soil and rock material by living organisms. The objective of this study was to develop an automatic method for root plate detection and volume (and thus biotransport) estimation based on LiDAR data. The study area included three Norway spruce-dominated plots located in two national parks in the Polish Carpathians. For validation, the author mapped the root plates using a GNSS receiver and measured their dimensions. We created the differential model presenting the height of root plates, fallen trunks, and dense understory vegetation by interpolating the last returns with a normalized height < 2 m. We automatically extracted the root plate locations and computed their volume using three ways of estimation. The method was built in R. Depending on the study plot, the root plate detection rates ranged from 70.3 % to 79.1 %. For different ways of estimation, the mean root plate volume varied in a range of 2.2–3.35 m^3, while the mean biotransport reached 176.1–268.3 m^3/ha. The method offers the best results for LiDAR data with a minimal density of 8 pts/m^2. We recommend using this method for 1) protected Norway spruce stands and 2) windthrows with no or few young conifers. The method can be applied to 1) assess the amount and spatial distribution of root plates and 2) determine the degree of soil disturbance and transport of soil material. Applying point cloud data to investigate the effects of tree uprooting can improve the understanding of the scale and course of different environmental processes related to this phenomenon. In future studies, field root plate measurements and volume estimations could be independently confirmed by using LiDAR data and the method presented in this study.

1. Introduction

Tree uprooting (treethrow) can be considered one of the most important biotic-abiotic interactions in temperate forests worldwide (Schaetzl et al., 1989; Šamonil et al., 2010a; Phillips et al., 2017). This process is primarily driven by episodes of hurricane-force winds, which cause forest damage (Everham and Brokaw, 1996; Taylor et al., 2019). Tree susceptibility to wind damage is controlled by features of tree stands (e.g., age, height, health and dominant species) and by abiotic factors (e.g., soil, topography) (Schaetzl et al., 1989; Constantine et al., 2012; Phillips et al., 2017; Strzyżowski, 2019). When a tree is toppled (uprooted) by wind, some of the soil material attached to its root system is lifted and deposited on the ground surface in the form of a root plate. This process causes geomorphic and pedogenic effects that should not be omitted (Schaetzl et al., 1990; Šamonil et al., 2010a; Pawlik, 2013). Root plates are microrelief forms that consist of undecomposed tree root systems and soil and rock particles attached to roots (Fig. 2) (Schaetzl et al., 1989; Pawlik, 2013; Šamonil et al., 2016; Strzyżowski et al., 2018). Root plates arise as a direct result of the tree uprooting process. Therefore, these forms indicate the impact of winds on forest dynamics (Kulakowski and Veblen, 2002; Doane et al., 2021). Another type of tree mortality, tree breakage, is not associated with such distinct above-ground evidence and does not result in significant or long-term geomorphic or pedogenic consequences (Mitchell, 2013). The shape, volume and spatial orientation of root plates are influenced by many factors, such as the anatomy of the root system of a given tree species, the soil type and bedrock, the soil water content, and the prevailing wind direction (Schaetzl et al., 1989; Pawlik, 2013) In addition, root plates can be considered to be involved in biotransport, i.e., the movement of soil and rock material by living organisms (Phillips et al., 2008;

https://doi.org/10.1016/j.jag.2024.103992
Received 12 February 2024; Received in revised form 17 May 2024; Accepted 19 June 2024
Available online 25 June 2024

Pawlik, 2013). From a broader perspective, in temperate forests, root plates are one of the main effects of biomorphodynamics, i.e., changes in landforms and the intensity of geomorphological processes caused by biota (Šamonil et al., 2015). Root plates influence the development of understory vegetation (Kooch et al., 2012), and biodiversity and the process of forest recovery after windthrow (Everham and Brokaw, 1996; Buma, 2015). Root plate preservation is strongly related to forest management activities. In managed forests, root plates are normally removed, but in old-growth forests, they are left intact and represent natural remnants of past forest damage (Šamonil et al., 2010b; Barker Plotkin et al., 2017). Gradual decomposition of roots and erosion of the soil attached to them leads to the formation of pit-mound topography, which can act as an indicator of past forest dynamics (Ulanova, 2000; Šamonil et al., 2016; Godziek and Pawlik, 2023). For this reason, the detection, documentation, and mapping of root plates are highly important.

Wind-driven forest damage is prevalent in some of the world's forests (Mitchell, 2013; Bonannella et al., 2024). Satellite imagery and orthophotomaps are crucial remote sensing (RS) data for evaluating negative and positive changes in forest ecosystems, including wind-driven damage (Hansen et al., 2013; Potapov et al., 2015).Besides, the LiDAR data is crucial for research on forest disturbances (Dubayah et al., 2020; Heinaro et al., 2021). The availability of LiDAR point cloud data has been growing exponentially in recent decades (including open-source data). LiDAR data provide an opportunity to quantify and measure various landforms and changes in vegetation cover, even in remote areas where access is difficult. Using the LiDAR data in the investigations may help to increase the scope of the work and significantly reduce the cost of fieldwork. The LiDAR data can be effectively acquired using drones or airplanes (altitude laser scanning, ALS) and ground scanners (terrestrial laser scanning, TLS). The computing power required to process the point clouds is provided by constantly developing hardware and software. Hence we presume the opportunities to use the LiDAR for different applications will continue to increase. The availability of data and dedicated algorithms provides adequate opportunities to develop automatic and objective methods for detecting, interpreting, and mapping relief and land cover forms (Jasiewicz and Stepinski, 2013). Hence, LiDAR point clouds have been frequently applied to extract the location of the stems of fallen trees (coarse woody debris, CWD) (Blanchard et al., 2011; Mücke et al., 2012; Lindberg et al., 2013; Nyström et al., 2014; Joyce

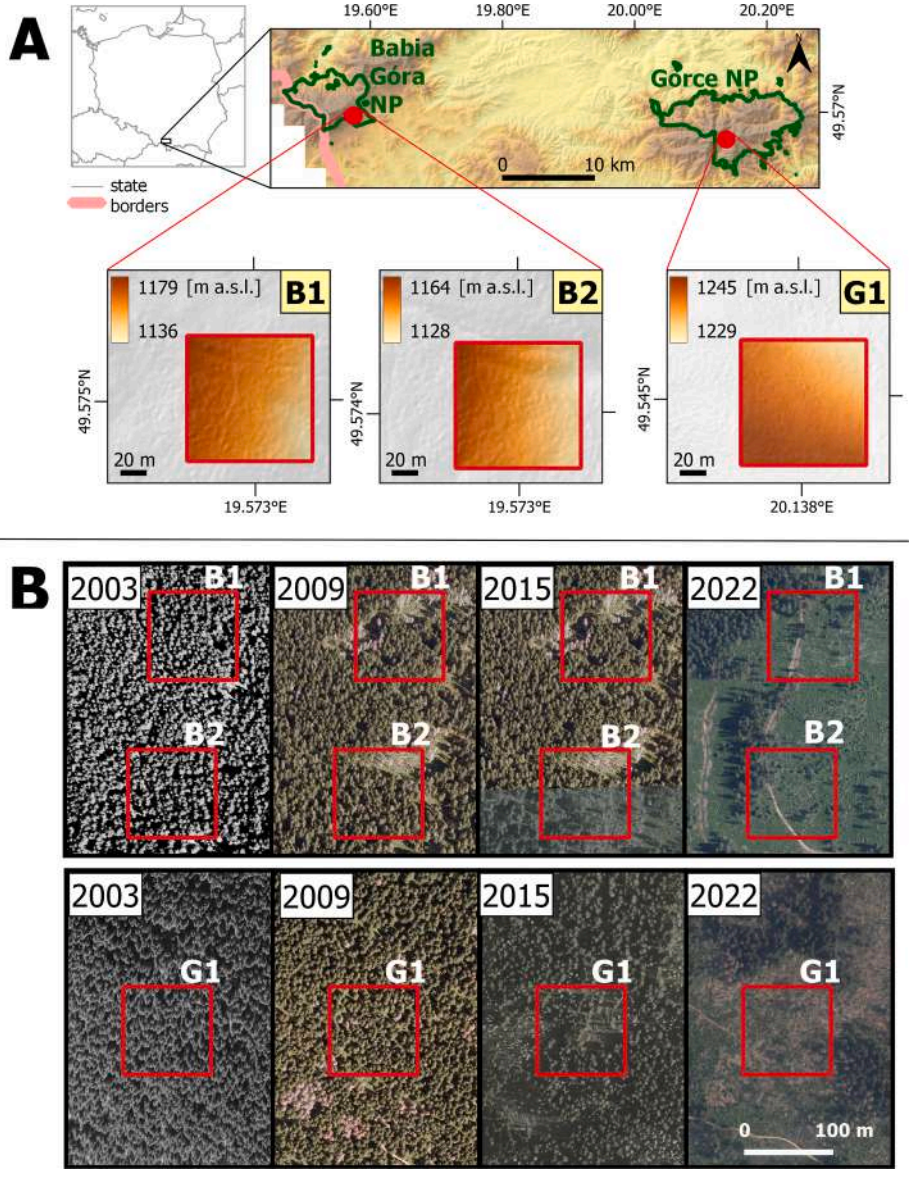

Fig. 1. A – Location and topography of the study plots. B – Forest dynamics of the study plots based on orthophotomaps obtained from the Polish Head Office of Geodesy and Cartography (download from https://www.geoportal.gov.pl/).

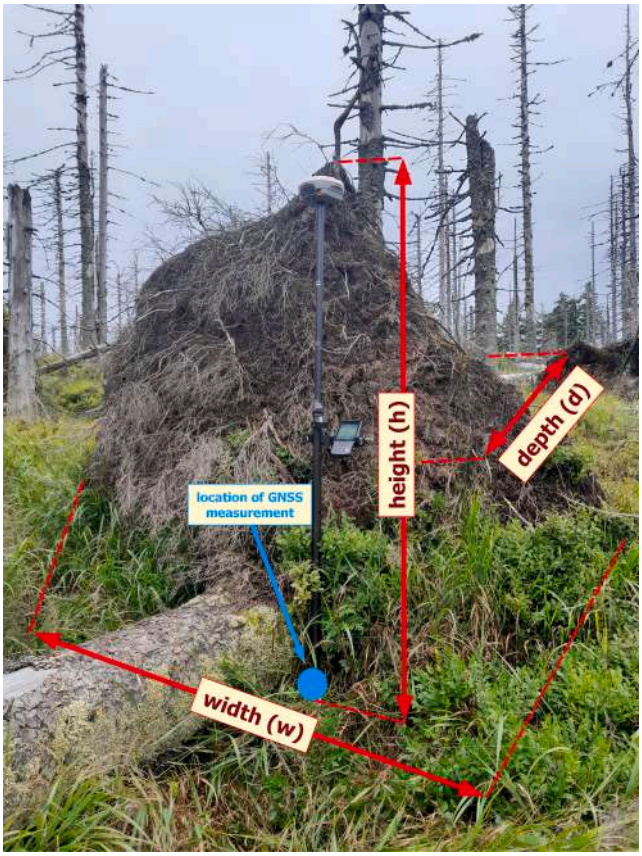

Fig. 2. Root plate field measurement procedure. We measured the location using a GNSS receiver (accuracy: +/- 0.05 m) and three root plate dimensions (width, height, depth) as described in detail in the text. Photo. J. Godziek (2023).

et al., 2019; Heinaro et al., 2021; Dakin Kuiper et al., 2023). To the best of our knowledge, the LiDAR data have not yet been used to detect the root plates of uprooted trees. However, we can presume that if the point cloud is used to detect the downed trees, then such data will also allow the extraction of root plate locations. As the LiDAR data provide a very accurate representation of the Earth's surface, we also assume that such data will enable us to estimate the root plate volume (and thus the biotransport). Following this, the LiDAR point cloud may be applied to 1) detect root plates and 2) estimate their volume.

Previous studies on root plates, pit mound topography and windthrows have been mostly based on field measurements (Gallaway et al., 2009; Pawlik et al., 2013; Šamonil et al., 2016) and have been focused on 1) the impacts on the soil formation and properties (Kooch et al., 2014; Šamonil et al., 2015, 2016), 2) the relationship between the root system architecture and the shape of the root plate (Beatty and Stone, 1986), 3) the rate of root plate erosion and decomposition (Šamonil et al., 2010b), and 4) the link between a particular episode of extreme wind and the formation of root plates (Kulakowski and Veblen, 2002; Strzyżowski et al., 2016; Zadrożny et al., 2017). Using field data, several characteristics related to root plates were estimated, e.g., the volume of the root plates, the area occupied by the root plates, the mean upslope and downslope transport distances and the mean sediment flux (Kotarba, 1970; Reid, 1981 Norman et al., 1995; Gabet et al., 2003; Phillips et al., 2008; Dąbrowska, 2009; Gallaway et al., 2009; Richards et al., 2011; Rojan, 2012; Strzyżowski et al., 2018). In the majority of approaches, the three dimensions of the root plates (width, height, and depth) were measured (Dąbrowska, 2009; Strzyżowski et al., 2018), and the volume was estimated using the modified equation for a half ellipsoid (for details see Eq. (4)). The determining of the location of the root plates with the use of GPS positioning (Pawlik et al., 2013) was quite uncommon, perhaps due to the difficulties in using precise mapping equipment in remote forest areas where windthrow occurred. Several studies have applied RS data and modeling to investigate the effects of tree uprooting and biotransport. LiDAR-derived DTM was used to quantify hillslope sediment fluxes driven by treethrow in south-central Indiana, United States (Doane et al., 2021). The study focused on topographic roughness related mainly to the occurrence of pit mound topography and estimated the topographic variance resulting from tree uprooting for entire slopes. A simulation approach based on the forest gap model (ForGEM) was applied to investigate the relationship between windthrow-driven sediment transport and windstorm frequency (Constantine et al., 2012). Neither approach using RS data extracted the location or estimated the volume of a single root plate. Thus, the development of a root plate detection and volume estimation method based on LiDAR data is crucial for scientific disciplines such as geomorphology, soil science, and forest ecology. With LiDAR point clouds, the effects of the tree uprooting could be studied on a broader spatial and temporal scale than in field research. This would allow us to enhance our understanding of the impact of the treethrow process on slope evolution. Also changes within windthrow patches could be monitored remotely, especially in strictly protected areas, reducing the cost and time required for fieldwork. The objective of this study was to develop an automatic unsupervised method of 1) root plate detection and 2) root plate volume estimation (and thus biotransport estimation) based on LiDAR point cloud data. The author 1) presents the details and steps of the proposed method, 2) describes how the field data were acquired and applied to validate the method, 3) analyzes the detection results in detail, 4) explains the inaccuracies of the method, and 5) proposes potential applications of the method.

2. Materials and methods

2.1. Study area

We selected three one hectare (100 × 100 m) study plots located in the Polish Outer Western Carpathians. Two of them were in Babia Góra National Park (B1 and B2), and one was in Gorce National Park (G1) (Fig. 1A). They were located at 1200–1300 m above sea level (m a.s.l). and were gently sloped. The study plot exposures and geomorphic positions were the eastern hillslope (Mt. Babia Góra), flat ridge and northeastern hillslope (Gorce Mts.). (Fig. 1A). At the altitude of the study plots, the mean annual temperature is approximately 2–4 °C, and the mean annual precipitation can reach 1400 mm (Obrębska-Starkel et al., 2004). At the Turbacz station (1272 m a.s.l., Gorce Mts, 1.3 km west of plot G1), during the period from 2010 to 2020, the mean annual temperature reached 4.6 °C, the minimal recorded temperature was −26.6 °C, and the maximal recorded temperature was 28.7 °C. The annual sum of precipitation reached approximately 900–1000 mm for most years during the 2010–2020 period. During the same period, NW winds significantly prevailed. Other dominant wind directions included W and SE. The highest recorded wind speed reached 22.9 m/s (own calculation based on IMWM-NRI archival data, 2023).

All the study plots were overgrown by single-species forests composed of Norway spruce (*Picea abies* (L.) H. Karst.). For the plots located in Babia Góra National Park (B1, B2), initial wind-driven forest damage occurred in November 2004, during the bora-type wind blowing from the north. In 2005, the authorities of Babia Góra National Park decided to establish a strictly protected monitoring area covering the initial windthrow site. In subsequent years, the area of wind-damaged forest gradually increased (Zadrożny et al., 2017) (Fig. 1B). Plot G1, located in Gorce National Park, experienced initial damage between 2009 and 2015. In subsequent years, the extent of the damaged forest expanded (Fig. 1B). The B1 and B2 plots were subjected to spontaneous forest regeneration after damage. For study plot G1, the period after the initial forest damage was shorter, and thus, the plot was only slightly

overgrown.

2.2. Materials

2.2.1. LiDAR data

Analysis was based on two altitude laser scanning LiDAR point clouds obtained from the following sources: 1) Babia Góra National Park and 2) Gorce National Park. We obtained point clouds from scientific repositories of both national parks upon formal request. Data from Babia Góra were acquired during the leaf-off season in 2020. The density of the point cloud is 70 points/m^2 with 42.7 pulses/m^2. For the study plots located in Babia Góra (B1, B2), we worked on one tile of LiDAR data with the grid sheet identifier provided by the Polish Head Office of Geodesy and Cartography M-34–88-A-c-2–1-1–4 (grid for the coordinate reference system ETRF2000-PL/CS92, scale 1:1250). This tile covered a rectangle with sides of 560 × 580 m, had an area of 33 ha, and took up 1.5 GB of disc space. A point cloud from Gorce National Park was obtained in May 2021. The density of these data reaches 193 points/m^2, with 141.5 pulses/m^2.

For the G1 plot, one tile was analyzed (M-34–89-A-d-1–3-3, coordinate reference system ETRF2000-PL/CS92, scale 1:2500). The tile occupied a rectangle with sides of 1130 × 1160 m, had an area of 131 ha and took up 17 GB of disc space. Both source point clouds were 1) clipped to the 20-m buffers of particular study plots and 2) processed and classified (for details, see Section 2.3.1). We compared the basic properties of the point clouds located within the boundary of each study

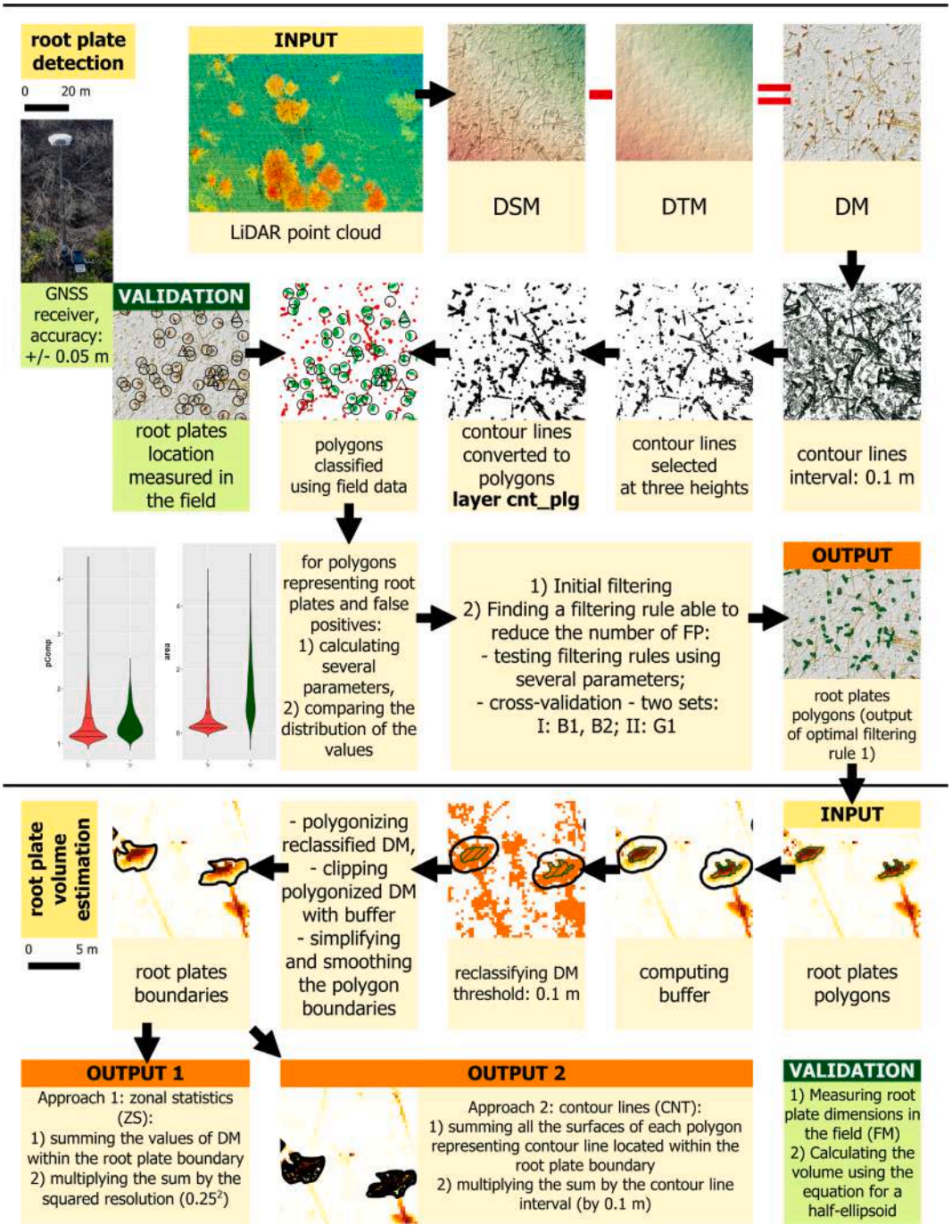

Fig. 3. Workflow of the proposed method.

plot (Table 1). For plots B1 and B2, the point cloud density was 56.7 points/m^2 and 51.5 points/m^2, respectively, while for plot G1, it was 132.6 points/m^2.

2.2.2. Field measurements

The aim of the field measurements was to acquire validation datasets to assess the accuracy and validity of the proposed method. The fieldwork was performed 1) before modeling to obtain the validation datasets on the location and volume of root plates and 2) after modeling to investigate in depth the obtained results. The study plots (B1, B2, G1) were the sites of fieldwork. Before modeling, we accurately mapped the positions of the root plates and measured their dimensions. Locations were obtained using a GNSS receiver with horizontal and vertical accuracies reaching +/- 0.05 m. We measured the location of the root plate by placing the GNSS stick on the ground on one of the sides of the fallen tree trunk, as close to the root plate as possible (Fig. 2). In isolated cases of very dense vegetation, measurements were taken as close to the root plate as possible. We measured the height (**h**), width (**w**) and depth (**d**) of the root plate with an accuracy of +/- 0.05 m using a measuring tape. The height was measured from the place on the ground where the GNSS stick was located up to the highest part of the root plate with soil or rock particles. We measured the width as the distance between the outermost points and the soil attached to the roots on both sides of the root plate. The depth was measured from the junction of the root neck with the soil to the bottom part of the soil on the other side of the root plate. We also took photos of the selected root plates. We divided the root plates into two categories:

1. Category 1 – fresh root plates, clearly visible;
2. Category 2 – root plates overgrown by vegetation and/or partly eroded (Fig. 6).

After modeling, we investigated the obtained outcome by checking the location of some of the false positives (see Section 2.3.1). We located the places for field checking by analyzing the modeling results (differential model (DM), Section 2.3.1) via GIS software. We imported locations to the GNSS receiver, found them in the field and documented them by taking photos (Fig. 6). We also identified the primary tree and shrub species growing in the study plots.

2.3. Methods

2.3.1. Root plate detection

During the analyses of LiDAR data from different sources, we observed that the standard LiDAR data classification procedure misclassifies such nonstandard forms as root plates. Therefore, there appeared to be a need to develop an approach for extracting information about root plates from the processed point cloud, which is relevant for various applications. In the standard point cloud classification procedure, laser beam reflections from root plates were classified as low or medium vegetation, as the height of the root plates is similar to the height of the understory vegetation (e.g., small shrubs and young trees). The ground point classification algorithms did not label the laser beam reflections from the root plates as ground points. The reason might be the shape of the root plates, as they are relatively small, and their sides are very steep. Field observation showed that in most cases, root plates are not taller than 2 m. For this reason, we can assume that most laser beam reflections from root plates are located up to 2 m above the ground. Moreover, the laser beam is unable to penetrate through the root plate or fallen trunk. Thus, the majority of points reflected from the root plates or fallen trunks were the last returns of the laser beam. In regard to the above-described observations, we propose a method of root plate detection using points 1) situated up to 2 m above the ground and 2) representing the last returns of the laser beam. All the computations were performed and automated in the R programming language (R Core Team, 2023) using RStudio (RStudio Team, 2021). The most important packages that were used include *lidR* (Roussel et al., 2020), *terra* (Hijmans, 2023), *sf* (Pebesma, 2018), *stars* (Pebesma, 2022), *dplyr* (Wickham et al., 2023), and *ggstatsplot (*Patil, 2021*)*. All raster layers were computed at a 0.25 m spatial resolution.

We 1) processed the raw point cloud data, 2) assigned point class numbers based on the American Society for Photogrammetry and Remote Sensing specification (ASPRS, 2011), and 3) classified and removed noise points (i.e., “high points” and “low points”) using the statistical outlier removal (SOR) algorithm. For every point, this algorithm calculates the mean distance to its k-nearest neighboring points. Points farther than the average distance plus a multiplier of the standard deviation are classified as noise and removed. The ground points were classified using a progressive morphological filter (Zhang et al., 2003). We assigned points to vegetation classes using the following threshold values: low vegetation (0–0.4 m above the ground), medium vegetation (0.4–2 m above the ground) and high vegetation (>2 m above the ground). Then, we 1) produced elevation models at a 0.25 m spatial resolution using TIN interpolation, 2) computed the Digital Terrain Model (DTM) using only ground points, 3) created the Digital Surface Model (DSM) representing the root plates, fallen trunks and dense understory vegetation by interpolating the points representing the last returns of the laser beam and located up to 2 m above the ground (point classes: ground, low vegetation, medium vegetation), and 4) produced the differential model (DM) by subtracting the DTM from the DSM- to increase the visibility of the root plates (Fig. 3). This subtraction allowed us to obtain a model of the height of certain features of the forest floor caught by DSM (including root plates). Using such a workflow resulted in eliminating the influence of topography on root plate detection. The created model (DM) had values from 0 to 2 m, as only the laser beam reflections up to 2 m above the ground were taken into consideration during DSM computation.

To extract the locations of the root plates, for DM and DSM we computed the contour lines at 0.1-m intervals. We observed that contour lines closed within root plates, which are significant convex surface objects. The comparison of contour lines between DM and DSM indicated that DM-derived contour lines better reflect root plates than DSM-derived contour lines. Thus we decided to use a differential model (DM) to detect root plates. Regarding the height and shape of the root plates, we decided to extract contour lines located at three height levels: 0.5, 1 and 1.5 m. We converted closed contours to polygons (layer **cnt_plg**, Fig. 3). Then, we divided the polygons into root plates (RPs) and false positives (FPs) using collected validation data (see Section 2.2.2). We deleted small false positives by removing polygons with an area (AR) < 0.1 m^2. Then, to reduce the number of false positives and create an optimal filtering rule for the detection method, we aimed to find differences between the root plate polygons and false positive polygons. Therefore, we calculated several parameters for each polygon (see Table 1S). For each parameter, we produced value distribution plots divided into root plates and false positives. We performed initial filtering 1) by removing polygons with areas > 5 m^2, as the area of the largest “root plate” polygon was less than 5 m^2, and 2) by deleting false positives representing concave objects (e.g., space between fallen trunks) with a mean DM < 0.5 m. We analyzed the remaining polygons to determine the most effective filtering rule under which the number of false positives would significantly decrease. We tested 1454 filtering rules using the following parameters: area, polygon compactness index (PC) (Brinkhoff et al., 1995), the maximum value of the vegetation

Table 1
Comparison of basic point cloud data properties for each study plot.

No.	study plot	number of points [thousands]	density [pts/m^2]	density [pulses/m^2]	size [MB]
1.	B1	578.2	56.7	38.3	39.7
2.	B2	525.2	51.5	35.8	36.1
3.	G1	1350	132.6	113.5	87.7

height model (VHM_max), and convex hull perimeter (CVHP) (Supplementary Materials, Table 2S). The polygon compactness index was calculated as follows:

$$PC = \frac{P}{3.45 \bullet \sqrt{AR}} \quad (1)$$

where:

PC – polygon compactness index.

P – polygon perimeter.

AR – polygon area.

Such an approach allowed us to relate the area of the given polygon to the length of its boundary. The more complex was the polygon boundary, the higher were the values of PC. The vegetation height model (VHM) was computed by subtracting the DSM representing the tree canopies (interpolated using first returns of the laser beam) from the DTM. Convex hull polygons were delineated as the smallest convex polygons enclosing the vertices of individual polygons. For the testing procedure, the data were divided into training and test sets in the

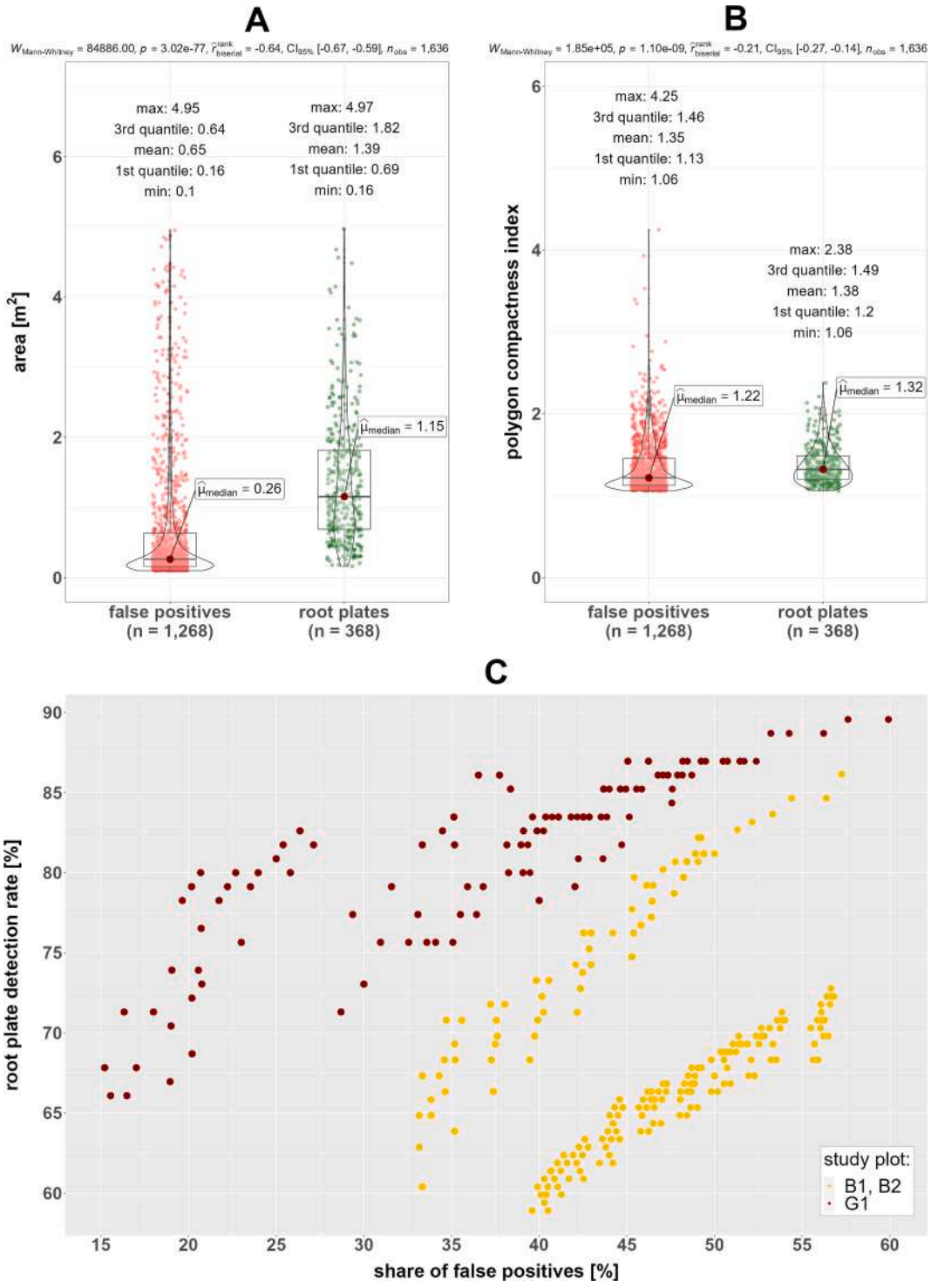

Fig. 4. A, B – Plots of the distribution of the *area* and *polygon compactness index* generated for polygons after initial filtering and divided into root plates and false positives. C – Relationships between the root plate detection rate and share of false positives for 1454 polygon filtering rules tested on two datasets (B1&B2, G1).

following manner: turn I: B1 and B2, the training set; G1, the test set; and turn II: G1, the training set; B1 and B2, the test set. For the results of each of the 1454 tested filtering rules, we 1) merged the overlapping polygons (related to the use of three contour line levels) and 2) calculated the root plate detection rate:

$$\boldsymbol{RPdr} = \frac{\boldsymbol{RPd}}{\boldsymbol{RPm}} \bullet 100\% \quad (2)$$

where:

RPdr – root plate detection rate.
RPd –number of detected root plates (true positives, TP).
RPm –number of root plates measured in the field (validation data).
and the share of false positives:

$$\boldsymbol{FPsh} = \frac{\boldsymbol{FP}}{\boldsymbol{Ad}} \bullet 100\% \quad (3)$$

where:

FPsh – share of false positives.
FP –number of false positives.
Ad –number of all detected polygons.

We compared these two ratios on the scatter plot to determine the optimal filtering rules (those with a high root plate detection rate and a low share of false positives) (Fig. 4C). We tested different groups of queries (Table 2S), which resulted in the grouping of the filtering rules on the scatter plot. The tested polygon filtering rules achieved better results for the G1 plot than for the B1&B2 plots. Based on the scatter plot, we selected several filtering rules for further analysis. In turn I (training: plots B1&B2), we selected rules with FPsh $<$ 35 % and RPdr $>$ 65 %, while in turn II (training: plot G1), rules with FPsh $<$ 25 % and RPdr $>$ 75 % were selected. We compared the results obtained in both turns, which allowed us to propose few filtering rules (Table 2). Then, we applied optimal filtering rule 1 (Table 2, no. 3) to extract the locations of the root plates in all the study plots (Fig. 5). To further investigate optimal filtering rule 1, we tested the significance of differences in the parameters used in this rule, i.e., area and polygon compactness index (Fig. 4A, 4B). Due to 1) the different number of observations in the compared groups and 2) lack of a normal distribution, we applied the Mann-Whitney *U* test (Mann and Whitney, 1947). To evaluate the impact of the point cloud density on the detection results, we applied the optimal root plate detection algorithm (using optimal filtering rule 1) to the point clouds at the different densities (Fig. 7).

2.3.2. Biotransport estimation

To estimate the extent of biotransport driven by tree uprooting, we needed to calculate the volume of each root plate and therefore delineate the root plate boundary. To calculate the biotransport as accurately as possible, we selected all polygons from the **cnt_plg** layer (Section 2.3.1) corresponding to the root plates mapped in the field. We merged the overlapping polygons so that one polygon corresponded to one root plate. For each polygon, we created a 1-m buffer, as the spatial analysis showed that in all cases, such a distance covered all the root plates and was not too wide. Then, we extracted areas with DM values greater than or equal to 0.1 m above the ground within the buffers and 2) simplified and smoothed the shape to eliminate the influence of pixel boundaries. In most cases, the root plate boundaries delineated in this way corresponded well with the real shape of the root plates (see Fig. 3).

The root plate volume was calculated with the use of 1) field measurements and 2) a differential model (DM). Applying the field data, we estimated the volume of the root plates using an approximation to the shape of a half ellipsoid (Norman et al., 1995). This approach assumes that the root plate dimensions (width, height, and depth) are related to the three semi-axes of the half ellipsoid (a, b, c). To represent the length of the semi-axes, the **w** and h dimensions must be divided by 2. Then, the root plate volume estimation formula can be derived from the equation for the volume of a half ellipsoid in the following way:

$$\boldsymbol{V} = \frac{1}{2} \bullet \left(\frac{4}{3}\boldsymbol{\pi abc}\right)$$

$$\boldsymbol{V} = \frac{1}{2} \bullet \left(\frac{4}{3}\boldsymbol{\pi} \bullet \frac{\boldsymbol{w}}{2} \bullet \frac{\boldsymbol{h}}{2} \bullet \boldsymbol{d}\right)$$

$$\boldsymbol{V} = \frac{\boldsymbol{\pi whd}}{6} \quad (4)$$

where:

a, b, c – semi-axes of the ellipsoid.
w – width [m] of a root plate.
h – height [m] of a root plate.
d – depth [m] of a root plate.

To calculate the volume with the use of DMs, we applied two approaches—the contour lines (CNT) approach and the zonal statistics (ZS) approach (Fig. 3). The CNT approach was based on 0.1-m interval contour lines. We converted contour lines to polygons and clipped the polygons to the root plate boundaries. We calculated the area of each clipped polygon. For each root plate boundary, we summed the areas of the clipped polygons. To compute the final result, we multiplied the summed areas by the contour line interval (i.e., by 0.1 m). The ZS approach was based on the computation of the zonal statistics of the DM within the root plate boundaries. For each root plate boundary, we summed all the values of the differential model pixels. To transform the sum into the volume, we multiplied the summed value by the squared size of the pixel of the DM (i.e., by 0.25^2). We compared the results on value distribution plots and tested the significance of the differences between them. Due to the lack of a normal distribution and non-homogeneous variances, we applied the nonparametric Kruskal-Wallis test (Hollander and Wolfe, 1973) and the post-hoc Dunn test (Dunn, 1964) with the Holm-Bonferroni correction of p values.

3. Results

3.1. Root plate detection

3.1.1. Mapping and detection results

The fieldwork resulted in the mapping and measurement of 317 root plates, which created a validation dataset. A total of 259 of them

Table 2
Root plate detection rate and share of false positives for six selected polygon filtering rules. Abbreviations: RP, root plate; FP, false positive; AR, area; PC, polygon compactness index; CVHP, convex hull perimeter. Optimal rule 1 was selected for further analysis.

no.	description	filtering rule	Babia Góra (B1, B2)		Gorce (G1)	
			RP detection rate [%]	share of FP [%]	RP detection rate [%]	share of FP [%]
1.	minimalisation of the FP share	AR $>$ 1 *and* PC $<$ 1.8	**62.9**	**33.2**	**67.8**	**15.2**
2.	maximalisation of the RP detection rate	CVHP $<$ 13 *and* CVHP $>$ 2.2	**86.1**	**57.2**	**89.6**	**59.9**
3.	optimal rule 1	AR $>$ 0.9 *and* PC $<$ 2.2	**70.8**	**34.7**	**79.1**	**22.2**
4.	optimal rule 2	AR $>$ 1 *and* PC $<$ 2.2	**67.3**	**33.3**	**79.1**	**20.2**
5.	optimal rule 3	AR $>$ 1 *and* PC $<$ 2.3	**67.3**	**34.3**	**80**	**20.7**
6.	optimal rule 4	AR $>$ 1 *and* PC $<$ 2.1	**65.8**	**33.8**	**78.3**	**19.6**

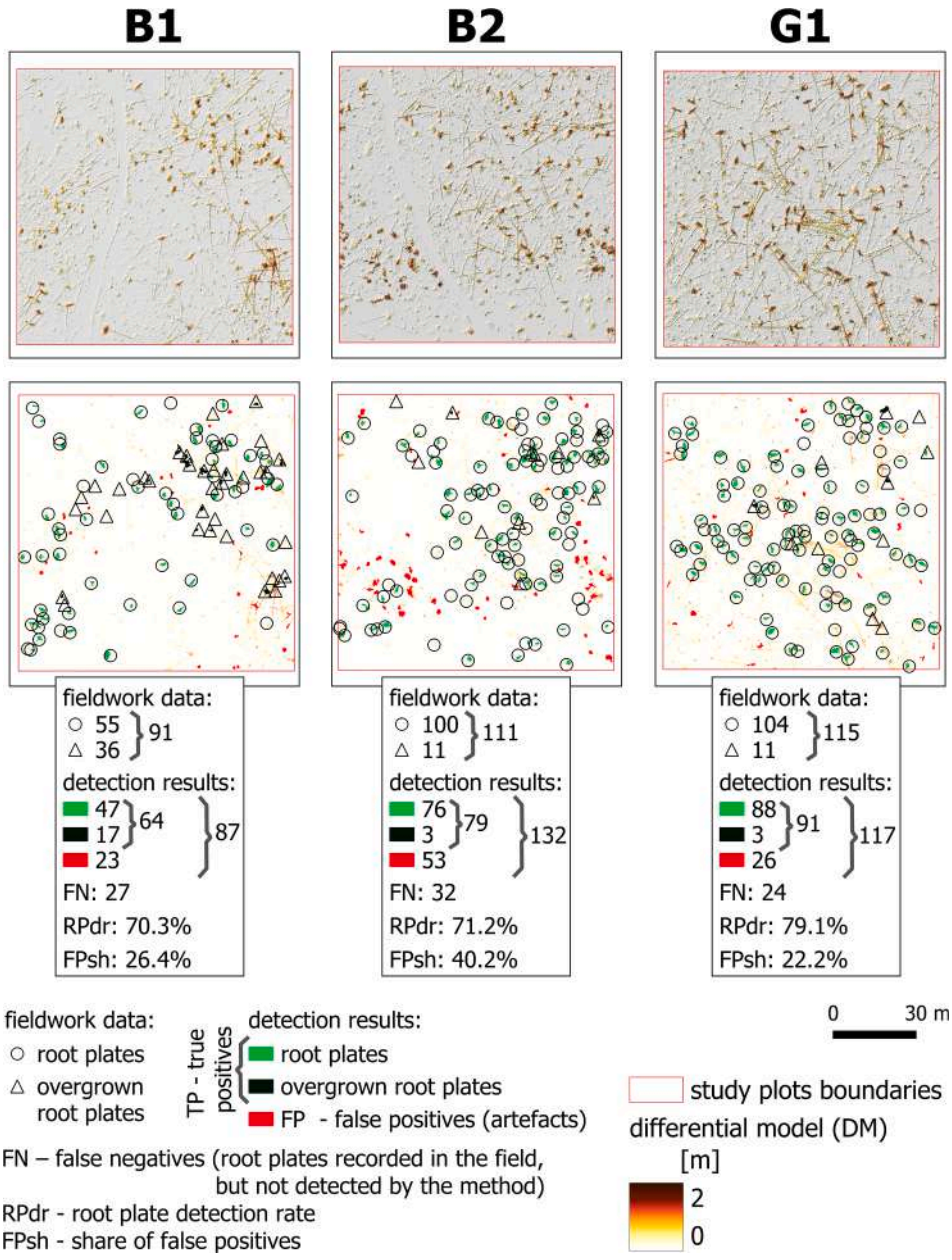

Fig. 5. Differential model (DM) for all study plots and root plate detection results for 1) field mapping and 2) the proposed method using optimal filtering rule 1 (see Table 2, no. 3) on all study plots.

belonged to category 1 (fresh, clearly visible), while 58 belonged to category 2 (overgrown or eroded). In study plots B2 and G1, the majority of the root plates represented category 1 (Fig. 5). The analysis showed that not very deeply processed LiDAR data can be successfully applied to detect root plates. The method accuracy depended on the following: 1) the selected polygon filtering rule (Section 3.1.2), 2) the DM (Section 3.1.3), and 3) the LiDAR data quality (Sections 2.2.1 and 3.1.4). Optimal filtering rule 1 (Table 2, no. 3) allowed us to achieve a high root plate detection rate of 70–80 %. The highest precision was obtained for the G1 plot. This method was slightly less accurate for B1 and B2 (Table 2, Fig. 5). In the G1 study plot, 91 out of the 115 root plates were detected (79.1 %). In the B2 study plot, the method correctly indicated the positions of 79 out of the 111 root plates (71.2 %). In the B1 study plot, 64 out of 91 root plates were detected (70.3 %) (Fig. 5). The lowest proportion of false positives reached 22.2 % of all detection results (117) in G1. The lowest number of false positives (23 polygons, 26.4 %) was found for B1. The highest rate of false positives (40.2 %) was found for B2, where 53 out of 132 detected polygons were false positives (Fig. 5). Root plates mapped in the field but not detected by the method (false negatives, FNs) were: 1) eroded to a significant extent, 2) overgrown by vegetation, or 3) pinned by tree stems (Table 3). In rare cases, the false negatives were related to root plates that originated after the date of the LiDAR survey but before the fieldwork.

3.1.2. Procedure for finding the optimal filtering rule for DM-derived polygons

Several filtering rules could be proposed for DM-derived polygon filtering aimed at reducing the number of false positives (Table 2). Based on the obtained results, we recommend using optimal filtering rule 1 (area > 0.9 and polygon compactness index < 2.2; Table 2, no. 3), which was applied in this study to extract root plate locations (Section 3.1.1, Fig. 5). For both research sites (Babia Góra, Gorce), this rule was able to correctly indicate locations of above 70 % of the root plates, while the share of false positives was less than 35 %. The parameters applied in

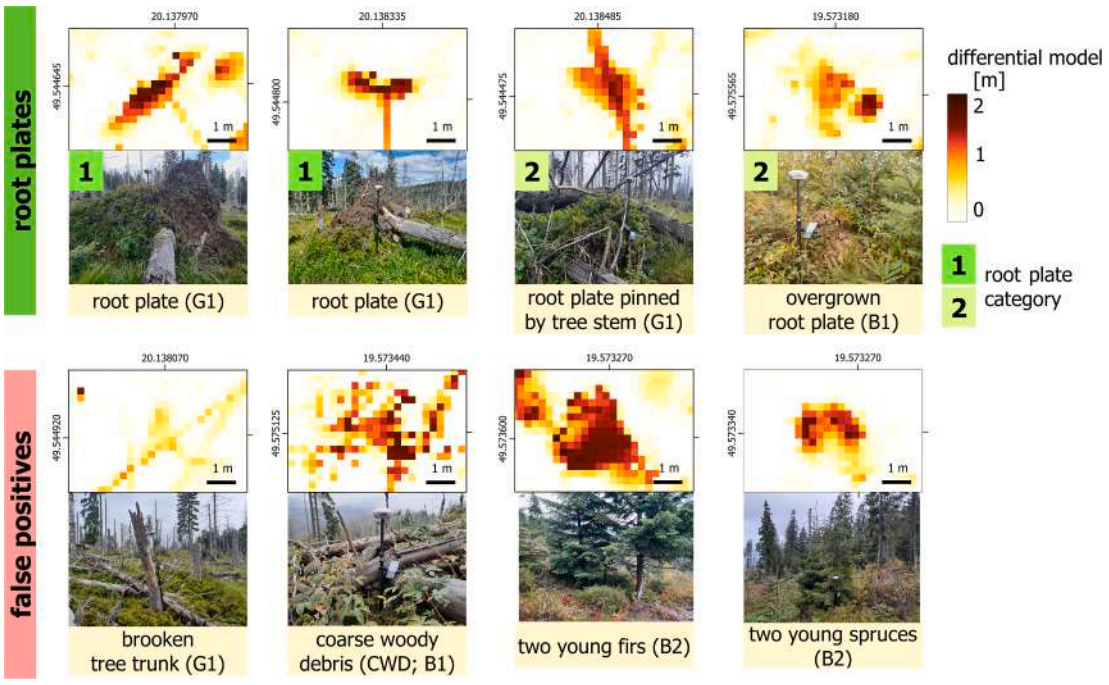

Fig. 6. Characteristic examples of different object types visible in the differential model (DM): root plates (categories 1 and 2; for details, see Section 2.2.2) and false positives (broken tree trunks, coarse woody debris and young trees). Study plot IDs are in parentheses.

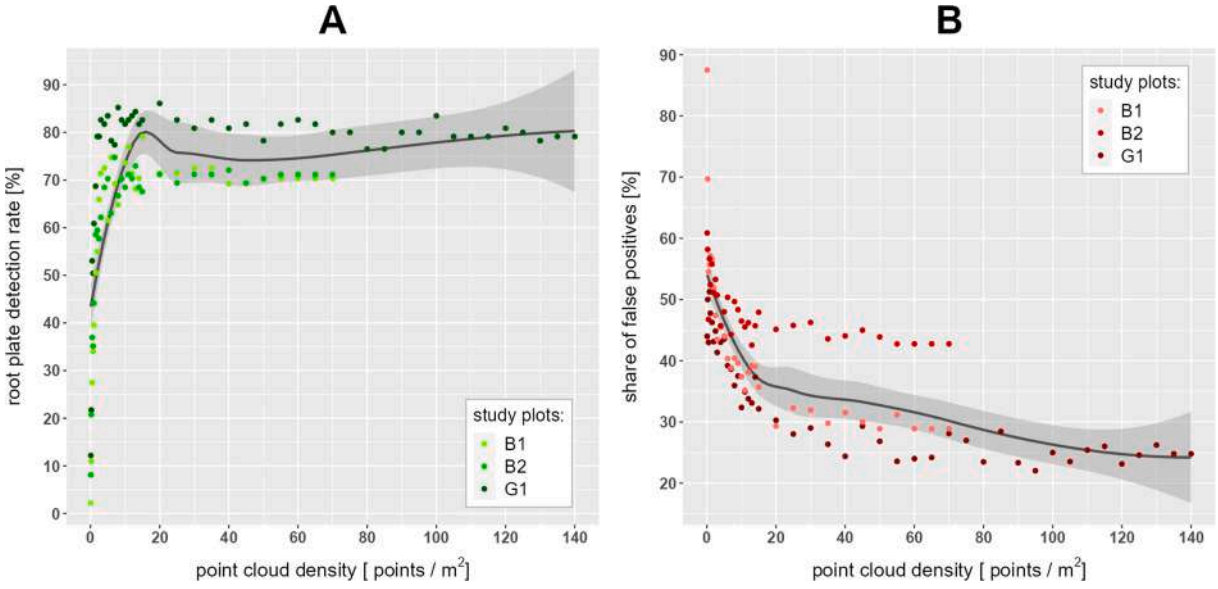

Fig. 7. A – Relationship between the root plate detection rate and the point cloud density. B - Relationship between the share of false positives and the point cloud density. The results were computed basing on optimal filtering rule 1 (for details, see Table 2, no. 3).

Table 3
Number of different understory objects distinguishable in the differential model and mapped in the field and of different types of root plates in category 2 mapped in the field divided into study plots.

object category	study plot		
	B1	B2	G1
young conifers	16	53	6
CWD piles	8	1	1
brooken tree trunks	1	3	9
root plates pinned by tree stems	6	3	4
root plates overgrown by vegetation	14	3	–
eroded root plates	16	5	7

optimal filtering rule 1 were characterized by some variability in the distribution of values between the root plates and false positive groups. For area (AR), the majority of false positives had area values less than 0.64 m^2 (3rd quantile). The area of the majority of the root plates was greater than 0.69 m^2 (the 1st quantile value) (Fig. 4A). Booth values were almost the same (0.05 m^2 difference). Hence, for the AR parameter the value being around the 3rd quantile of FP and the 1st quantile of RP (i.e. 0.7 m^2) was considered as an initial threshold value. Then we tested other decimal threshold values in the specified neighbourhood of the initial threshold. In this study, we checked the values in the neighbourhood of +/- 0.3, i.e. 0.4–1 (Table 2S). For the polygon compactness index (PC), almost all values of descriptive statistics measures for the

root plate (RP) and false positive (FP) groups were nearly the same (Fig. 4B). However, in the FP group, the maximal PC value was 4.25, while in the RP group − 2.38. For the PC parameter, the initial threshold value of 2.0 was obtained through 1) GIS analysis of the polygons and 2) visual analysis of the distribution plot. Then the decimal threshold values in the neighbourhood of +/-0.3 were checked (Table 2S). For AR and PC, other initial threshold values and neighbourhood values may be specified when aligning the method for a different dataset. The Mann-Whitney *U* test indicated significant differences between RPs and FPs for the area (p value < 0.0001) and the polygon compactness index (p value < 0.0001) (Fig. 4A, B).

The other filtering rules presented in Table 2 achieved different RP detection rates and FP shares. The filtering rule that correctly detected the highest number of root plates reached 89.6 % and 86.1 % for the G1 and B1&B2 plots, respectively. However, this high RP detection rate was accompanied by a high share of FPs, up to 59.9 % for G1 and 57.2 % for B1&B2 (Table 2, no. 2). A filtering rule that significantly reduced the share detected 67.8 % of the RPs in G1 (with a FP share of 15.2 %) and 62.9 % of the RPs in the B1&B2 plots (with a FP share of 33.2 %) (Table 2, no. 1). The presented optimal filtering rules detected 65.8–70.8 % of the RPs in B1&B2 and 79.1–80 % in G1. According to these rules, the share of FPs was 33.3–34.7 % for B1&B2 and 19.6–22.2 % for G1 (Table 2, nos. 3–6). Of all the tested filtering parameters (AR, PC, VHM_max, and CVHP), VHM_max was found to be inappropriate. For the analyzed optimal filtering rules, this parameter had no influence on the fluctuations in the RP detection rate. The AR and PC parameters were the most useful. CVHP was important only when maximizing the RP detection rate; however, it was associated with a high FP share (Table 2).

3.1.3. Differential model (DM) analysis

In terms of computing methods, the differential model allowed us to capture not only root plates but also different objects occurring in the understory, such as young trees, coarse woody debris (CWD) and broken tree trunks (Fig. 5, Fig. 6, Table 3). Root plates in category 1 (fresh, clearly visible) were distinguishable in the DM as elongated clusters of pixels with relatively high values (above 0.5–1 m). The trunks of the uprooted trees (which in national parks are left intact for natural decomposition) were clearly visible in the DM and, in most cases, could be linked to specific root plates. The trunks became apparent as lines consisting of pixels with values of 0.2–0.5 m and perpendicular to the longer axis of the root plates. There was also a large amount of coarse woody debris not related to any of the root plates. They appeared as lines of pixels with values above 0.2 m. Regarding the CWD piles, the pixel values were above 1.5 m (Fig. 6, Table 3). Considering the root plates of category 2 (overgrown or eroded), the clusters of pixel values were not as elongated as those in the case of the root plates of category 1. For the root plates in category 2, the tree trunks were frequently not clearly visible. In several cases, the CWD was located on the top of the root plates of category 2, causing difficulties in identifying clusters of pixels related to the root plate (Fig. 6, Table 3). The number of root plates in category 2 that were pinned by tree stems, overgrown by vegetation and eroded divided into study plots is presented in Table 3. In some cases, different understory objects were also distinguishable in the DM (Fig. 6, Table 3). Standing broken tree trunks were visible in the DM as clusters of pixels with values less than 1 m. Young coniferous trees were represented in the DM as circular or elongated groups of pixels with values greater than 0.5 m. In most cases, for such clusters, there were no linearly shaped pixels related to the fallen tree trunk (Fig. 6, Table 3).

3.1.4. Impact of point cloud density on the root plate detection rate

Identifying the optimal point cloud density for root plate detection is crucial for 1) assessing the possibility of using given LiDAR data to detect root plates, 2) performing computations as quickly and efficiently as possible, and 3) minimizing the disc space occupied by point cloud data. The tests performed indicated the significant impact of point cloud density on 1) the number of detected root plates and 2) the share of false positives. The root plate detection rate achieved the highest level for a point cloud density interval of 8–20 pts/m^2 (Fig. 7A). The share of false positives decreased as the point cloud density increased (Fig. 7B). The highest root plate detection rate, above 85 %, was achieved in G1 for a point cloud density of 20 pts/m^2. For plot B1, the highest root plate detection rate of nearly 80 % was reached with a point cloud density of 17 pts/m^2. Considering plot B2, using the point cloud with a density of 8 pts/m^2 resulted in the highest root plate detection rate of approximately 75 %. For a point cloud density interval of 0.1–8 pts/m^2, the root plate detection rate exponentially increased. For the B1 and B2 study plots, the root plate detection rate decreased when the point cloud density interval was 18–25 pts/m^2. For plot G1, this decrease was noted in the point cloud density interval of 20–30 pts/m^2. In all the study plots, for point cloud densities above 25 pts/m^2, the root plate detection rate was constant at 70–85 % (Fig. 7A). The decrease in the share of false positives was the greatest with the point cloud density interval of 0.1–18 pts/m^2. For point cloud densities above 18 pts/m^2, the FP share slowly decreased in the interval of 33–22 % for plots G1 and B1 and 46–43 % for plot B2 (Fig. 7B).

3.2. Biotransport estimation

After applying three approaches (FM, CNT, ZS), in most cases, the estimated biotransport was not equal (Fig. 8). The contour lines (CNT) approach resulted in lower estimations of biotransport than did the zonal statistics (ZS) approach. The Kruskal-Wallis test confirmed the statistical significance of these differences. The difference between CNT and ZS was significant (adjusted p-value $p_{Holm\text{-}adj} = 0.03$) (Fig. 8). At B1, the volumes estimated using FM were lower than those estimated using CNT and ZS, and the differences FM − CNT and FM − ZS were significant ($p_{Holm\text{-}adj} = 0.02$ and $p_{Holm\text{-}adj} < 0.0001$, respectively). In this study plot, there was no significant difference between volume values calculated applying the CNT and ZS approaches (Fig. 8, B1). For plot B2, no significant differences were found (Fig. 8, B2). Considering plot G1, the volumes estimated using FM were significantly lower than those estimated using point cloud ($p_{Holm\text{-}adj} < 0.0001$), and there was no statistically significant difference in the distribution of volume values between CNT and ZS (Fig. 8, G1). According to the field measurements, the mean root plate volume was 2.2 m^3 (2.11 m^3 in B1, 2.45 m^3 in B2 and 2.01 m^3 in G1). When considering the CNT approach, the mean root plate volume was 2.99 m^3 (2.82 m^3 in B1, 2.5 m^3 in B2 and 3.56 m^3 in G1). According to the ZS approach, the mean root plate volume reached 3.35 m^3 (3.16 m^3 in B1, 2.83 m^3 in B2 and 3.96 m^3 in G1). The mean biotransport and the overall biotransport divided into particular plots (each with an area of 1 ha) are presented in Table 4.

4. Discussion

4.1. Factors impacting the accuracy of the proposed method

We showed that root plates can be detected with the use of LiDAR point clouds. The volume of individual root plates can also be calculated; thus, we can automate the biotransport estimation driven by the treethrow process. However, the accuracy of the method described in this study depends on many factors, which can be divided into two major groups: 1) environmental factors and 2) factors related to data acquisition and processing. The environmental factors include 1) forest ecosystem recovery after wind disturbance, 2) the size and shape of root plates and 3) the size and spatial configuration of coarse woody debris (CWD). With respect to root plate detection, the data-related factors include 1) the point cloud density, 2) the method of differential model computation, and 3) the filtering rules of DM-derived polygons. Considering the biotransport estimation, the data and processing-related factors include 1) fieldwork data quality, 2) accuracy of the root plate boundary delineation, and 3) the adopted volume computation

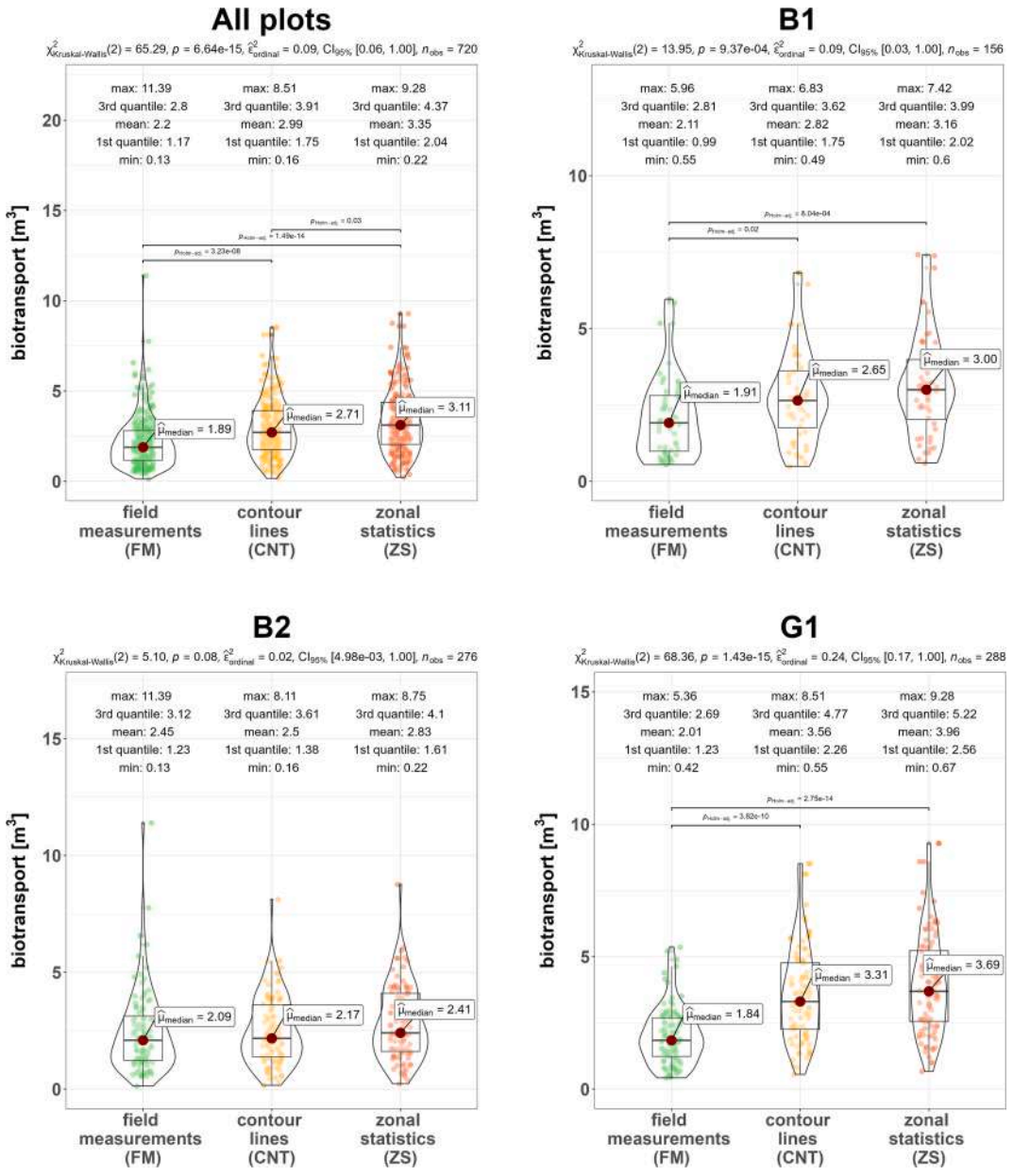

Fig. 8. Biotransport driven by tree uprooting estimated using field measurements and two proposed methods: contour lines and zonal statistics. Biotransport was calculated for 1) all study plots, 2) plot B1, 3) plot B2, and 4) plot G1.

Table 4
Overall biotransport estimated in m^3/ha using three different methods (FM, CNT, ZS).

method	B1 [m^3/ha]	B2 [m^3/ha]	G1 [m^3/ha]	all plots (3 ha) [m^3]	mean [m^3/ha]
FM	109.59	225.33	193.37	528.29	176.1
CNT	146.6	229.97	341.32	717.89	239.3
ZS	164.36	260.64	379.87	804.87	268.3

approach. We discuss also the key parameters of the method that may be important during its application.

4.1.1. *Factors affecting root plate detection*

Environmental factors strongly control the results of the root plate detection workflow. Under the conditions of mid-latitude natural coniferous forests, forest ecosystem recovery after wind disturbance is driven mainly by spontaneous plant succession. In the Norway spruce-dominated forests of the Western Carpathians (occurring in the study plots), the windthrow areas were overgrown with silver birch (*Betula pendula* Roth), goat willow (*Salix caprea* L.), rowan (*Sorbus aucuparia* L.), and blackberry (*Rubus fruticosus* L.). There were also seedlings of Norway spruce and other tree species, such as silver fir (*Abies alba* Mill.) and European beech (*Fagus sylvatica* L.) (Franczak, 2013). The results of the root plate detection might be controlled by the extent and structure of the revegetation at the study site. The presented method achieved the best result for the least overgrown study plot G1 (Fig. 5). The high number of false positives in B2 (Fig. 5) may be related to the presence of several young conifers in this plot (Table 3, Fig. 6). Within all the study plots, deciduous trees (mainly silver birch) grew on the root plates of category 2. However, deciduous trees did not contribute to the occurrence of false positives due to better penetration (compared to conifers) by the laser beam, especially during the leaf-off season.

Root plates have different shapes and sizes controlled by tree features (e.g., tree species, tree height and the properties of the root system) and abiotic factors (e.g., soil and bedrock properties) (Schaetzl et al., 1989).

Therefore, the representation of individual root plates in the differential model can vary. One root plate may sometimes form due to the uprooting of two or more trees (Schaetzl et al., 1989). Such root plates are usually larger than forms originating from one uprooted tree. When developing the method, the influence of tree species was not considered, as all the mapped root plates were formed by uprooted Norway spruces. Perhaps the developed methods may also be effective for evaluating root plates produced by other tree species. This requires further research involving the calibration of different parameters and steps of the root plate detection method.

The method was developed for Norway spruce, as this tree species is very prone to uprooting due to the morphological properties of its roots, as it can form shallow, wide, disc-shaped root systems (Tjoelker et al., 2007). The probability of Norway spruce uprooting increases for 1) swampy areas with high levels of groundwater and 2) shallow soils, which occur on steep slopes or on boulders. Moreover, under the climatic conditions of many mid-latitude mountain ranges (including the Polish Carpathians), Norway spruce overgrows in high-altitude areas, which are more exposed to high wind speeds than lower-lying slopes. Under such conditions, Norway spruce stands are more likely to be damaged by hurricane-force winds than stands of other species (Mitchell, 2013). Gradation by insects, mainly the bark beetle (*Ips typographus* L.), and prolonged drought periods, cause a decrease in health conditions of Norway spruce and may increase the vulnerability of stands to wind damage (Grodzki et al., 2006; Buma, 2015). All of the abovementioned factors contribute to the lower resilience of Norway spruce forest stands to wind-driven damage.

Coarse woody debris accumulates within the forest bottom during and after forest damage events, and if not collected by foresters, it can be an important source of biomass. One root plate is associated with at least one CWD piece, so the number of CWD piles is at least as large as the number of root plates. During extreme wind events, CWD can also form as a result of stem breakage (Mitchell, 2013). This may increase the amount of CWD at a particular windthrow site. The CWD hindered the detection of root plates with the use of the proposed method when it was lying 1) on the top of the root plate or 2) near the root plate. In both cases, the presence of CWD caused an increase in the complexity of the polygons extracted from the DM, which reduced the probability of root plate detection. Piles of CWD, individual logs and snags sometimes produced false positives (Fig. 6, Table 3). In contrast, the tree trunks related to particular root plates were often clearly visible in the DM. In future analyses, such CWD might be applied to extract information about the direction (azimuth) of uprooted trees.

The performance of the proposed method was affected by factors related to the data and to the processing techniques. The point cloud density is important for accurate root plate detection (Fig. 7). Point clouds of low density lower the method efficiency due to an insufficient amount of data. We recommend using point clouds with densities greater than 8 pts/m^2. Similar results were obtained for CWD detection, where a point cloud density less than 1 pts/m^2 caused a significant decrease in the detection rate. In this case, a point cloud density greater than 16 pts/m^2 was considered appropriate for detecting CWD in northeastern Minnesota, United States (Joyce et al., 2019).

For differential model computation, using the last return points located up to 2 m above the ground resulted in a satisfactory level of accuracy of the root plate detection algorithm. A similar approach involving a maximum height filter of 1.3 m above the ground was previously applied to detect CWD (Joyce et al., 2019). However, the approach implemented in the present study allowed the extraction of root plates from LiDAR data but was not able to remove all false positives. The most common false positives were young conifers (Fig. 6, Table 3), whose branch height was 0–2 m above the ground. They had a very dense cover of branches and needles, and for this reason, the laser beam could not penetrate through them. Therefore, the laser reflections from young conifers were saved in the LiDAR data as the last return points. Similarly, the laser reflections from CWD or broken tree trunks were also the last return points.

The aim of the DM analysis was to reduce the number of false positives resulting from the above-described LiDAR point patterns. The parameters tested in the procedure for finding the optimal filtering rule were related to the geometry of the polygons (AR, PC, and CVHP; see Table 2). This approach was successful at discriminating between root plates and false positives (Table 2). The procedure of finding the optimal filtering rule allowed us to find optimal threshold values of the area parameter (Table 2, Fig. 4A). The applied procedure involving the PC enabled the removal of complex polygons usually marking the locations of CWD or young conifers (Table 2, Fig. 4B, Fig. 6). The VHM_max parameter was found to be useless mainly because of 1) the similar heights obtained for young conifers and for some root plates overgrown by young deciduous trees and 2) the tall tree branches located above the root plates. The direct proportionality of the relationship between the root plate detection rate and the share of false positives detected in the group of all tested queries (Fig. 4C) reflects the general observation that if a given rule returns more root plates, it also returns more false positives.

Of the different factors related to the data and processing, the results of the root plate detection workflow were influenced mostly by the DM computation procedure and by the DM-derived polygon filtering rules. The point cloud density seems to be less meaningful as long as it is at a sufficient level of $\geq$ 8 pts/m^2. The applied fieldwork procedure for root plate mapping was accurate and allowed us to acquire precise location data. Double-checking of the study plots ensured that all the root plates were mapped; thus, mistakes resulting from fieldwork data are very unlikely. All of the abovementioned environmental factors presumably affected the detection results to a similar extent. The presented approach performed well and detected most of the root plates (Fig. 5) despite the passage of time since the occurrence of wind-driven forest damage (Fig. 1) and the growth of the young tree generation. However, further research is needed to test the method for different tree species and for different environmental conditions (topography, forest type, etc.).

4.1.2. Issues related to biotransport estimation

The point cloud-based results of the biotransport estimation depended on the same environmental factors as the output of the root plate detection. Generally, for several reasons, environmental factors cause overestimation of the root plate volume. If a root plate was overgrown by dense young trees that blocked the laser beam (17 cases; Table 3), the differential model could have greater values, and the pixel cluster representing such a root plate was complex (Fig. 6), which contributed to volume overestimation. Regarding the root plate shape, narrow and newly created root plates formed an overhang at the site opposite the fallen tree trunk (Schaetzl et al., 1989), which was observed mainly in plot G1. Under this overhang, there was no soil or roots, just empty space; thus, the volume of soil and roots should not be taken into account when estimating the root plate volume. The airborne LiDAR laser beam cannot penetrate this region to measure its dimensions. Therefore, in such cases, the volume of the space under the overhang was included in the overall root plate volume. However, our field survey confirmed that such cases were quite rare and therefore had limited impact on volume estimates. Considering the presence of CWD, in rare cases, CWD located on the top of a root plate (Table 3) increased the values of the DM. More frequently, smaller or larger parts of fallen tree trunks (root necks) were incorporated into root plate boundaries (20 cases in B1, 32 in B2 and 37 in G1).

The factors related to the data and processing may also influence the estimated biotransport. Regarding the root plate boundaries, the delineation algorithm based on a DM threshold value of 0.1 m and on a 1-m buffer around the root plate polygon (Fig. 3) could lead to the incorporation of the root plate boundary, not only the pixels representing the root plate lying outside the root plate polygon. Within the 1-m buffer, pixels related to 1) fallen tree trunks (root neck) and 2) dense shrubs or young conifers were also included. This may slightly increase the

estimated root plate volume. Root plates neighbouring other CWD, shrubs and young conifers could experience additional volume overestimation. Considering the possible impact of the different approaches for volume computation, the slightly lower results of the CNT than those of the ZS approach (Fig. 8) could be related to the way the volume was estimated by these approaches. The volume computed using the overlapped polygons – slices with thickness of 0.1 m representing the DM contour lines (CNT) – seems to better represent the real shape of the root plate than the cuboids arranged side-by-side with base sides of 0.25 × 0.25 m and heights equal to the DM (ZS) pixel value (Fig. 3). The ZS approach may also overestimate the volume because the parts of some pixels slightly protrude from the root plate boundaries.

During the fieldwork, we measured the root plate dimensions as accurately as possible to reduce errors resulting from measurement inaccuracies. The equation applied to estimate root plate volumes (Norman et al., 1995) is widely known and applied (Dąbrowska, 2009; Strzyżowski et al., 2018). This equation is considered a close approximation of the root plate volume (Pawlik, 2013). Other equations have also been used (Reid, 1981; Putz, 1983; Beatty and Stone, 1986; Burns and Tonkin, 1987; Gabet and Mudd, 2010; Richards et al., 2011). We think that the equation applied in this study helps to accurately estimate the root plate volume. However, such an estimate is limited to 1) three values for each root plate and 2) approximating the root plate shape to half of a rotational ellipsoid. The approaches based on LiDAR data use several dozen DM pixel values for each root plate. Thus, the CNT and ZS may better approximate the root plate volume than the FM. The approaches based on point cloud (CNT, ZS) have several advantages over the FM approach, as they allow us to 1) quickly estimate the root plate volume, 2) reduce the cost and time required for fieldwork, 3) widen the spatial scale of the analysis, and 4) estimate and compare the root plate volume for different time periods, depending on the LiDAR data availability. Although the results of the applied methods differed ($p < 0.001$; Fig. 8), they had similar magnitudes. Thus, point cloud-based approaches can be valuable alternatives to approaches based on field measurements.

4.1.3. Key parameters of the method

The proposed method of root plate detection and biotransport estimation has several key parameters that may be important when the method is applied 1) for different environmental conditions, and 2) for LiDAR data with different properties. These parameters include 1) the height above the ground of the last return points to be interpolated as DM, 2) spatial resolution, 3) contour line interval and the heights of the contour lines for polygonization, 4) the rule of the root plate polygons filtering, and 5) the buffer distance and minimum DM value while delineating the RP boundary.

The DM was interpolated using the last returns located up to 2 m above the ground. The majority of root plates in all study plots had a height lower or slightly higher than 2 m. Filtering the point cloud using the 2 m above ground height threshold allowed to capture all root plates in the DM. However, when performing the analysis for root plates significantly higher or significantly lower than 2 m this threshold should be around the maximal possible height of the root plates. The spatial resolution of 0.25 m was considered effective and optimal for research on root plates. Using higher resolution will result in smoother and more detailed DM and may improve the accuracy of root plate volume estimation. Nevertheless, computations in a higher resolution will be time-consuming, and the quality of the final result may be similar to the result presented in this paper. Applying lower resolution may shorten the computation time, but can also lead to incorrect results, as the pixel size will be too big to effectively present the root plate shape. The contour lines at the heights of 0.5, 1, and 1.5 m had oval, closed shapes on root plates. Applying three height thresholds enabled the detection of root plates of different sizes. The number of height thresholds may be lower, and the threshold elevations can be different, depending on the specific properties of the investigated root plates. However the shape of the contour lines extracted for polygonization is dependent on the filtering rule, i.e. all polygons that satisfy the rule (have a sufficiently large AR and a sufficiently low PC) are considered root plates. For effective detection of root plates of different sizes, we recommend using three height thresholds. The contour line interval of 0.1 m allows efficient visualization of the DM, supports the selection of different height thresholds, and provides accurate results of the volume estimation by the CNT approach. Despite this if the detailed data inspection is not required, to shorten the computing time the contour line generation could be reduced to delineate only the contours of the selected height thresholds. The filtering rule using AR and PC parameters could be modified for different study cases. However, such modification should be justified by the analysis of the distribution plots grouped into root plates and false positives. When dealing with very large root plates, the root plate polygon filtering threshold of area $< 5\ m^2$ should be increased depending on the largest root plate size observed in the field or identified during data analysis via GIS software. The parameters used in the root plate boundary delineation (buffer distance 1 m and DM >= 0.1 m) are effective for this purpose. Other values of these parameters could also be tested in future studies to optimize the way of the RP boundary extraction.

4.2. Detection of root plates and biotransport estimation in the light of previous research

The results of this study represent the first attempt to use remote sensing data (LiDAR point clouds) for the detection and volume estimation of the root plates of uprooted trees. However, numerous studies have considered a similar problem of the application of LiDAR point clouds to investigate coarse woody debris (CWD). Downed trees in Northeast Germany were identified from dense LiDAR data by applying point cloud normalization and filtering the data according to a normalized point height threshold of < 2 m and a laser echo width of $<$ 4.5 ns. This approach allowed to fully detect 37.3 % and partly detect 33.2 % of the stems (Mücke et al., 2012). For areas located in Southwest Sweden, another approach applied line template matching algorithms together with point cloud filtering using a normalized point height interval of 0.2–1 m, which resulted in 41 % precision in detecting field-measured stems (Lindberg et al., 2013). The CWD detection approach involved extracting first returns from the LiDAR data and filtering them using a normalized point height threshold of ≤ 1.3 m to extract locations where 23 % of the CWD was measured during fieldwork in areas located in Northeastern Minnesota, United States. The logistic regression models showed that CWD detection rates were greater than 50 % for logs with a diameter > 0.3 m and a point cloud density of 7–8 pulses/m^2 (Joyce et al., 2019). All of the above-described approaches used different methods of point cloud filtering, with height thresholds of 2 m, 0.2–1 m, and 1.3 m. Further filtering of the point cloud was based on laser echo width or on selecting the first returns. Similarly, we applied a height threshold of 2 m and extracted the last returns.

A method for detecting windthrown trees under a forest canopy based on the difference between two elevation models obtained from the same LiDAR data was applied for a Norway spruce-dominated stand in South Sweden. Template matching applied to the difference image allowed to detect 38 % of the trees and 89 % of the trees taller than 27 m measured in the field (Nyström et al., 2014). This approach used a differential model to locate the detected objects, which was similar to the workflow of DM computation adopted in this study. LiDAR data were used to produce different raster layers that were used in object-based image analysis (OBIA). This approach allowed to detect 73 % of the logs digitized previously on the orthophotomap (Blanchard et al., 2011). Using the point cloud with a density of 15 points/m^2 enabled detection of 78 % of the largest fallen trees (with a diameter at breast height > 3 m) in Finnland (Heinaro et al., 2021). LiDAR data were also applied to automatically detect instream dead wood via point cloud filtering and skeletonization for 9 streams located on Vancouver Island, Canada. For

different streams, the detection accuracy varied from 37- 87 %, with a mean of 63 % (Dakin Kuiper et al., 2023). Such a variation in detection rates could have been conditioned by the variability of environmental features in each studied stream (including dead wood properties). The quite low CWD detection rate reported by several studies (Nyström et al., 2014; Joyce et al., 2019) was related mainly to CWD size and point cloud density. Similarly, the root plate detection method was affected by the root plate size. The presented workflow enabled the detection of the majority of root plates of the most common sizes. However, the DM might not capture very small or very thin root plates.

Similar to the presented root plate detection and volume estimation method, the CWD detection methods were based on a deterministic approach that was quite effective at extracting the studied objects from the LiDAR data and their derivatives. Unlike most of the mentioned CWD detection approaches, we performed analysis on the raster model (DM). The DM was the base used to delineate contour lines, which were subsequently used to extract the root plate locations (Section 2.3.1). Contour lines have been applied to other relief features, such as karst landforms (Liang et al., 2014), closed depressions (Wu et al., 2015), and pit-mound topography (Godziek and Pawlik, 2023). The contour line approach is intuitive and performs well for different types of landforms, especially for microrelief forms. Perhaps other approaches (i.e., OBIA, template matching) might also be applied to extract root plates from the DM. However, due to the various environmental and technical factors (similar to those described in Section 4.1), these algorithms can also be prone to different inaccuracies. The procedure applied in this study, based on DM-derived contour lines and on filtering of selected contour line polygons, achieved a root plate detection rate of 70–80 % (Fig. 5). This accuracy is comparable to the results achieved in research on CWD detection.

The CWD detection errors were associated with clusters of downed logs and with logs covered with vegetation or under a tree canopy (Blanchard et al., 2011). The presence of dense tree canopy caused a lowering of the number or the absence of near-ground returns and hence the problems with CWD detection (Joyce et al., 2019). Similarly, the root plate detection rate in our method was also influenced by 1) vegetation overgrowing the windthrow site, and 2) the presence of root plates overlapping with CWD or with other root plates. Another source of errors was the quality of the applied elevation models and the used LiDAR data filtering rules (Mücke et al., 2012). This relates also to the study presented in this paper, as the data processing workflow and the patterns present in the data might be an important source of errors. The errors were also related to the data quality, as the detection of CWD was impossible for point clouds with a pulse density below 1 pls/m^2 (Joyce et al., 2019). Also, root plate detection was impossible for point clouds with low density (Fig. 7).

Most of the past research on root plate volume estimation was conducted in coniferous or mixed temperate forests (Kotarba, 1970; Dąbrowska, 2009; Gallaway et al., 2009; Phillips et al., 2008; Strzyżowski et al., 2018), similarly as the study presented in this paper. Some studies involved investigation of the area previously affected by the wildfire (Gallaway et al., 2009) or a windthrow caused by the tornado (Phillips et al., 2008). The obtained estimations of root plate volumes (and thus the biotransport) are similar or slightly greater than the results presented in the literature. The mean volumes estimated for different study plots located in the spruce forest belt of the Tatra Mts., Poland, varied between 1.8 and 3.6 m^3 (Kotarba, 1970), however, these results were overestimated (Norman et al., 1995). In the Slovak part of the Tatra Mts., the mean root plate volume in the spruce forest belt was estimated to be 1.9 m^3 (Dąbrowska, 2009). For natural beech-fir forests in Czechia, the mean root plate volume of Norway spruce reached 5.6 m^3 (Pawlik, 2013, after Šamonil P. (unpublished data)). The estimated mean volume of root plates in coniferous forests in North America varies from 0.7-1 m^3 in British Columbia, Canada (Gallaway et al., 2009), 2 m^3 in Arkansas, United States (Phillips et al., 2008), and up to 4 m^3 in Washington, United States (Reid, 1981). In the present study, the estimated mean root plate volume reached 2.2 m^3 for FM, 3 m^3 for CNT and 3.35 m^3 for ZS (Fig. 8). These results fit the range of Norway spruce root plate volumes estimated in the abovementioned research (1.8–5.6 m^3) and support the application of LiDAR data for root plate volume estimation. However, due to the discrepancies in results, there is a need for further research on this topic aiming at finding as accurate solution as possible.

4.3. Potential applications of the proposed method

The method proposed in this study has a wide range of applications in science and practice, particularly in geomorphology, soil science, and forest ecology and management. Root plate forms resulting from tree uprooting are important for understanding microscale slope and soil formation processes and forest ecosystem transformation related to wind-driven disturbances. Information on the quantity, spatial distribution, and volume of root plates can support the planning of fieldwork by foresters after a disturbance.

If point cloud data are available, the method may be applied to assess the amount and spatial distribution of root plates. Such analysis might be combined with root plate volume estimation (and thus biotransport estimation). Fieldwork performed at selected small areas can confirm the results of root plate detection and volume estimation. This approach can also enable the evaluation of 1) the impact of treethrow on pit-mound microrelief formation and 2) the influence of different environmental factors (tree stand properties, topography, etc.) on the intensity and occurrence of tree uprooting. Estimating the root plate volume with the use of point clouds acquired by repeated scanning during different periods may help to assess the rate of root plate erosion and deterioration. Because root plate mapping is time-consuming and often difficult in steep mountain areas, the spatial extent of past studies on this topic is rather limited (Schaetzl and Follmer, 1990; Pawlik et al., 2013; Šamonil et al., 2015; Phillips et al., 2017; Strzyżowski et al., 2018; Greenwood et al., 2021). The method described in this study may facilitate geomorphological research on root plates and expand their spatial and temporal scope.

Considering the potential applications in soil science, the developed method may be important for assessing the impact of tree treethrow on soil mixing and development. This method may allow us to map zones with different degrees of tree uprooting impact on soils. Other applications include 1) finding and selecting study sites appropriate for analyzing soil formation under the influence of treethrow and 2) exploring the relationships between tree uprooting frequency and soil properties and age. The workflow of root plate volume estimation applied to multitemporal LiDAR data could be used to estimate 1) the root plate deterioration rate over time and 2) the soil turnover time (i.e., to count how many times a given soil could be transformed by the tree uprooting process). Previous studies have linked the tree uprooting process to the impact of trees on soils and their properties (Šamonil et al., 2010b; Richards et al., 2011; Kooch et al., 2012). The presented method may aid further investigations of the relationship between treethrow and soils.

The method can also be applied in forest ecology research. A forest ecosystem is a dynamic assemblage of various natural components that develop and change over time (Mitchell, 2013). Investigating post-disturbance forest recovery processes is crucial to understanding long-term forest dynamics (Buma and Schultz, 2020; Buma and Wessman, 2011). Specifically, the method could be applied to 1) delineate forest stands affected by strong winds, 2) quantify the amount of wind-driven forest damage, and 3) find potential study sites for detailed ecological research on windthrows. The root plate volume estimation workflow applied to multitemporal LiDAR data could be used to investigate the impact of root plate erosion on changes in understory plant communities, for example, plant succession on root plates. The method may be applied to monitor long-term changes in the spatial distribution of windthrows and post-disturbance forest recovery.

The practical applications of the proposed method are seen in

forestry, particularly in forest management and protection. ALS LiDAR surveys have become cheaper and easier to perform with the use of UAVs. Since the late 1990 s and early 2000 s, LiDAR data have been widely used in forestry (Means et al., 1999; Pirotti, 2011; Lisiewicz et al., 2022). Moreover, point cloud data are increasingly important, especially in areas affected by forest damage, including damage caused by wind. When acquiring LiDAR data just after damage, the workflow of root plate detection may be used to create an inventory of potential root plates. This may accelerate the planning of forest works after a windthrow event. The root plate can also be a source of wood. Therefore, foresters can use the proposed root plate detection algorithm to extract locations and estimate the potential number of root systems harvested during forest works. In addition, slopes affected by windthrow have an increased susceptibility to erosion and thus may be less stable (Strzyżowski et al., 2021; Mauri and Tarolli, 2023). Hence, the method can be applied by geotechnical engineers to 1) delineate the zones affected by the treethrow process and 2) assess the scale of impact of this process on soil. Such information can be used for further study of different soil properties, which can help to assess slope stability. The method can also be applied in forest protection to delineate and monitor windthrow areas, which should be placed under strict protection to observe the natural processes of forest recovery.

5. Conclusions

In different types of forest ecosystems around the world, tree uprooting plays crucial role in long-term forest dynamics. Applying point cloud data to investigate the effects of treethrow may improve the understanding of the scale and course of various environmental processes related to this phenomenon. The novel approach presented in this study might be widely applied to map root plates and estimate their volume. This could lead to significant progress in numerous scientific fields, such as geomorphology, soil science and forest ecology. The development of potential practical applications of the presented method may contribute to progress in forest management and protection.

The analysis presented in this study indicated that LiDAR point cloud data can be applied to 1) extract the location of the root plates of uprooted trees and 2) estimate their volume, and hence to estimate the biotransport driven by the tree uprooting process. The fieldwork allowed us to compare the results of point cloud processing with the real locations of the root plates and thus to validate the performance of the chosen approach. The root plate detection rate was 70–80 %. The results of the root plate volume estimation fit the range of past estimations from various regions and forest ecosystems. In future studies, field root plate measurements and volume estimations could be independently confirmed by using LiDAR data and the method presented in this study. However, the method accuracy was negatively affected by environmental and data-related factors. Despite these difficulties, the method achieved efficient performance (Fig. 5, Fig. 8).

Based on the presented results, several recommendations can be proposed. 1) The minimum LiDAR data density to apply the proposed method is 8 pts/m^2. 2) The method was developed based on root plates of uprooted Norway spruces; thus, we recommend applying the presented workflow to such stands. When applying this method to other tree species, the height of the contour lines used to extract root plates from the DM and the polygon filtering rule (threshold values for AR and PC) may require changes. 3) The occurrence of young conifers may increase the number of false positives; hence, for windthrows overgrown by such young trees, we recommend treating the results with caution. For such windthrows, the possible overestimation of the number of root plates results from a compromise between the accuracy of the method and its applicability for large areas. 4) We recommend using a raster spatial resolution of 0.25 m (as in this study), which is a good compromise between a sufficient level of detail and possibly the lowest amount of disc space required. 5) The method was developed for protected forest stands located in national parks; thus, we recommend the described workflow mainly for monitoring strictly protected stands or forests mostly undisturbed by human activity. When using this method in forest management, LiDAR data should be acquired before starting any forestry work that may disturb the root plate layout.

CRediT authorship contribution statement

Janusz Godziek: Writing – review & editing, Writing – original draft, Visualization, Validation, Software, Resources, Methodology, Investigation, Formal analysis, Data curation, Conceptualization.

Declaration of competing interest

The authors declare that they have no known competing financial interests or personal relationships that could have appeared to influence the work reported in this paper.

Data availability

Data will be made available on request.

Acknowledgements

This study was supported by the Polish National Science Centre - Narodowe Centrum Nauki (grant no. 2019/35/O/ST10/00032). The author would like to thank Tomasz Lamorski from Babia Góra National Park and Paweł Czarnota from Gorce National Park for assisting in obtaining LiDAR data from the National Parks and for providing information on the forest history of the selected study areas. The author would also like to thank Łukasz Pawlik and two anonymous reviewers for providing insightful comments that significantly improved the quality of the manuscript. The author is grateful to Izabela Godziek for the help during the fieldwork.

Appendix A. Supplementary material

Supplementary data to this article can be found online at https://doi.org/10.1016/j.jag.2024.103992.

References

ASPRS, 2011. LAS Specification 1.4 - R15. American Society for Photogrammetry and Remote Sensing. Online: https://www.asprs.org/wp-content/uploads/2019/07/LAS_1_4_r15.pdf.

Barker Plotkin, A., Schoonmaker, P., Leon, B., Foster, D., 2017. Microtopography and ecology of pit-mound structures in second-growth versus old-growth forests. For. Ecol. Manage. 404, 14–23. https://doi.org/10.1016/j.foreco.2017.08.012.

Beatty, S.W., Stone, E.L., 1986. The variety of soil microsites created by tree falls. Can. J. For. Res. 16, 539–548. https://doi.org/10.1139/x86-094.

Blanchard, S.D., Jakubowski, M.K., Kelly, M., 2011. Object-based image analysis of downed logs in disturbed forested landscapes using lidar. Remote Sens. (Basel) 3, 2420–2439. https://doi.org/10.3390/rs3112420.

Bonannella, C., Parente, L., De Bruin, S., Herold, M., 2024. Multi-decadal trend analysis and forest disturbance assessment of European tree species: concerning signs of a subtle shift. For. Ecol. Manage. 554, 121652 https://doi.org/10.1016/j.foreco.2023.121652.

Brinkhoff, T., Kriegel, H.-P., Schneider, R., Braun, A., 1995. Measuring the complexity of polygonal objects. ACM-GIS 109.

Buma, B., 2015. Disturbance interactions: characterization, prediction, and the potential for cascading effects. Ecosphere 6, art70. https://doi.org/10.1890/ES15-00058.1.

Buma, B., Schultz, C., 2020. Disturbances as opportunities: Learning from disturbance-response parallels in social and ecological systems to better adapt to climate change. J. Appl. Ecol. 57, 1113–1123. https://doi.org/10.1111/1365-2664.13606.

Buma, B., Wessman, C.A., 2011. Disturbance interactions can impact resilience mechanisms of forests. Ecosphere 2, art64. https://doi.org/10.1890/ES11-00038.1.

Burns, S.F., Tonkin, P.J., 1987. Erosion and sediment transport by windthrow in a mountain beech forest, New Zealand., in: Beschta, R.C., Blinn, T., Grant, G.E., Iceland, G.G., Swanson, F.J. (Eds.), Erosion and Sedimentation in the Pacific Rim. International Association of Hydrological Sciences, pp. 269-270.

Constantine, J.A., Schelhaas, M.-J., Gabet, E., Mudd, S.M., 2012. Limits of windthrow-driven hillslope sediment flux due to varying storm frequency and intensity. Geomorphology 175–176, 66–73. https://doi.org/10.1016/j.geomorph.2012.06.022.

Dąbrowska, K., 2009. The morphogenetic impact of the bora type wind (19thNovember 2004) on the relief of Danielov dom area (The High Tatras). Landform Analysis 11, 5–10.
Dakin Kuiper, S., Coops, N.C., Jarron, L.R., Tompalski, P., White, J.C., 2023. An automated approach to detecting instream wood using airborne laser scanning in small coastal streams. Int. J. Appl. Earth Obs. Geoinf. 118, 103272 https://doi.org/10.1016/j.jag.2023.103272.
Doane, T.H., Edmonds, D., Yanites, B.J., Lewis, Q., 2021. Topographic roughness on forested hillslopes: a theoretical approach for quantifying hillslope sediment flux from tree throw. Geophys. Res. Lett. 48 https://doi.org/10.1029/2021GL094987.
Dubayah, R., Blair, J.B., Goetz, S., Fatoyinbo, L., Hansen, M., Healey, S., Hofton, M., Hurtt, G., Kellner, J., Luthcke, S., Armston, J., Tang, H., Duncanson, L., Hancock, S., Jantz, P., Marselis, S., Patterson, P.L., Qi, W., Silva, C., 2020. The global ecosystem dynamics investigation: high-resolution laser ranging of the Earth's forests and topography. Science of Remote Sensing 1, 100002. https://doi.org/10.1016/j.srs.2020.100002.
Dunn, O.J., 1964. Multiple comparisons using rank sums. Technometrics 6, 241–252. https://doi.org/10.1080/00401706.1964.10490181.
Everham, E.M., Brokaw, N.V.L., 1996. Forest damage and recovery from catastrophic wind. Bot. Rev. 62, 113–185. https://doi.org/10.1007/BF02857920.
Franczak, P., 2013. Influence of windstorms on change of landscape and land form; a case of the blowdown area of the southern slopes Polica Range(Beskid Żywiecki). Zarządzanie Ochroną Przyrody W Lasach 7, 273–285.
Gabet, E.J., Mudd, S.M., 2010. Bedrock erosion by root fracture and tree throw: a coupled biogeomorphic model to explore the humped soil production function and the persistence of hillslope soils. J. Geophys. Res. 115, F04005. https://doi.org/10.1029/2009JF001526.
Gabet, E.J., Reichman, O.J., Seabloom, E.W., 2003. The effects of bioturbation on soil processes and sediment transport. Annu. Rev. Earth Planet. Sci. 31, 249–273. https://doi.org/10.1146/annurev.earth.31.100901.141314.
Gallaway, J.M., Martin, Y.E., Johnson, E.A., 2009. Sediment transport due to tree root throw: integrating tree population dynamics, wildfire and geomorphic response. Earth Surf. Proc. Land. 34, 1255–1269. https://doi.org/10.1002/esp.1813.
Godziek, J., Pawlik, Ł., 2023. Indicators of wind-driven forest disturbances - pit-mound topography, its automatic detection and significance. Catena 221, 106757. https://doi.org/10.1016/j.catena.2022.106757.
Greenwood, P., Bauer, J., Kuhn, N.J., 2021. Assessing hillslope sediment generation potential by tree throw: a preliminary field study along a small river valley in the Jura Mountains, northwest Switzerland. Geographica Helvetica 76, 319–333. https://doi.org/10.5194/gh-76-319-2021.
Grodzki, W., Loch, J., Armatys, P., 2006. Occurrence of *Ips typographus* L. in wind-damaged Norway spruce stands of Kudłoń massif in the Gorce National Park. Ochrona Beskidów Zachodnich 1, 125–137.
Hansen, M.C., Potapov, P.V., Moore, R., Hancher, M., Turubanova, S.A., Tyukavina, A., Thau, D., Stehman, S.V., Goetz, S.J., Loveland, T.R., Kommareddy, A., Egorov, A., Chini, L., Justice, C.O., Townshend, J.R.G., 2013. High-resolution global maps of 21st-century forest cover change. Science 342, 850–853. https://doi.org/10.1126/science.1244693.
Heinaro, E., Tanhuanpää, T., Yrttimaa, T., Holopainen, M., Vastaranta, M., 2021. Airborne laser scanning reveals large tree trunks on forest floor. For. Ecol. Manage. 491, 119225 https://doi.org/10.1016/j.foreco.2021.119225.
Hijmans, R., 2023. terra: Spatial Data Analysis. R package version 1.7-18. Online: https://CRAN.R-project.org/package=terra.
Hollander, M., Wolfe, D.A., 1973. Nonparametric Statistical Methods. John Wiley & Sons, New York.
IMWM - NRI - Institute of Meteorology and Water Management - National Research Institute, 2023. Meteorological survey - archival data from automatic weather stations (telemetric system). Online, in Polish: https://dane.imgw.pl/datastore (dane archiwalne - dane meteorologiczne). doi: 10.1016/j.geomorph.2021.107749.
Jasiewicz, J., Stepinski, T.F., 2013. Geomorphons — a pattern recognition approach to classification and mapping of landforms. Geomorphology 182, 147–156. https://doi.org/10.1016/j.geomorph.2012.11.005.
Joyce, M.J., Erb, J.D., Sampson, B.A., Moen, R.A., 2019. Detection of coarse woody debris using airborne light detection and ranging (LiDAR). For. Ecol. Manage. 433, 678–689. https://doi.org/10.1016/j.foreco.2018.11.049.
Kooch, Y., Hosseini, S.M., Mohammadi, J., Hojjati, S., 2012. Effects of uprooting tree on herbaceous species diversity, woody species regeneration status and soil physical characteristics in a temperate mixed forest of Iran. J. For. Res. 23 https://doi.org/10.1007/s11676-012-0236-6.
Kooch, Y., Zaccone, C., Lamersdorf, N.P., Tonon, G., 2014. Pit and mound influence on soil features in an Oriental Beech (Fagus orientalis Lipsky) forest. Eur. J. Forestry ResearchJournal of Forestry Res. 133, 347–354. https://doi.org/10.1007/s10342-013-0766-2.
Kotarba, A., 1970. The morphogenetic role of foehn wind in the Tatra Mts. Studia Geomorphologica Carpatho-Balcanica 4, 171–188.
Kulakowski, D., Veblen, T.T., 2002. Influences of fire history and topography on the pattern of a severe wind blowdown in a Colorado subalpine forest. J. Ecol. 90, 806–819. https://doi.org/10.1046/j.1365-2745.2002.00722.x.
Liang, F., Du, Y., Ge, Y., Li, C., 2014. A quantitative morphometric comparison of cockpit and doline karst landforms. J. Geog. Sci. 24, 1069–1082. https://doi.org/10.1007/s11442-014-1139-6.
Lindberg, E., Hollaus, M., Mücke, W., Fransson, J.E.S., Pfeifer, N., 2013. Detection of lying tree stems from airborne laser scanning data using a line template matching algorithm. ISPRS Annals of the Photogrammetry, Remote Sensing and Spatial Information Sci. II-5/W2, 169–174. https://doi.org/10.5194/isprsannals-II-5-W2-169-2013.
Lisiewicz, M., Kamińska, A., Stereńczak, K., 2022. Influence of the correction method of CHM−based individual tree detection results on the estimation of forest stand characteristics. Sylwan 166, 362–377. https://doi.org/10.26202/sylwan.2022040.
Mann, H.B., Whitney, D.R., 1947. On a test of whether one of two random variables is stochastically larger than the other. Ann. Math. Stat. 18, 50–60.
Mauri, L., Tarolli, P., 2023. Modeling windthrow effects on water runoff and hillslope stability in a mountain catchment affected by the VAIA storm. Sci. Total Environ. 895, 164831 https://doi.org/10.1016/j.scitotenv.2023.164831.
Means, J.E., Acker, S.A., Harding, D.J., Blair, J.B., Lefsky, M.A., Cohen, W.B., Harmon, M.E., McKee, W.A., 1999. Use of large-footprint scanning airborne lidar to estimate forest stand characteristics in the western cascades of oregon. Remote Sens. Environ. 67, 298–308. https://doi.org/10.1016/S0034-4257(98)00091-1.
Mitchell, S.J., 2013. Wind as a natural disturbance agent in forests: a synthesis. Forestry 86, 147–157. https://doi.org/10.1093/forestry/cps058.
Mücke, W., Hollaus, M., Pfeifer, N., 2012. Identification of dead trees using small footprint full-waveform airborne laser scanning data. Proceedings of SilviLaser, Vancouver, BC, Canada.
Norman, S.A., Schaetzl, R.J., Small, T.W., 1995. Effects of slope angle on mass movement by tree uprooting. Geomorphology 14, 19–27. https://doi.org/10.1016/0169-555X(95)00016-X.
Nyström, M., Holmgren, J., Fransson, J.E.S., Olsson, H., 2014. Detection of windthrown trees using airborne laser scanning. Int. J. Appl. Earth Obs. Geoinf. 30, 21–29. https://doi.org/10.1016/j.jag.2014.01.012.
Obrębska-Starkel, B., Zaleski, T., Mazurek, R., 2004. Klimat Babiej Góry., in: Wołoszyn, B.W., Jaworski, A., Szwagrzyk, J. (Eds.), Babiogórski Park Narodowy. Monografa przyrodnicza. Komitet Ochrony Przyrody PAN, Babiogórski Park Narodowy, Kraków, pp. 137-151.
Patil, I., 2021. Visualizations with statistical details: the "ggstatsplot" approach. J. Open Source Softw. 6, 3167. https://doi.org/10.21105/joss.03167.
Pawlik, Ł., 2013. The role of trees in the geomorphic system of forested hillslopes — a review. Earth Sci. Rev. 126, 250–265. https://doi.org/10.1016/j.earscirev.2013.08.007.
Pawlik, Ł., Migoń, P., Owczarek, P., Kacprzak, A., 2013. Surface processes and interactions with forest vegetation on a steep mudstone slope, Stołowe Mountains, SW Poland. Catena 109, 203–216. https://doi.org/10.1016/j.catena.2013.03.011.
Pebesma, E., 2018. Simple features for R: standardized support for spatial vector data. R J. 10, 439. https://doi.org/10.32614/RJ-2018-009.
Pebesma, E., 2022. stars: Spatiotemporal Arrays, Raster and Vector Data Cubes. R package version 0.6-0. Online: https://CRAN.R-project.org/package=stars.
Phillips, J.D., Marion, D.A., Turkington, A.V., 2008. Pedologic and geomorphic impacts of a tornado blowdown event in a mixed pine-hardwood forest. Catena 75, 278–287. https://doi.org/10.1016/j.catena.2008.07.004.
Phillips, J.D., Šamonil, P., Pawlik, Ł., Trochta, J., Daněk, P., 2017. Domination of hillslope denudation by tree uprooting in an old-growth forest. Geomorphology 276, 27–36. https://doi.org/10.1016/j.geomorph.2016.10.006.
Pirotti, F., 2011. Analysis of full-waveform LiDAR data for forestry applications: a review of investigations and methods. Iforest - Biogeosciences and Forestry 4, 100. https://doi.org/10.3832/ifor0562-004.
Potapov, P.V., Turubanova, S.A., Tyukavina, A., Krylov, A.M., McCarty, J.L., Radeloff, V.C., Hansen, M.C., 2015. Eastern Europe's forest cover dynamics from 1985 to 2012 quantified from the full Landsat archive. Remote Sens. Environ. 159, 28–43. https://doi.org/10.1016/j.rse.2014.11.027.
Putz, F.E., 1983. Treefall pits and mounds, buried seeds, and the importance of soil disturbance to pioneer trees on Barro Colorado Island, Panama. Ecology 64, 1069–1074. https://doi.org/10.2307/1937815.
R Core Team, 2023. R: A language and environment for statistical computing. R Foundation for Statistical Computing, Vienna, Austria. Online: https://www.R-project.org/.
Reid, L.M., 1981. Sediment production from gravel-surfaced forest roads, Clearwater Basin, Washington. Publication FRI-UW-8180. University of Washington, Fisheries Research Institute, Seattle, Washington, USA.
Richards, P.J., Hohenthal, J.M., Humphreys, G.S., 2011. Bioturbation on a south-east Australian hillslope: estimating contributions to soil flux. Earth Surf. Proc. Land. 36, 1240–1253. https://doi.org/10.1002/esp.2149.
Rojan, E., 2012. Pit-and-mound microrelief in the windthrow area in the Slovak High Tatras. Prace i Studia Geograficzne 49, 173–183.
Roussel, J.-R., Auty, D., Coops, N.C., Tompalski, P., Goodbody, T.R.H., Meador, A.S., Bourdon, J.-F., de Boissieu, F., Achim, A., 2020. lidR: An R package for analysis of Airborne Laser Scanning (ALS) data. Remote Sens. Environ. 251, 112061 https://doi.org/10.1016/j.rse.2020.112061.
RStudio Team, 2021. RStudio: Integrated Development Environment for R. RStudio, PBC, Boston, MA. Online: http://www.rstudio.com/.
Šamonil, P., Král, K., Hort, L., 2010a. The role of tree uprooting in soil formation: a critical literature review. Geoderma 157, 65–79. https://doi.org/10.1016/j.geoderma.2010.03.018.
Šamonil, P., Tejnecký, V., Borůvka, L., Šebková, B., Janík, D., Šebek, O., 2010b. The role of tree uprooting in Cambisol development. Geoderma 159, 83–98. https://doi.org/10.1016/j.geoderma.2010.06.020.
Šamonil, P., Daněk, P., Schaetzl, R.J., Vašíčková, I., Valtera, M., 2015. Soil mixing and genesis as affected by tree uprooting in three temperate forests. Eur. J. Soil Sci. 66, 589–603. https://doi.org/10.1111/ejss.12245.
Šamonil, P., Valtera, M., Schaetzl, R.J., Adam, D., Vašíčková, I., Daněk, P., Janík, D., Tejnecký, V., 2016. Impacts of old, comparatively stable, treethrow microtopography on soils and forest dynamics in the northern hardwoods of Michigan, USA. Catena 140, 55–65. https://doi.org/10.1016/j.catena.2016.01.006.

Schaetzl, R.J., Burns, S.F., Small, T.W., Johnson, D.L., 1990. Tree uprooting: review of types and patterns of soil disturbance. Phys. Geogr. 11, 277–291. https://doi.org/10.1080/02723646.1990.10642407.

Schaetzl, R.J., Follmer, L.R., 1990. Longevity of treethrow microtopography: implications for mass wasting. Geomorphology 3, 113–123. https://doi.org/10.1016/0169-555X(90)90040-W.

Schaetzl, R.J., Johnson, D.L., Burns, S.F., Small, T.W., 1989. Tree uprooting: review of terminology, process, and environmental implications. J. For. Res. https://doi.org/10.1139/x89-001.

Strzyżowski, D., 2019. The role of topography, canopy gaps, and forest edges in the distribution of windthrow damage in the Western Tatra Mountains, Poland. Geogr. Pol. 92, 173–187. https://doi.org/10.7163/GPol.0143.

Strzyżowski, D., Fidelus, J., Żelazny, M., 2016. Geomorphological changes within a hillslope caused by a windthrow event in the Tatra Mountains, southern Poland. Geogr. Ann. Ser. B 98, 347–360. https://doi.org/10.1111/geoa.12141.

Strzyżowski, D., Fidelus-Orzechowska, J., Żelazny, M., 2018. Sediment transport by uprooting in the forested part of the Tatra Mountains, southern Poland. Catena 160, 329–338. https://doi.org/10.1016/j.catena.2017.09.019.

Strzyżowski, D., Gorczyca, E., Krzemień, K., Żelazny, M., 2021. The intensity of slope and fluvial processes after a catastrophic windthrow event in small catchments in the Tatra Mountains. J. Mt. Sci. 18, 1405–1423. https://doi.org/10.1007/s11629-021-6726-2.

Taylor, A.R., Dracup, E., MacLean, D.A., Boulanger, Y., Endicott, S., 2019. Forest structure more important than topography in determining windthrow during Hurricane Juan in Canada's Acadian Forest. For. Ecol. Manage. 434, 255–263. https://doi.org/10.1016/j.foreco.2018.12.026.

Tjoelker, M.G., Boratynski, A., Bugała, W., 2007. Biology and Ecology of Norway Spruce. Springer Science & Business Media.

Ulanova, N.G., 2000. The effects of windthrow on forests at different spatial scales: a review. For. Ecol. Manage. 135.

Wickham, H., François, R., Henry, L., Müller, K., Vaughan, D., 2023. _dplyr: a Grammar of Data Manipulation_. R Package Version 1 (1), 2. Online https://CRAN.R-project.org/package=dplyr.

Wu, Q., Liu, H., Wang, S., Yu, B., Beck, R., Hinkel, K., 2015. A localized contour tree method for deriving geometric and topological properties of complex surface depressions based on high-resolution topographical data. Int. J. Geogr. Inf. Sci. 29, 2041–2060. https://doi.org/10.1080/13658816.2015.1038719.

Zadrożny, P., Krużel, J., Lamorski, T., Nicia, P., Kozina, P., 2017. Changes of the monitoring windfallen area on the Babia Góra Mountain. J. Ecol. Eng. 18, 193–199. https://doi.org/10.12911/22998993/67097.

Zhang, K., Chen, S.-C., Whitman, D., Shyu, M.-L., Yan, J., Zhang, C., 2003. A progressive morphological filter for removing nonground measurements from airborne LIDAR data. IEEE Trans. Geosci. Remote Sens. 41, 872–882. https://doi.org/10.1109/TGRS.2003.810682.

Catena 221 (2023) 106757

Contents lists available at ScienceDirect

Catena

journal homepage: www.elsevier.com/locate/catena

Indicators of wind-driven forest disturbances – pit–mound topography, its automatic detection and significance

Janusz Godziek [a,b,*], Łukasz Pawlik [a]

[a] University of Silesia, Faculty of Natural Sciences, Institute of Earth Sciences, ul. Będzińska, 60, 41-200 Sosnowiec, Poland
[b] University of Silesia, International Environmental Doctoral School, ul. Będzińska, 60, 41-200 Sosnowiec, Poland

ARTICLE INFO

Keywords:
pit–mound topography
LiDAR
digital elevation model
geomorphometry
R programming
Polish Carpathians

ABSTRACT

Pit-and-mound topography is a result of tree uprooting caused by hurricane-force wind events and hence can act as a bioindicator of forest disturbance. The occurrence and evolution of pit–mound topography can be analyzed using detailed elevation data, such as point clouds from Light Detection and Ranging (LiDAR) surveys. The objective of this study was to develop an automatic method of pit–mound topography detection. We propose the usage of closed contour lines to extract the locations of pits and mounds. We performed analyses in two study areas (*Markowa* and *Stonów*) located on the Babia Góra Massif (southern Poland). We computed the digital elevation model (DEM), extracted contour lines, calculated the length of each contour line and selected only closed contours belonging to a specified length interval. Then, we created polygons from the outermost closed contour lines. We classified polygons into "pits" and "mounds" by investigating the location of the highest and lowest altitudes within the polygon. We tested 27 variants of our method using different DEM spatial resolutions, contour intervals and contour length intervals. To estimate the accuracy of our method, we created a validation dataset by performing manual recognition of pit–mound pairs based on the topographic position index (TPI). One of the highest accuracies, obtained for the 1st variant of our method, reached 96.9 % for pits, 93.8 % for mounds and 90.6 % for pit–mound pairs in the *Stonów* area. In the *Markowa* area, this variant achieved an accuracy of 95.2 % for pits, 90.5 % for mounds and 85.7 % for pit–mound pairs. Our method can be used as an important step in analyses conducted in forest ecology, geomorphology or soil science.

1. Introduction

Living organisms act as geomorphic and pedogenic agents and impact the evolution of hillslope relief and soils (Schaetzl et al., 1990; Gabet et al., 2014; Ocko et al., 2019; Meng et al., 2022). In forest ecosystems, tree uprooting, caused by hurricane wind events or ice storms, is the most widespread process. Combined with subsequent erosion of the displaced soil material, this process leads to the formation of the so-called pit-and-mound topography (Ulanova, 2000; Šamonil et al., 2010a, 2010b; Pawlik et al., 2013). This unique type of microrelief occurs all over the world in tropical, subtropical and temperate forests (Putz, 1983; Jane, 1986; Clinton and Baker, 2000; Kooch et al., 2014) and is a clear bioindicator of forest dynamics related to climate events (Schaetzl et al., 1989; Hellmer et al., 2015; Pawlik et al., 2016).

To date, studies on pit–mound topography have attempted to investigate the following issues: 1) storage of nutrients in soils under old-growth forests (Liechty et al., 1997), 2) species composition of understory vegetation in forests (Kooch et al., 2012), 3) tree stand dynamics in old-growth forests (Ulanova, 2000; Šamonil et al., 2009), 4) pedoturbations and pedogenesis under the repeated impact of the tree-throw process (Phillips et al., 2008; Šamonil et al., 2016; Pawlik et al., 2017), 5) detection and radiocarbon dating of pit–mound forms (Embleton-Hamann, 2004; Šamonil et al., 2013), 6) application of geophysical methods to investigate the internal structure and properties of tree-throw pits and mounds (Pawlik and Kasprzak, 2015, Pawlik and Kasprzak, 2018), and 7) biotransport (Gabet et al., 2003; Gallaway et al., 2009; Pawlik et al., 2013; Doane et al., 2021). In addition, pit–mound topography has been analyzed in terms of water retention and hydrologic modeling (Valtera and Schaetzl, 2017), as well as soil erosion and biotransport (Gabet et al., 2003; Gallaway et al., 2009; Constantine et al., 2012; Pawlik et al., 2016; Strzyżowski et al., 2018). Barker Plotkin et al. (2017) compared the formation of pit–mound topography between old-growth and second-growth forests and pointed out the possible influence of humans on the formation of this type of relief. Other studies

* Corresponding author at: University of Silesia, Faculty of Natural Sciences, Institute of Earth Sciences, ul. Będzińska, 60, 41-200 Sosnowiec, Poland.
E-mail address: janusz.godziek@us.edu.pl (J. Godziek).

https://doi.org/10.1016/j.catena.2022.106757
Received 6 June 2022; Received in revised form 15 October 2022; Accepted 3 November 2022
Available online 13 November 2022

have investigated relict pit–mound topography preserved in mountain meadows (so-called hummocky meadows) (Embleton-Hamann, 2004; Pawlik et al., 2019).

In recent years, the availability of detailed elevation data (especially Light Detection and Ranging (LiDAR) surveys) has significantly increased. Such data are very often used for the detection of different types of microrelief forms, particularly of anthropogenic origin, such as pitfall traps (Trier and Pilø, 2012), cache pits (Cody and Anderson, 2021), burial mounds (Freeland et al., 2016; Niculiță, 2020), charcoal kilns (Rutkiewicz et al., 2017), and agricultural terraces (Tarolli et al., 2015). LiDAR data are also applied to detect microrelief forms produced by biotic factors, such as termite and ant mounds (D'hont et al., 2021) and mima mounds (Gabet et al., 2014). Many authors have tended to propose methods of automatic detection of microrelief forms (Trier and Pilø, 2012; Freeland et al., 2016; Davis et al., 2019a). Automation have numerous advantages over manual, "on-screen" data analysis. Automatic methods are much more objective (Trier and Pilø, 2012) and can be applied to the examination of large areas (Meyer et al., 2019; Trier et al., 2019). In addition, such methods allow us to determine the location of many previously undetected forms, which can significantly accelerate the scope of their inventory (Riley, 2009; Schneider et al., 2015; Freeland et al., 2016). However, automatic detection methods are characterized by certain inaccuracies. Therefore, various techniques for accuracy assessment are used (Howey et al., 2016; Niculiță, 2020) or an estimated probability of the occurrence of a given form is presented (Guyot et al., 2018; Davis et al., 2019b).

Most past research has focused on detecting forms of anthropogenic origin. Because of the more regular shapes of such forms, their detection seems to be easier in comparison with mapping the forms of biotic origin, which frequently have irregular shapes. Only a few studies have looked at the usage of LiDAR data application in research on pit–mound topography. Doane et al. (2021) attempted to quantify hillslope sediment flux caused by tree throw with the use of a digital elevation model (DEM) produced on the basis of a LiDAR survey. For quantification, they needed to build a model of a typical pit–mound pair based on forms mapped on a 1 km^2 plot of land. However, their overall analysis was focused on slope-scale estimations, and they did not extract precise locations of pit–mound pairs through the application of any dedicated method.

The consideration of the detection of pit–mound topography is important for several reasons. First, this topography is a direct bioindicator of the past forest disturbances that were caused by strong wind events or ice storms (Schaetzl et al., 1989; Hellmer et al., 2015). Wind is the most common factor of tree uprooting and breakage in temperate forest zones (Schelhaas et al., 2003; Šamonil et al., 2009). If detected, the topography can serve as proxy data on past forest and hillslope dynamics. Second, this type of topography is evidence of past pedoturbations that can have a key meaning in soil development and influence its physical and chemical properties. For instance, soil profile upbuilding is evident within tree-throw mounds. In addition, organic matter accumulation and stronger leaching are frequently observed soil profile properties within tree-throw pits (Šamonil et al., 2010a, 2010b; Pawlik et al., 2013).

LiDAR data analysis offers significant opportunities in terms of the extraction of various types of information from digital elevation models (Freeland et al., 2016; Niculiță, 2020). This may include precise information on the position and geomorphometric parameters of pit–mound pairs. High-resolution DEMs can be used to study the spatial extent and stage of development and degradation (denudation) of pit–mound topography. Such research can expand our knowledge of the magnitude of wind effects on forest floor microrelief changes caused by the tree uprooting process. In addition, such knowledge would be crucial for research on forest ecosystem dynamics (disturbances and regeneration). Measuring different morphometric parameters of particular forms might be applied to assess the stage of their development. Modern tools (e.g., R programming language) can be used to automate DEM analysis. This can help to examine large areas in terms of pit–mound topography occurrence and the level of its development.

The objective of this study is to develop an automatic unsupervised method of pit–mound topography detection. First, we describe in detail the proposed contour method (CM). Second, we show how the proposed method was optimized and validated using reference data. Third, we explore the spatial patterns of the detected probable locations of pit–mound pairs and compare them against terrain morphometric properties. Fourth, we show ways of potential application of the method and pit–mound topography significance from the viewpoint of geomorphology and forest ecology. We investigated two study areas located on the Babia Góra Massif (southern Poland). Analyses are based on DEMs produced from publicly accessible LiDAR data (Geoportal, 2022).

2. Background

There are various microforms of biological activity, including earthworm casts, which can be up to several centimeters high (Darwin, 1881), and spectacular termite mounds, which can reach a height of 2–3 m (Davies et al., 2014). Tree-throw pit–mound forms are among the most complex surficial forms that originate from the disturbance (uprooting) of living or dead trees. Tree uprooting can be a result of wind impacts or ice storms (Schaetzl et al., 1989; Pawlik, 2013; Hellmer et al., 2015). Such forms typically consist of two components: 1) pits (places occupied by tree-root systems before uprooting) and 2) mounds, which are a result of root-plate degradation and root wood decomposition of uprooted trees. Tree root-plate degradation and mound formation can take several years, and their rate is mainly related to climate, soil conditions, and root-plate volume (soil volume + root volume) (Fig. 1S, Supplementary Materials). For instance, the rate of root-plate degradation in Michigan, USA, was estimated at 5–10 years (Schaetzl and Follmer, 1990), whereas in the flysch zone of the Czech Republic, it was 50–60 years (Šamonil et al., 2009). Both forms add to the complexity of the hillslope topography (roughness, surface wash connectivity and continuity) that greatly impact geomorphic activity (transport, erosion) and soil processes (Pawlik et al., 2016; Šamonil et al., 2010a). Their spatial density can be up to 1200 forms per ha (Lyford, 1966), and their age can reach even 6000 years (Šamonil et al., 2013). Tree-throw pit–mound pairs can pose a problem during any attempt at their recognition in very high-resolution LiDAR-based DTMs. However, there are several clues that can help to detect such forms: 1. adjacent position of tree-throw pits and mounds because they are a result of the same event acting upon a single tree; 2. on steeper hillslopes, mounds tend to form downslope of adjacent pits; 3. mounds are not higher than 0.5–2 m, and pits are not deeper than 0.5–2 m; and 4. pits are places of water accumulation that can be visible in models of the topographic wetness index (TWI). On the other hand, in recent decades, researchers have reported a wide range of various pit–mound forms that are hard to generalize, and their correct recognition can only be realized during detailed fieldwork surveys (mapping and excavation). Existing estimations of root plates mean volumes range from 0.1 in British Columbia (Gallaway et al., 2009) to 4.0 m^3 in the Sudety Mountains, Poland (Pawlik et al., 2016). However, the mean volume of tree-throw mounds can reach 3.0 m^3 in forests of Mazandaran Province, Iran (Kooch et al., 2012).

3. Materials and methods

3.1. Study area

For a detailed study, we selected two areas: *Markowa* and *Stonów* (Fig. 1). They are located close to each other at the northern foot of the Babia Góra Massif (1725 m a.s.l., Polish Western Carpathians). Their areas are 62.5 and 44.9 ha for *Markowa* and *Stonów,* respectively. The altitudes of the examined areas vary between 779 and 911 m a.s.l. for *Markowa* and between 799 and 905 m a.s.l. for *Stonów*. Both areas are

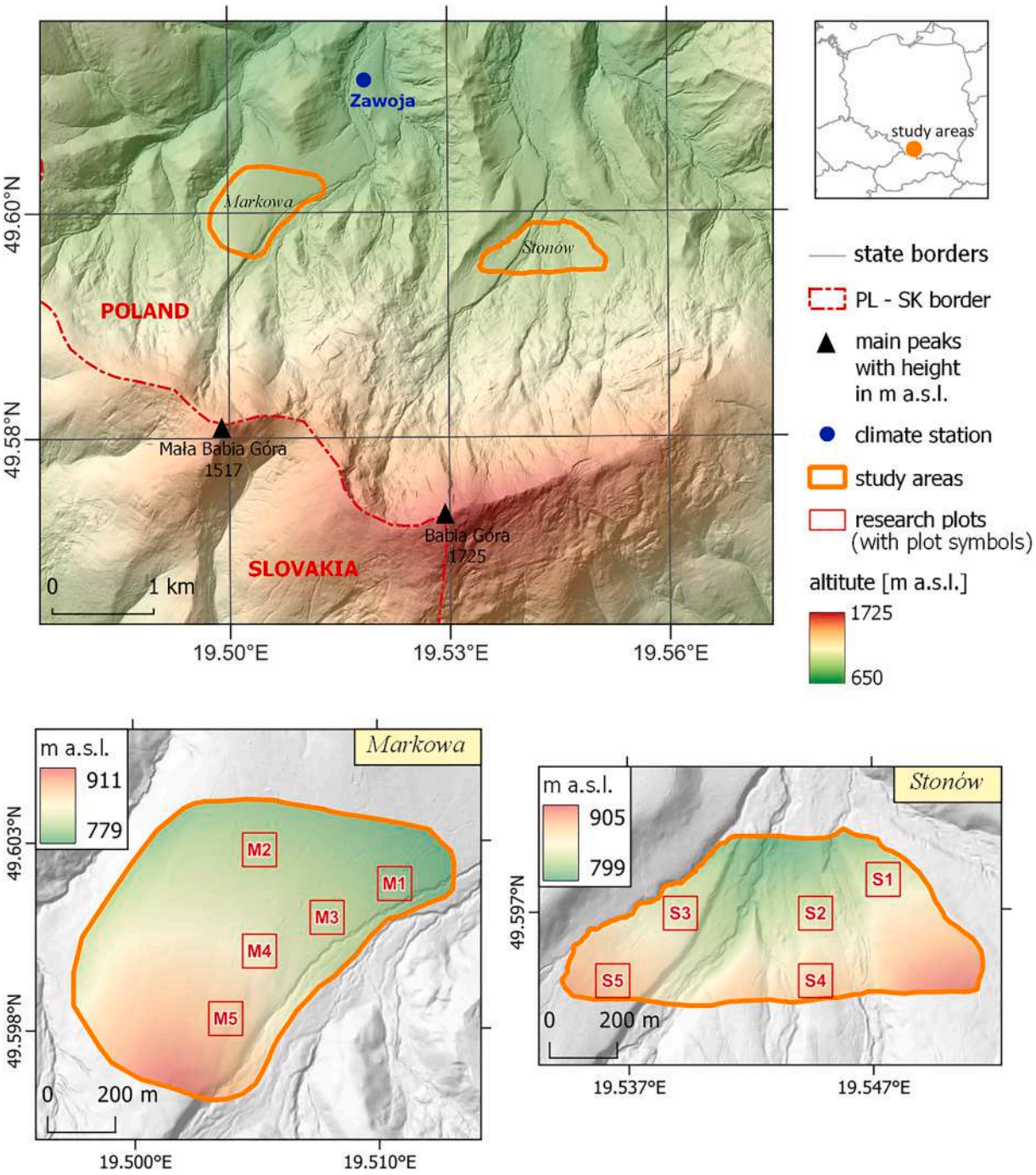

Fig. 1. Two study sites (*Markowa* and *Stonów*) and their locations within the Babia Góra Massif (1725 m a.s.l., Polish Western Carpathians).

gently sloped, with a predominance with a northern aspect. Hillslopes are incised by a few stream valleys in a S-N direction. The bedrock is composed of alternating layers of shales and sandstones forming flysch. Major parts of both areas are occupied by Quaternary sands and gravels of presumed fluvial origin (Książkiewicz, 1971; Detailed Geological Map of Poland, 2019).

The Babia Góra Massif is characterized by a moderate warm transitional climate, with a strong altitude impact. The northern foot of the massif is located in a moderate warm zone, with a mean annual temperature of approximately 6 °C (Wypych et al., 2018). For the *Zawoja* climate station, located ca. 1 km from the *Markowa* study area (19.51866°E, 49.61176°N), the mean annual temperature in the 1961–2018 period reached 6.4 °C, and the mean annual precipitation during the same period was 1228.7 mm (IMWM – NRI, 2022). The Babia Góra Massif is the highest part of the Western Beskidy Mountains, with no mountains of similar height within a few dozen kilometers. Therefore, the massif forms a significant natural barrier against flowing air masses and is a region of frequent strong wind activity. The predominant wind directions measured in Zawoja include S and SW (Trepińska and Kowanetz, 2000). The vegetation of the massif includes mixed forests, coniferous forests, dwarf pine scrub and alpine meadows. Both study areas are overgrown by mixed, beech-fir forest, with an admixture of spruce. Since 1954, a major part of the massif has been protected by Babia Góra National Park (BgNP; Holeksa and Woźniak, 2005). The forest in the *Markowa* area was probably damaged by hurricane-force wind in 1926 or 1936 (Lamorski, person. comm.). We do not know

about a similar event that disturbed the *Stonów* area. Trees in this area are much older than those in the *Markowa* area, i.e., Norway spruces are 130 years old, and beeches are 120 years old. In the *Markowa* area, young generations of Norway spruce (30 years old) and silver fir (55 years old) dominate (Forest survey, 2021).

3.2. LiDAR data processing and DEM analysis

Detailed elevation data were obtained from an airborne LiDAR (Light Detection and Ranging) survey carried out by the Polish Institute of Geodesy and Cartography. These public data can be freely downloaded from the Polish *Geoportal* website (Geoportal, 2022). Each tile has an area of ca. 1.3 km^2 and includes ca. 81–104 MB of data. The XY-data of each point were measured in a flat rectangular Polish Coordinate System 1992 (EPSG: 2180). Altitudes refer to the "Kronsztadt" normal height system (PL-KRON86-NH). The vertical accuracy of the data reaches $\leq$ 0.15 m, and the position accuracy is $\leq$ 0.5 m. The point cloud density is at least 4 points per m^2. The ratio of the average distance of the laser dots in the direction of flight and in the transverse direction ranges from 1:1.5 to 1.5:1. The incidence angle was $\leq \pm 25°$, and the spot diameter of the laser beam on the surface of the terrain was $\leq$ 0.5 m. The transverse coverage between rows was in a range of 20–30 %. Point cloud data were divided into 12 classes in accordance with the ASPRS standard (Wężyk, 2015). For the area of interest, LiDAR data were acquired in November 2012 and November 2014. We worked on 4 tiles of point cloud data (2 for each study area).

The point cloud was processed in the R environment using the *lidR* package (Roussel et al., 2020). Duplicated points were filtered. We used points classified as "ground" or "water" (classes 2 and 9, respectively) to compute three DEMs with resolutions of 0.5, 0.25 and 0.1 m. We applied the k-nearest neighbor algorithm (KNN) with inverse distance weighting (IDW). The number of nearest neighbors was set to 10, and the power of IDW was 2. For detailed DEM analysis, we computed several DEM derivatives, such as slope, aspect, wind exposition index (WEI), topographic wetness index (TWI) and topographic ruggedness index (TRI). The WEI provides information about terrain exposure to potential airflow, where places with WEI < 1 are shadowed from the potential influence of airflow, and places with WEI > 1 are exposed to wind impact. The TWI is a dimensionless index that describes the potential surface water flow and accumulation (Moore et al. 1991). The TRI expresses elevation differences between adjacent cells of a DEM (Riley et al., 1999). All three indices are potentially highly useful in ecological and geomorphic modeling (Dyderski and Pawlik 2021; Pawlik and Harrison 2022).

3.3. Validation data – "On screen" recognition of pits and mounds

We applied the topographic position index (TPI) to perform "manual" recognition of pit-and-mound pairs. The TPI is a very valuable tool for relief classification. This index is computed by obtaining the difference between the elevation of a given raster cell and the mean elevation within the predefined surroundings of that cell. In most cases, this surrounding is defined as a circle or as a square (De Reu et al., 2013). Positive values of the TPI indicate the presence of convex forms, while negative values are related to concave forms. Values near 0 are characteristic of flat areas or slopes with uniform gradients. The size of the moving circle or square used for TPI computation is strongly related to the size of landforms that we want to recognize. A larger moving window should be applied in main ridge and valley identification, while a smaller window size would be appropriate for microtopographic investigations. The minimal size of detectable forms is limited mainly by the DEM resolution (Skentos, 2017).

In each study area (*Markowa* and *Stonów*), we delineated 5 square-shaped research plots (Fig. 1). Plot locations were randomly selected. We used the criterion of not choosing adjacent plots. Each plot occupied an area of 1 ha. We assumed that the analysis of 5 such plots for each study area would be representative and reliable. For the research plots, we conducted "on-screen" recognition of pit-and-mound pairs. The analysis was based on DEM-derived data, such as the 1) TPI and 2) contour lines. We marked only pit–mound pairs with 1) negative TPI values for the pit, 2) positive TPI values for the mound and 3) a characteristic fit of contour lines for both forms (pit-mound) at the same time that assured us these forms originated from the tree uprooting process (Fig. 2). As auxiliary layers, we also used WEI, TRI and slope.

Raster data were calculated on the basis of a DEM with a 0.5 m resolution. Contour lines were generated with an interval of 0.1 m on the basis of a DEM with a 0.25 m resolution. The TPI was calculated in the *spatialEco* R package (Evans, 2021). We took the *scale* argument equal to 7, which corresponds to a moving 3.5 m-sided square for the DEM with a 0.5 m resolution.

3.4. Detection – Contour method (CM)

Tree-throw pits and mounds very often represent distinct concave or convex forms, clearly recognizable at the microtopographic scale. Therefore, such forms influence the shape of the contour lines, especially if the contour line interval is small. It seems that in many cases, the contour lines close at local microscale elevations and depressions even though at the hillslope scale they should continue as almost straight lines (Fig. 2, Fig. 3). Extraction of such lines can make it possible to determine the exact location of the forms.

These forms can be classified as pits or mounds based on an examination of values of terrain elevation a.s.l. (represented in the DEM) inside the closed contour line. In most cases, the direct proximity of pit-and-mound forms can be considered a premise for inferring the wind-thrown genesis of these forms. Analysis of the distance between the closest pits and mounds may allow effective recognition of pit-and-mound pairs. These assumptions are the basis of the contour method (CM) proposed in this study. An overview of the general workflow of this method is presented in Fig. 4.

We created contour lines on the basis of the DEM and calculated the length of each contour line. Then, we selected only contour lines belonging to the specified contour line length interval. Maximum and minimum threshold values were adopted from the literature (Phillips et al., 2008; Šamonil et al., 2010a; Pawlik, 2013;) but were also based on the authors' experience. Tree-throw pits and mounds are limited by the size of root-plates of uprooted trees and subsequent processes that deteriorate root-plates and material filling pits. The next step was to extract polygons representing the outermost closed contour lines. For this purpose, we performed several spatial operations on closed contour lines, such as 1) conversion to polygons, 2) union and dissolve to exclude overlapping features, and 3) simplification and smoothing of polygons.

The next stage of the analysis was to classify polygons into pits and mounds. We conducted classification on the basis of the location of the highest and lowest elevations a.s.l. within each polygon. For each polygon, we computed the distance between the location of the highest elevation and the polygon boundary (*dist_H*) and between the location of the lowest elevation and the polygon boundary (*dist_L*). Then, we calculated *diff_HL*– the absolute value of the difference between *dist_H* and *dist_L*. All polygons with *diff_HL* lower than 0.1 m were labeled "unclassified" and excluded from the analysis. The remaining polygons were divided into "pit" and "mound" classes based on the difference between *dist_H* and *dist_L*. If *dist_L* was greater than *dist_H*, then the polygon was labeled "pit" class. Otherwise, it was assigned to the "mound" class (Fig. 5). Finally, classified polygon data were converted to a raster with a spatial resolution of 0.5 m. Features of class "pit" were assigned the value "-1", while features of class "mound" were assigned the value "1". Pixels located outside the polygons obtained a value of 0.

3.5. Statistical analyses and testing

The analysis procedure described above was repeated for different 1)

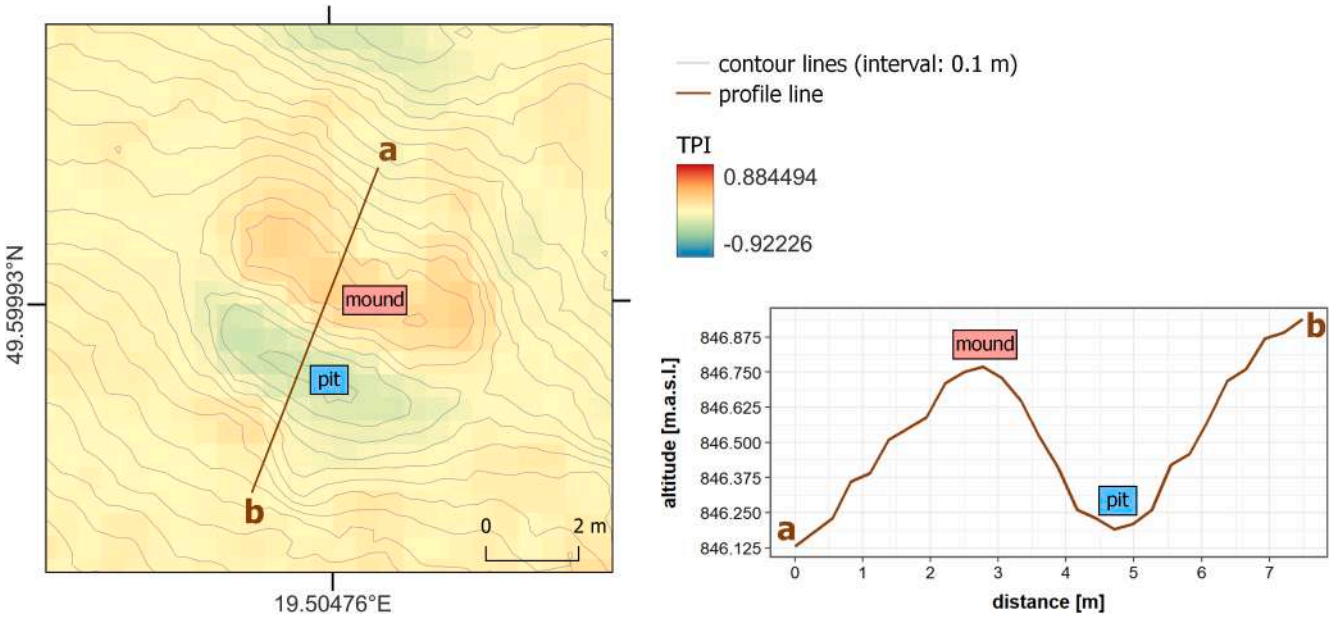

Fig. 2. A template pit–mound pair – map with topographic position index (TPI) and cross-section. This kind of form was marked during "on-screen" recognition.

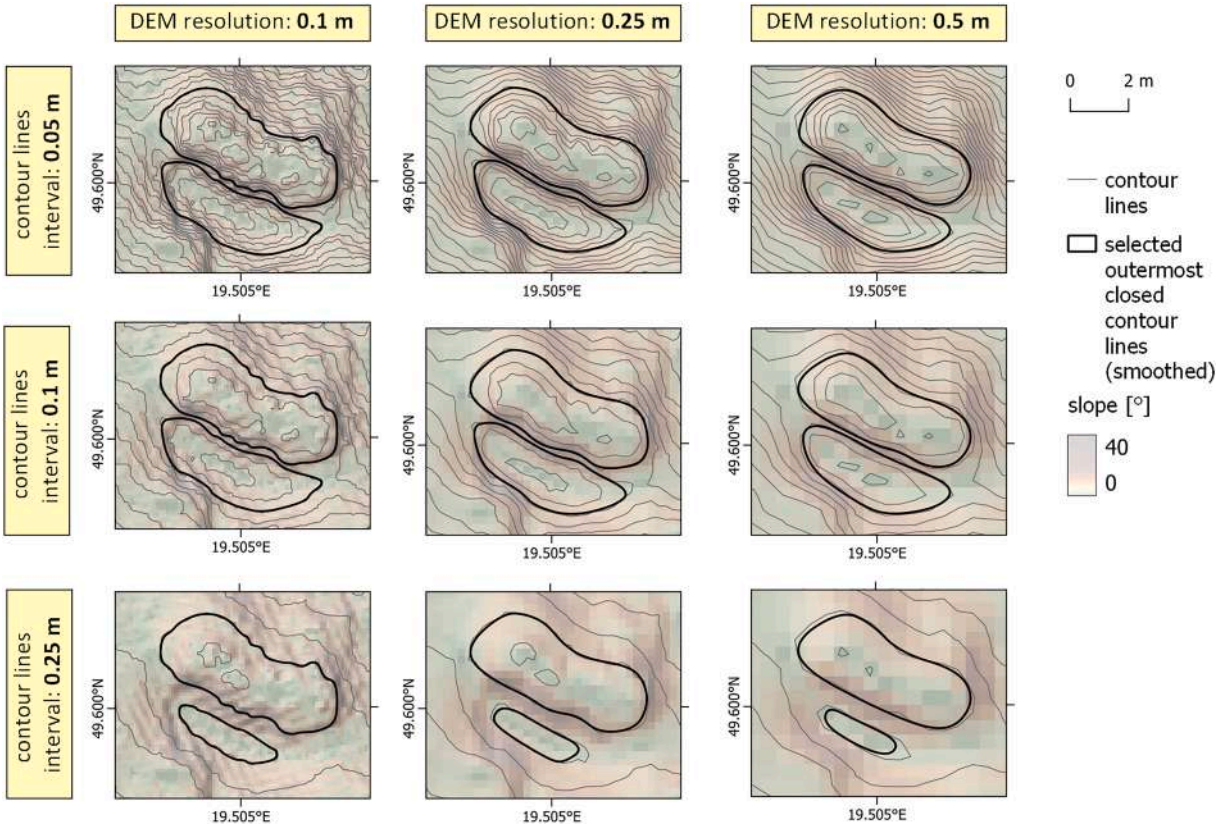

Fig. 3. Maps showing the template pit–mound pair depending on the resolution of the DEM and contour line intervals.

spatial resolutions of the DEM (0.5, 0.25 and 0.1 m), 2) contour line intervals (0.25, 0.1 and 0.05 m) and 3) contour line length intervals (1.5–25 m, 2.5–20 m and 3.5–15 m). We tested 27 variants of the abovementioned variables (Table 1). As an output, we derived 27 raster layers with pixels assigned to classes: "pit" (−1), "mound" (1) and "other areas" (0). The next step was to evaluate the compatibility of the resulting raster layers with the point validation data. For each point location, we sampled 27 raster layers and assigned their values to the attribute table. For each applied variant of the contour method (CM), we counted the number of correctly and incorrectly recognized pits. A similar analysis was conducted for mounds. We also counted the number of properly identified pit–mound pairs. Some pit–mound pairs were "partially detected", i.e., only pits or only mounds were detected. The analysis described above allowed us to calculate the accuracy of the CM. We assumed this accuracy as the percentage share of correctly detected forms (i.e., pits, mounds or pit–mound pairs).

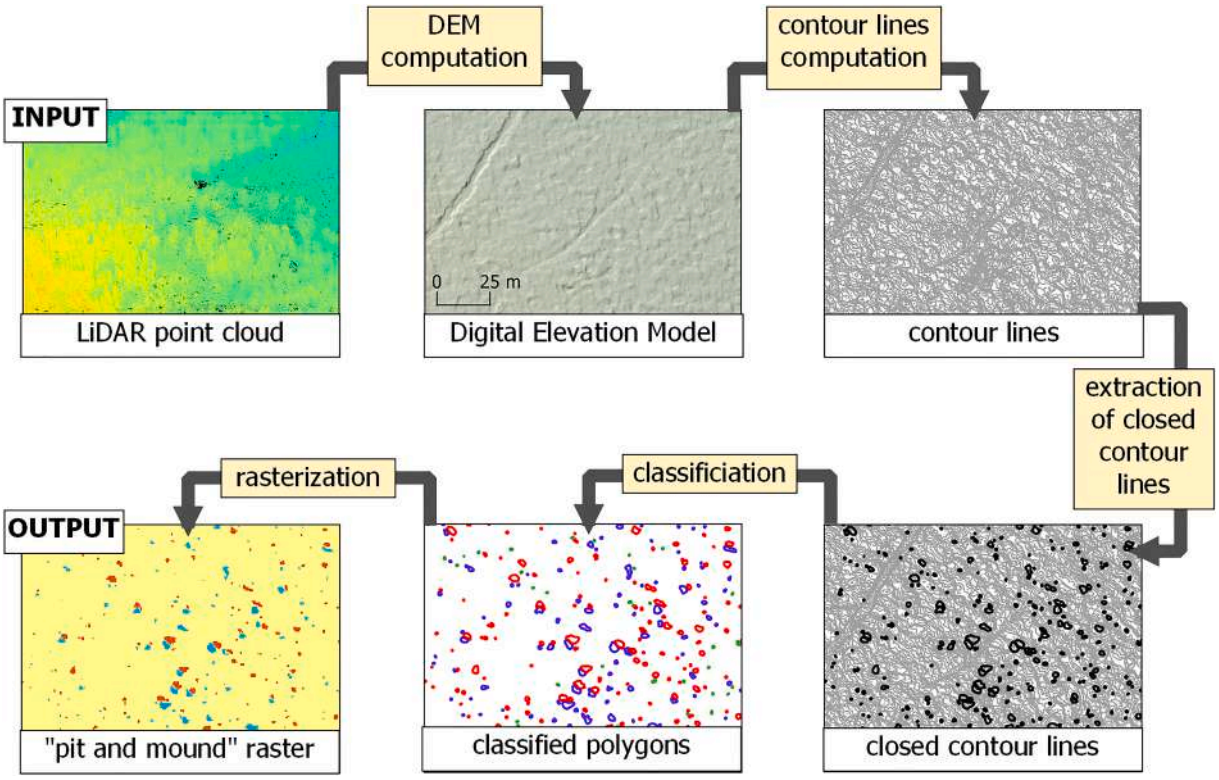

Fig. 4. Pit-and-mound detection – general workflow of the contour method (CM).

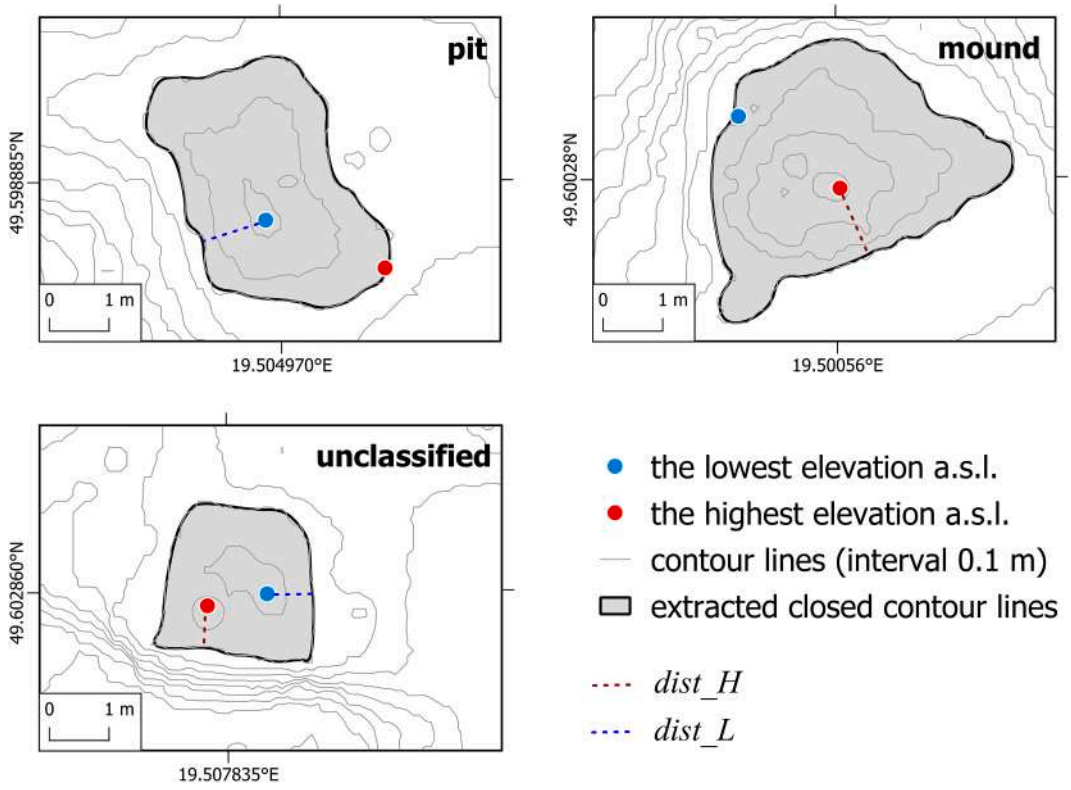

Fig. 5. The rules of the pit-and-mound classification applied in the contour method (CM).

We performed further analysis for the 1st variant of the CM. We converted the raster data to two vector layers (with pits and with mounds). Then, for each pit, we computed the distance to the nearest mound, and for each mound, we computed the distance to the nearest pit. We selected only adjacent forms by setting the maximal threshold distance between pit and mound to 1.5 m. In the next step, we filtered

Table 1
The percentage share of correctly detected (green), undetected (orange), misrecognized (yellow) and partially detected (blue) forms for each of the 27 tested variants (gray) of the contour method (CM). The share was calculated by comparing the output of each variant with the validation dataset (n = 42 for the *Markowa* area and 32 for the *Stonów* area) derived from the "on-screen" analysis of the TPI. In both study areas, assessments were conducted separately for 1) pit–mound pairs, 2) mounds, and 3) pits.

Variant number	Variant variables				Markowa (n = 42)									Stonów (n = 32)								
					Pit-mound pairs			Mound			Pit			Pit-mound pairs			Mound			Pit		
	DEM resolution	Contour lines interval	Minimal length of contour lines	Maximal length of contour lines	Detected [%]	Partially detected [%]	Undetected [%]	Detected [%]	Undetected [%]	Misrecognized [%]	Detected [%]	Undetected [%]	Misrecognized [%]	Detected [%]	Partially detected [%]	Undetected [%]	Detected [%]	Undetected [%]	Misrecognized [%]	Detected [%]	Undetected [%]	Misrecognized [%]
1	0.10	0.05	1.5	25.0	85.7	14.3	0.0	90.5	9.5	0.0	95.2	4.8	0.0	90.6	9.4	0.0	93.8	6.3	0.0	96.9	3.1	0.0
2	0.10	0.05	2.5	20.0	83.3	16.7	0.0	88.1	11.9	0.0	95.2	4.8	0.0	93.8	6.3	0.0	96.9	3.1	0.0	96.9	3.1	0.0
3	0.10	0.05	3.5	15.0	81.0	19.0	0.0	85.7	14.3	0.0	95.2	4.8	0.0	90.6	9.4	0.0	96.9	3.1	0.0	93.8	6.3	0.0
4	0.10	0.10	1.5	25.0	69.0	26.2	4.8	66.7	23.8	9.5	69.0	11.9	19.0	90.6	9.4	0.0	93.8	6.3	0.0	96.9	3.1	0.0
5	0.10	0.10	2.5	20.0	71.4	28.6	0.0	81.0	19.0	0.0	90.5	9.5	0.0	93.8	6.3	0.0	96.9	3.1	0.0	96.9	3.1	0.0
6	0.10	0.10	3.5	15.0	69.0	28.6	2.4	78.6	21.4	0.0	88.1	11.9	0.0	87.5	12.5	0.0	93.8	6.3	0.0	93.8	6.3	0.0
7	0.10	0.25	1.5	25.0	21.4	52.4	26.2	57.1	42.9	0.0	38.1	61.9	0.0	28.1	46.9	25.0	56.3	43.8	0.0	46.9	53.1	0.0
8	0.10	0.25	2.5	20.0	21.4	52.4	26.2	57.1	42.9	0.0	38.1	61.9	0.0	28.1	46.9	25.0	43.8	43.8	12.5	34.4	53.1	12.5
9	0.10	0.25	3.5	15.0	16.7	52.4	31.0	50.0	50.0	0.0	35.7	64.3	0.0	18.8	43.8	37.5	28.1	59.4	12.5	31.3	59.4	9.4
10	0.25	0.05	1.5	25.0	81.0	16.7	2.4	83.3	16.7	0.0	95.2	4.8	0.0	87.5	12.5	0.0	96.9	3.1	0.0	90.6	9.4	0.0
11	0.25	0.05	2.5	20.0	78.6	19.0	2.4	83.3	16.7	0.0	92.9	7.1	0.0	87.5	12.5	0.0	96.9	3.1	0.0	90.6	9.4	0.0
12	0.25	0.05	3.5	15.0	78.6	14.3	7.1	81.0	19.0	0.0	90.5	9.5	0.0	87.5	12.5	0.0	96.9	3.1	0.0	90.6	9.4	0.0
13	0.25	0.10	1.5	25.0	66.7	31.0	2.4	76.2	23.8	0.0	88.1	11.9	0.0	75.0	25.0	0.0	87.5	12.5	0.0	87.5	12.5	0.0
14	0.25	0.10	2.5	20.0	64.3	33.3	2.4	76.2	23.8	0.0	85.7	14.3	0.0	78.1	21.9	0.0	90.6	9.4	0.0	87.5	12.5	0.0
15	0.25	0.10	3.5	15.0	59.5	35.7	4.8	76.2	23.8	0.0	78.6	21.4	0.0	75.0	25.0	0.0	90.6	9.4	0.0	84.4	15.6	0.0
16	0.25	0.25	1.5	25.0	21.4	50.0	28.6	52.4	45.2	2.4	38.1	61.9	0.0	21.9	53.1	25.0	56.3	43.8	0.0	40.6	59.4	0.0
17	0.25	0.25	2.5	20.0	21.4	45.2	33.3	47.6	50.0	2.4	38.1	61.9	0.0	21.9	53.1	25.0	56.3	43.8	0.0	40.6	59.4	0.0
18	0.25	0.25	3.5	15.0	11.9	52.4	35.7	42.9	57.1	0.0	33.3	66.7	0.0	18.8	56.3	25.0	53.1	46.9	0.0	40.6	59.4	0.0
19	0.50	0.05	1.5	25.0	61.9	33.3	4.8	71.4	28.6	0.0	85.7	14.3	0.0	75.0	25.0	0.0	84.4	15.6	0.0	87.5	9.4	3.1
20	0.50	0.05	2.5	20.0	59.5	35.7	4.8	69.0	31.0	0.0	83.3	14.3	2.4	75.0	21.9	3.1	87.5	12.5	0.0	84.4	15.6	0.0
21	0.50	0.05	3.5	15.0	54.8	40.5	4.8	66.7	33.3	0.0	83.3	16.7	0.0	71.9	25.0	3.1	87.5	12.5	0.0	81.3	18.8	0.0
22	0.50	0.10	1.5	25.0	54.8	35.7	9.5	66.7	33.3	0.0	76.2	21.4	2.4	65.6	34.4	0.0	87.5	12.5	0.0	75.0	21.9	3.1
23	0.50	0.10	2.5	20.0	52.4	40.5	7.1	64.3	31.0	4.8	73.8	23.8	2.4	59.4	34.4	6.3	81.3	18.8	0.0	71.9	28.1	0.0
24	0.50	0.10	3.5	15.0	45.2	42.9	11.9	61.9	38.1	0.0	69.0	28.6	2.4	59.4	37.5	3.1	84.4	15.6	0.0	68.8	28.1	3.1
25	0.50	0.25	1.5	25.0	21.4	38.1	40.5	42.9	57.1	0.0	35.7	61.9	2.4	18.8	40.6	40.6	46.9	53.1	0.0	31.3	68.8	0.0
26	0.50	0.25	2.5	20.0	21.4	35.7	42.9	40.5	57.1	2.4	35.7	64.3	0.0	21.9	34.4	43.8	40.6	56.3	3.1	34.4	65.6	0.0
27	0.50	0.25	3.5	15.0	16.7	40.5	42.9	35.7	61.9	2.4	33.3	64.3	2.4	21.9	34.4	43.8	43.8	53.1	3.1	31.3	68.8	0.0

selected forms to assign one pit to each mound and one mound to each pit. If one mound had more than one adjacent pit, then we evaluated the distances between the mound and each pit and selected only the closest pit. When the distance was the same, we took into account the area of the pit polygons and selected the largest one. We performed similar analyses for pits having more than one adjacent mound. As a result, we obtained probable locations of pit–mound pairs according to the CM (Fig. 6). To acquire point data for visualization purposes, we extracted the centroid of each pit.

Furthermore, for each research plot, we counted the number of probable locations of pit–mound pairs 1) detected in "on-screen" DEM data analysis and 2) extracted with the use of the two variants of the CM

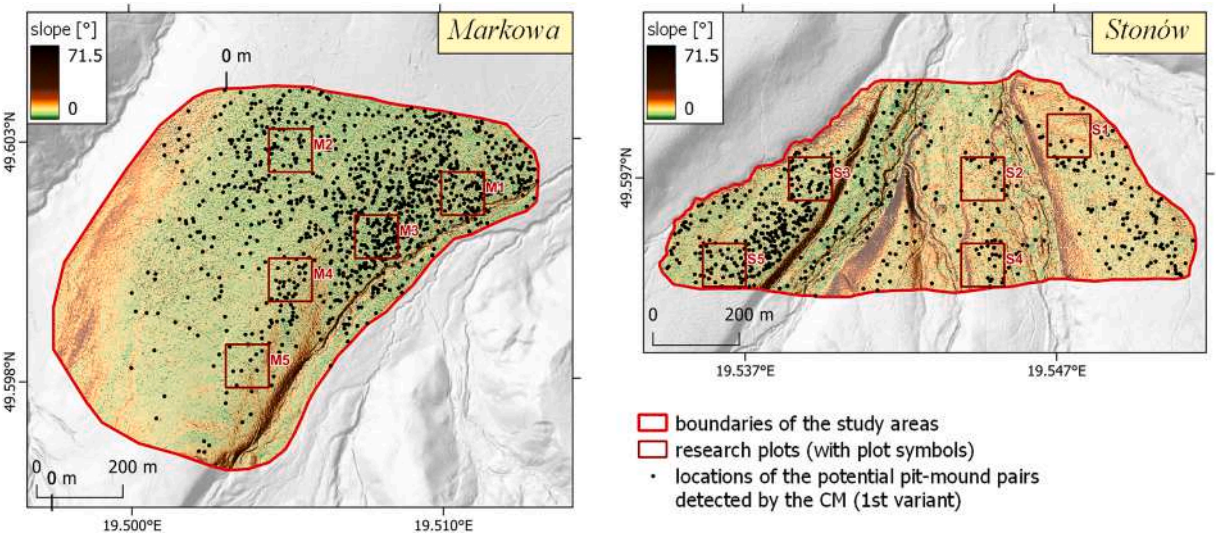

Fig. 6. Spatial distribution of probable locations of the pit–mound pairs on the background of the slope map. The locations were determined on the basis of the 1st variant of the contour method (for details, see Table 1).

(1st and 5th). We determined the intersection of both datasets (matching pit–mound pairs; Table 2). Moreover, for each pit or mound in the "on-screen" validation dataset, we counted the number of CM variants detecting this pit or mound (Fig. 2S, Supplementary Materials). Morphometric statistical parameters (for details, see Table 2) were calculated for each research plot to investigate the relationship between the relief and number of probable locations of pit–mound pairs.

To better understand differences between the number of manually recognized and automatically detected pit–mound pairs within selected research plots, we tested the significance of differences between the individual plots. The testing was based on datasets with extracted values of basic geomorphometric parameters, i.e., WEI, TPI, TWI, TRI, and aspect. The data were extracted from raster layers in a 1x1-m grid. Due to many outliers and the lack of a normal distribution of some parameters (e.g., aspect), we used a nonparametric Kruskal–Wallis test (Hollander and Wolfe, 1973) and a post-hoc Dunn test (Dunn, 1964). For visualization, we used the ggstatsplot R package (Patil, 2021). In addition, the Holm adjusted method for p value for multiple comparisons was used as a default method (Holm, 1979).

4. Results

4.1. Accuracy assessment

Table 1 presents the percentage share of correctly detected, undetected and misrecognized forms for each variant of the CM. The accuracy of the CM was strongly affected by the contour line interval. The best accuracy for the contour line intervals of 0.05 and 0.1 m reached around 90–95 %. For the contour line interval of 0.25 m, the highest accuracy was approximately 45–55 %. DEM resolution also influenced the detection capability of the CM. The greatest CM accuracy, approximately 80–96 %, was achieved for the DEMs with the spatial resolution of 0.1 and 0.25 m. In the case of the DEM with resolution 0.5 m, the CM obtained slightly lower accuracy, reaching a maximum of approximately 60–87 %. It seems that the minimal and maximal lengths of the adopted contour line ranges did not exert a large influence on the accuracy of the CM (Table 1). In the majority of variants, all forms were properly recognized (as pits or as mounds). The highest share of misrecognized forms occurred for the 4th variant in the *Markowa* area, and for the 8th and 9th variants in the *Stonów* area (Table 1).

Generally, we obtained higher CM accuracies for the *Stonów* area than for the *Markowa* area. In the case of *Markowa*, the CM was slightly better in pit recognition in comparison to mound recognition. In the case of *Stonów,* such a relationship was not observed. In most cases, in both study areas, the accuracies computed for pit–mound pairs were significantly lower than the accuracies calculated separately for pits and mounds.

One of the best results were obtained for the 1st variant of the CM (Table 1). In this variant, we used the following variables: a DEM resolution of 0.1 m, contour line interval of 0.05 m and length of contour lines of 1.5–25 m. By applying such parameters, we obtained an accuracy of 96.9 % and 93.8 % for pits and mounds in the *Stonów* area, respectively. In the *Markowa* area, the 1st variant reached an accuracy of 95.2 % for pits and 90.5 % for mounds. For pit–mound pairs, this variant obtained an accuracy of 90.6 % for the *Stonów* area and 85.7 % for the *Markowa* area. Such results were the basis for using the 1st variant of the CM to extract the potential locations of pit–mound pairs at both study sites.

4.2. Spatial distribution and significance in light of forest and hillslope dynamics

The 1st variant of the contour method detected 1030 and 574 probable locations of pit–mound pairs in the *Markowa* and *Stonów* areas, respectively. The density of probable pit–mound pairs per 1 ha reached 16.5 for the *Markowa* area and 12.8 for the *Stonów* area. However, the spatial distribution of the extracted locations was irregular (Fig. 6), which was confirmed by an uneven number of detected forms for different research plots (Table 2). Determined locations tended to occur more frequently on gently sloped areas than on steep slopes. At the *Markowa* site, the majority of locations were situated in the eastern, northeastern and northern parts of the area (Fig. 6). This part of the site was characterized by a relatively gentle slope. In contrast, in the western and southern parts of the *Markowa* area, the slope was steeper. In this part of the site, the CM detected only a few potential locations of pit–mound pairs. A similar situation occurred in the *Stonów* area, where the majority of delineated probable locations were situated in the western, gently sloped part of the site (Fig. 6). In the central and eastern parts of the *Stonów* area, potential locations were distributed quite sparsely.

The forest in the *Markowa* area was damaged by hurricane-force wind (in 1926 or 1936), as opposed to the forest in the *Stonów* area. Trees in the *Stonów* area are much older (between 120 and 130 years old) than those in the *Markowa* area. Young generations of spruces (30 years old) and firs (55 years old) dominate in the *Markowa* area (Forest survey, 2021). In light of this information, we suggest that in the *Stonów* area, pit–mound forms might have been a result of individual tree uprooting under the impact of less devastating wind events. We can expect that pit–mound pairs differ in age. This could be confirmed by radiocarbon dating of the organic matter found in mounds (Embleton-Hamann, 2004; Šamonil et al., 2013), but such dating was not planned for this project. In the *Markowa* area, pit–mound pairs might have been a result of a one stand-replacing event. It is highly probable that the time of their formation was the same; however, they might differ in size due to the size variability of trees that were uprooted during the event.

Table 2
Number of pit–mound pairs per research plot compared to selected morphometric parameters of elevation and slope.

Study area	Research plot symbol	Number of probable locations of pit-mound pairs					Morphometric parameters		
		"On-screen" detection	1st CM variant	Matching ("on-screen" vs 1st CM variant)	5th CM variant	Matching ("on-screen" vs 5th CM variant)	Elevation difference [m]	Standard deviation of slope	Mean slope
Markowa	M1	7	51	6	13	4	13.62	5.71	8.07
	M2	11	28	7	7	6	12.74	3.87	6.92
	M3	10	69	9	27	9	12.23	4.22	6.93
	M4	9	26	9	15	8	17.19	4.88	9.15
	M5	5	8	4	5	3	18.82	3.96	9.1
Stonów	S1	3	6	2	4	3	23.91	5.02	12.38
	S2	4	11	4	5	3	20.28	5.5	11.81
	S3	10	41	10	18	10	15.05	4.74	8.95
	S4	4	16	3	3	3	23.59	6.33	12.73
	S5	11	35	11	17	10	18.62	4.66	9.23

4.3. Research plots and impact of terrain properties

Table 2 shows the number of pit–mound pairs per research plot in comparison to the selected morphometric parameters of elevation and slope. In the "on-screen" validation dataset, the number of pit–mound pairs recognized on particular research plots was uneven. In the *Markowa* area, the greatest number of forms (11) was recognized in the plot M2, while the smallest number (5) was recognized in the plot M5. In the *Stonów* area, the research plot with the highest number of recognized forms (11) was the S5, while the smallest amount of forms (3) was delineated on the plot S1. In the majority of cases, the number of pit–mound pairs detected by the analyzed CM variants was higher or equal to the number of pairs recognized in the "on-screen" DEM analysis. This difference was particularly high in the case of the plots M1, M3, M4, S3 and S5. For the 5th variant of the CM there were only two cases in which the number of extracted probable locations of pit–mound pairs was lower than the number of pairs in the validation dataset while for the 1st variant of the CM there were no such cases. In the *Markowa* area, the 1st variant of the CM detected from 8 (M5) to 69 (M3) pit-mound pairs, while the 5th variant of the CM extracted minimally 5 (M5) and maximally 27 (M3) pit-mound pairs. In the case of the *Stonów* area, the 1st variant of the CM identified from 6 (S1) to 41 (S3) pit-mound pairs, while the 5th variant of the CM delineated from 3 (S4) to 18 (S3) pit–mound pairs. In the *Markowa* area, the value of matching pit–mound forms varied from 4 to 9 for the 1st variant of the CM and from 3 to 9 for the 5th variant of the CM. In the *Stonów* area, the amount of matching pit-mound pairs oscillated within 2–11 for the 1st variant of the CM and 3–10 for the 5th variant of the CM. The majority of pits and mounds were correctly recognized by 12–22 variants of the CM (Fig. 2S, Supplementary Materials). There were also 14 pits and 13 mounds detected by all tested variants of the CM. 3 pits and 4 mounds remained undetected by any of the 27 tested variants. Such forms were more frequent in the *Markowa* area (2 pits, 3 mounds) than in the *Stonów* area (1 pit, 1 mound).

In some cases, the number of detected pit–mound pairs was related to the relief. In the *Stonów* area, the greatest number of detected pit–mound pairs was located in research plots with relatively low elevation differences, low mean slopes and low slope standard deviations. In contrast, research plots with relatively high values of morphometric statistical parameters were characterized by a low number of detected pit–mound pairs. However, this dependence was not clearly visible in the *Markowa* area. The statistical significance of differences in morphometric parameters between the analyzed research plots was confirmed by the nonparametric Kruskal–Wallis test and post-hoc Dum test (for details, see Supplementary Materials). If we consider research plots with a higher difference in detected pit–mound pairs (plots M3, M5, S3 and S4), they differed significantly from each other in terms of several geomorphometric parameters, mainly slope, TRI, TWI, and WEI (Figs. 3S–8S, Supplementary Materials). However, in the *Stonów* area, the difference was not significant for the TRI, and for the TWI, it was significant but only at $p_{adj} = 0.03$. There were no significant differences in terms of the TPI (Fig. 4S), but differences were significant for all plots in terms of the WEI (Fig. 3S, Supplementary Materials).

5. Discussion

5.1. Tree-throw pit–mound topography automatic detection in light of previous attempts of microrelief recognition and mapping

In recent decades, various landforms and microforms have been the subject of detailed investigations and detection. This field of study is a subject of intense research aiming at recognition of, for instance, surficial forms on extraterrestrial objects such as the Moon or the planet Mars (Bue and Stepinski, 2006; Stepinski et al., 2006). However, the task can be even more complex when small-scale forms are the main target of the investigation. Traditionally, these forms were a subject of qualitative evaluation and imprecise mapping on topographic maps at large scales. This approach has been significantly improved since the time when LiDAR point clouds have been easier to access and analyze. Most likely, the most significant step was to obtain submeter resolution DEMs, even for densely vegetated areas. Another step was the invention of many algorithms allowing the calculation of various geomorphometric features, such as the TWI and TPI. (Pike et al., 2008). These terrain parameters led to a better visualization and detection of DEM properties, e. g., flow accumulation, terrain roughness, valley depth, etc. For instance, Mohamed (2020) applied a knowledge-based fuzzy classification method to classify soil-landforms based on terrain attributes derived from DEMs. After classifying landforms into geomorphologic categories, Mohamed (2020) obtained an overall accuracy of 93 %. Ardizzone et al. 2007 showed how an airborne LiDAR survey after heavy rainfall improved the landslide inventory in comparison to traditional techniques (field survey and topographic map interpretation). They were able to detect 27 % more landslides.

Our method is new, written entirely in R, and for the first time, it was applied to the automatic detection of pit–mound topography, which is a unique bioindicator of forest dynamics due to wind disturbances. We were able to reach 80–96 % accuracy when a 0.1-0.25 m DEM was used and 60-87 % accuracy when the method was applied to a 0.5 m DEM. A similar approach based on closed contour lines was used in a limited scope in past studies; moreover, it was applied to other types of landforms, was not fully automated, and was not written in R. Liang and Du (2013); Liang et al. (2014) created a method based on closed contour lines (CCLs) to detect and classify karst landform entities. They used various combinations of closed contours and graph theory (an acyclic graph) to find sinkholes and karst hills and then calculated their surface coverage by these forms. Wu et al. (2015) used a localized contour tree method to extract the locations and properties of complex surface depressions. They used graph theory and a concept of the so-called "pour contour" that marks the boundary of local depressions.

5.2. Factors influencing the accuracy of the CM

The accuracy of the proposed contour method (CM) depends on many factors. Primarily, these factors are 1) the source data and the method of its processing, 2) the applied method of CM validation and 3) the shape of particular pits and mounds.

The output of our analysis is strongly affected by the quality of the LiDAR point clouds. The differentiation of ground reflections can be a challenging task, especially in mountainous areas covered with dense forest. In such areas, the penetrability of laser beams may be affected by the incidence angle (Hsu et al., 2015). For the detection of microtopographic forms, it is extremely important to distinguish between the "ground" and "low vegetation" reflections. The understory vegetation and low-growing branches may cause difficulties in the accurate classification of the point cloud. The LiDAR data applied in this study were processed and classified according to international standards (Wężyk, 2015). However, there still might exist incorrectly classified points, even if the probability of their occurrence seems to be low. There are many methods of ground reflection reclassification (Zhang et al., 2003; Podobnikar and Vrečko, 2012; Pingel et al., 2013; Chen et al., 2017). The "ground" class of LiDAR data is used to produce DEMs. Therefore, to investigate the pit–mound topography, the "ground" class of LiDAR data should be classified as accurately as possible. The kNN-IDW method applied in DEM calculation is effective, widely used and not very time-consuming (Granero and Godone, 2013). However, further investigations may include testing other methods to compare DEMs and choosing the best one. The point cloud density also exerts a significant impact on DEM quality (Agüera-Vega et al., 2020). The density of the applied LiDAR data is 4 points per m^2, which means that for each square meter, there are 4 or more reflections. Such density influences the quality of produced DEMs. Nevertheless, it seems that the impact of point cloud density can be reduced by the interpolation method used

during DEM computation (Agüera-Vega et al., 2020; Cățeanu and Ciubotaru, 2021). When interpolating a source point cloud, changing the resolution of the DEM in most cases does not add more topographic information. The higher spatial resolution of the DEM is connected with the greater complexity of the contour lines, but the overall relief information remains the same or very similar (Fig. 3). Hence, the CM results are mainly affected by the interval of contour lines, and the effect of DEM resolution is quite small (Table 1). Another data processing issue related to the CM is the classification of polygons into pits and mounds. When only one closed contour line is captured by a given feature, the differences in altitude within this contour line may be very small. In such a situation, the *dist_H* and *dist_L* (Fig. 5) can classify convex form as concave one (and oppositely). However, our results indicate that such cases are not frequent (Table 1, "misrecognized" column).

The results of the CM accuracy assessment depend on the quality of the validation dataset. To validate our method, we needed accurate location data of pit–mound pairs. We acquired such a dataset by performing manual, "on-screen" recognition of pits and mounds based on certain visual criteria (for details, see Fig. 2). We selected only these forms, in which we were sure that they represented pit–mound pairs. We decided not to mark adjacent convex–concave forms devoid of the characteristic fit of contour lines. Although this analysis is subjective, we are convinced that its output corresponds to the real locations of pit–mound pairs. A similar method of DEM data analysis was applied in several studies considering forms of anthropogenic origin (Trier and Pilø, 2012; Rutkiewicz et al., 2017; Niculiță, 2020). Such a way of validating may be effective for areas with no or limited access. For detection method improvement, we may need to provide an additional validation dataset with the locations of pit–mound pairs measured by GNSS in the field. Such measurements are planned in the next stage of the analyses. However, the initial tests have shown that the measurement accuracy in the forested areas is below the acceptable level which does not allow the creation of a validation dataset. Another issue is related to the pit-mound pairs from the validation dataset not detected by any of the CM variants. This may be due to the lack of closed contour lines on the pit (or mound), despite of distinct and characteristic fit of contour lines of both forms present in the validation dataset. Another reason can be the occurrence of only one relatively short closed contour line on the form. In such situation, the validation point may fall outside of the closed contour line, and the form may be considered undetected. Regardless of these issues, locations of forms extracted with the use of the CM should always be treated as probable locations of pit-mound pairs.

Generally, the tree-throw pit–mound pairs occur as a particular pattern of the slope microrelief. However, the shape of a given pit–mound pair is influenced by many factors, such as 1) the size of the root-plate of an uprooted tree from which the form arose, 2) the type of soil and bedrock in a given area, 3) the age of the form, and 4) the slope inclination (Schaetzl et al., 1990; Pawlik, 2013; Phillips et al., 2017). Therefore, the pattern of the pit–mound-pair shape is not as regular and repeatable as in the case of human-produced landforms, such as burial mounds, pitfall traps and charcoal kilns. Hence, the development of a method extracting the location of the pit–mound pairs seems to be more difficult than the creation of a method detecting forms of anthropogenic origin. We propose a method that detects pits and mounds at a certain stage of evolution. These forms are characterized by a particular shape, which is detected by our algorithm. Our method is not matched to detect young forms of wind-thrown origin, with undecomposed root plates. However, the CM might detect adjacent convex and concave forms, which can represent old, obliterated pit-mound pairs. Hence, there are a significant number of forms that were detected by the 1st and 5th variants of the CM but were not marked during the 'on-screen' recognition (Table 2). Nevertheless, the 1st and 5th variants of our method detected the majority of pit-mound forms from the validation dataset (Table 2), which may indicate the effectiveness of the CM. Presumably, the CM may also detect different microrelief features not related to pit-mound topography. Frequently the origin of these forms is not obvious and can only be investigated during field surveys. However, tree-throw pit-mound pairs occur very frequently in both study areas so there is a low probability that the CM will detect pits and mounds whose genesis is different than the tree uprooting process.

The best accuracy of the CM obtained for the contour lines with 0.05 m and 0.1 m intervals is strongly related to the shape of pits and mounds in both study areas (Fig. 2and 3). This small interval leads to the occurrence of closed contour lines on more terrain forms and hence enables their detection. In many cases, differences in relative altitude between the top of the mound and the bottom of the pit are below 0.5 m. Therefore, the contour line interval of 0.25 m performs less well at pit–mound pairs detecting.

The slope inclination seems to be very important in the case of CM performance. Presumably, on steep slopes, wind-thrown root-plates tend to evolve into pit–mound pairs with stair-like cross-sections (Šamonil et al., 2010b; Pawlik et al., 2013). This is probably because on steeper slopes, a larger amount of sediment moves downslope of the pit, decreasing the size of the corresponding mound (Gabet et al., 2003; Doane et al., 2021). Moreover, on steeper slopes, mounds deteriorate relatively fast, and pits are filled with organo-mineral material eroded from the upslope area and the rootplate. Furthermore, on steep slopes, the pit rims are inclined and therefore not represented as closed contours when using a horizontal surface reference. For these reasons, on steeper slopes, pit–mound topography might not be distinct enough for detection with the use of closed contours. Presumably, the CM might be able to detect pit-mound pairs on steep slopes if the DEM was produced with the reference to the inclined surface parallel to the slope. However, such an approach would require dividing the study area into sectors with gentle and steep slopes. Nevertheless, this issue can be the subject of future research.

5.3. Potential applications of the CM

The proposed contour method might act as an objective tool to assess the presence of pit–mound topography in a given forest area. This information is very valuable for several reasons.

First, the number and distribution of pit–mound forms seems to be related to the 1) frequency of strong wind occurrence and 2) forest stand properties (species composition, tree height, etc.). Presumably, a high frequency of hurricane wind events results in a larger number of uprooted trees. However, taller trees are more likely to uproot than lower trees. Hence, frequent uprooting of taller trees may cause gradual change in the forest structure toward younger and smaller trees (Gallaway et al., 2009). Therefore, the relationship between wind, forest properties and pit–mound topography formation is quite complex and nonlinear (Constantine et al., 2012). However, the number and distribution of pit–mound pairs may help to reconstruct the history of wind-driven forest disturbances in a particular forest stand. The presence of pit–mound topography can also act as a bioindicator of areas where tree felling occurred in the past (Clinton and Baker, 2000; Strzyżowski et al., 2016).

Second, in mountainous areas, the downslope sediment transport is supported by tree uprooting. Pit–mound topography is the long-term consequence of this geomorphic process. Therefore, the information about the location of pit–mound pairs could be the basis of the modeling of hillslope sediment flux caused by tree-throw. The morphometric parameters needed to estimate the amount of sediment can be obtained from the DEM. Research to date in this field has focused on estimating sediment transport by geomorphological mapping and field measurements of pit–mound pairs (Gallaway et al., 2009; Strzyżowski et al., 2018). Constantine et al. (2012) attempted to simulate sediment transport in connection with the modeling of forest growth dynamics. Doane et al. (2021) extracted several morphometric parameters of pit–mound pairs from LiDAR data. They applied these parameters to develop equations describing the impact of pit–mound topography on

topographic roughness. They created a dimensionless variable as a ratio of the sediment transported due to tree uprooting versus creep-like processes. Then, they measured topographic roughness by calculating the topographic variance of a detrended DEM for slopes on which pit–mound topography was presumably present. Their results showed that topographic variance differs depending on the slope aspect, which is related to the wind directions. Although this approach enables the estimation of hillslope sediment flux due to tree-throw, in some cases, it can be inaccurate due to the presence of other microtopographic forms impacting the topographic roughness, such as forest roads, boulders, and gulleys. Our research plots do not represent flat ground and are rather gently sloped (Table 2). Sediment transport caused by tree uprooting is possible even in case of low inclinations of the slope (Schaetzl et al., 1990). Hence, the presented contour method could be applied to investigate the sediment flux of gentle slopes. Reliable information on the location of pit–mound pairs could improve the accuracy of sediment flux estimation by the extraction of the actual size and volume of forms.

Third, the presence of pit–mound pairs influences soil properties (Putz, 1983; Šamonil et al., 2010a). Therefore, the extraction of pit–mound pair locations may be useful in microscale research on groundcover plant communities in fine-scale mapping. Moreover, some studies have stated that pit–mound forms are better preserved in unmanaged, "old" forests than in managed forests (Barker Plotkin et al., 2017; Phillips et al., 2017). Hence, our method may act as a tool to assess past and current human impacts on a given forest stand. This knowledge can be applied in forest management. Areas with well-developed pit–mound topography may be considered for protection to enable observation of the long-term processes impacting forest ecosystem evolution.

A significant advantage of the contour method is the possibility of performing remote unsupervised detection of pit–mound forms. If good quality LiDAR data are available, the CM can be easily applied to areas with no or limited access. Usage of the CM can also shorten the time needed for fieldwork preparation by providing exact information on the location of particular forms. The proposed method provides an objective assessment of DEMs in terms of pit–mound topography occurrence. Such assessment is faster and less time-consuming in comparison to mapping in the field or "on-screen" recognition of forms. However, the output of the CM may be affected by errors caused by initial data inaccuracy and arguments adapted in several algorithms used during the subsequent phases of the method workflow. Therefore, validation in the field might be necessary in some cases.

The proposed contour method might also have many different applications. In addition to pit–mound pairs, this method could also be applied to detect other microrelief forms, both of natural origin (i.e., termite mounds, mima mounds, landslide peat-bogs, and boulders) and anthropogenic origin (i.e., charcoal kilns, burial mounds and pitfall traps). However, presumably each form type will require an individual approach to adjust the CM to particular characteristic features of a given form type.

6. Conclusions and perspectives

Due to a growing amount of freely accessible and precise spatial data originating from LiDAR surveys, more detailed and large-scale analyses can be conducted in an automated style. This new approach is supported by fast Internet connections enabling sending and receiving large data cubes and more powerful personal computers allowing the performance of more complex operations without costly analytical devices, e.g., multicore servers. LiDAR point clouds are used for digital elevation model construction and its evaluation through more sophisticated geomorphometric algorithms. These models can now be of submeter resolution, which allows in-depth analysis of even small-scale forms or individual boulders. Tree-throw pit–mound pairs are one of the most widespread natural forms considered as bioindicators of forest dynamics due to abiotic disturbances, mostly strong winds. To analyze large segments of forested landscapes, we developed a new unsupervised method of pit–mound topography detection. The method helps to recognize and calculate the density of pit–mound forms that is frequently too difficult or impossible when using conventional methods (field survey, GNSS mapping) in large or inaccessible areas. The method can be used as an important step in different analyses conducted within forest ecology, geomorphology or soil science. It can also be modified and used for the detection of different types of microscale forms (both natural and anthropogenic).

Declaration of Competing Interest

The authors declare that they have no known competing financial interests or personal relationships that could have appeared to influence the work reported in this paper.

Data availability

Data will be made available on request.

Acknowledgements

This study was supported by the Polish National Science Centre – Narodowe Centrum Nauki (grant no. 2019/35/O/ST10/00032). Tomasz Lamorski from Babia Góra National Park is thanked for providing information on the forest history of the selected study areas. An anonymous reviewer is thanked for insightful comments and suggestions that significantly improved the quality of the manuscript.

Appendix A. Supplementary material

Supplementary data to this article can be found online at https://doi.org/10.1016/j.catena.2022.106757. The data include 1) the R script for the contour method automatization and 2) additional figures and plots.

References

Agüera-Vega, F., Agüera-Puntas, M., Martínez-Carricondo, P., Mancini, F., Carvajal, F., 2020. Effects of point cloud density, interpolation method and grid size on derived Digital Terrain Model accuracy at micro topography level. Int. J. Remote Sens. 41, 8281–8299. https://doi.org/10.1080/01431161.2020.1771788.

Ardizzone, F., Cardinali, M., Galli, M., Guzzetti, F., Reichenbach, P., 2007. Identification and mapping of recent rainfall-induced landslides using elevation data collected by airborne Lidar. Natural Hazards and Earth System Sciences 7 (6), 637–650. https://doi.org/10.5194/nhess-7-637-2007.

Barker Plotkin, A., Schoonmaker, P., Leon, B., Foster, D., 2017. Microtopography and ecology of pit-mound structures in second-growth versus old-growth forests. For. Ecol. Manage. 404, 14–23. https://doi.org/10.1016/j.foreco.2017.08.012.

Bue, B.D., Stepinski, T.F., 2006. Machine detection of Martian impact craters from digital topography data. IEEE Transactions on Geoscience and Remote Sensing 45 (1), 265–274. https://doi.org/10.1109/TGRS.2006.885402.

Cățeanu, M., Ciubotaru, A., 2021. The effect of LiDAR sampling density on DTM accuracy for areas with heavy forest cover. Forests 12, 265. https://doi.org/10.3390/f12030265.

Chen, B., Shi, S., Gong, W., Zhang, Q., Yang, J., Du, L., Sun, J., Zhang, Z., Song, S., 2017. Multispectral LiDAR point cloud classification: a two-step approach. Remote Sensing 9, 373. https://doi.org/10.3390/rs9040373.

Clinton, B.D., Baker, C.R., 2000. Catastrophic windthrow in the southern Appalachians: characteristics of pits and mounds and initial vegetation responses. For. Ecol. Manage. 51–60.

Cody, T.R., Anderson, S.L., 2021. LiDAR predictive modeling of Pacific Northwest mound sites: a study of Willamette Valley Kalapuya Mounds, Oregon (USA). J. Archaeolog. Sci.: Rep. 38, 103008 https://doi.org/10.1016/j.jasrep.2021.103008.

Constantine, J.A., Schelhaas, M.-J., Gabet, E., Mudd, S.M., 2012. Limits of windthrow-driven hillslope sediment flux due to varying storm frequency and intensity. Geomorphology 175–176, 66–73. https://doi.org/10.1016/j.geomorph.2012.06.022.

D'hont, B., Calders, K., Bartholomeus, H., Whiteside, T., Bartolo, R., Levick, S., Krishna Moorthy, S.M., Terryn, L., Verbeeck, H., 2021. Characterising termite mounds in a Tropical Savanna with UAV laser scanning. Remote Sensing 13, 476. doi: 10.3390/rs13030476.

Darwin, C., 1881. On the Formation of Vegetable Mould through the Action of Worms. John Murray, London.

Davies, A.B., Levick, S.R., Asner, G.P., Robertson, M.P., van Rensburg, B.J., Parr, C.L., 2014. Spatial variability and abiotic determinants of termite mounds throughout a savanna catchment. Ecography 37, 852–862. https://doi.org/10.1111/ecog.00532.
Davis, D.S., Lipo, C.P., Sanger, M.C., 2019a. A comparison of automated object extraction methods for mound and shell-ring identification in coastal South Carolina. J. Archaeolog. Sci.: Rep. 23, 166–177. https://doi.org/10.1016/j.jasrep.2018.10.035.
Davis, D.S., Sanger, M.C., Lipo, C.P., 2019b. Automated mound detection using lidar and object-based image analysis in Beaufort County, South Carolina. Southeastern Archaeology 38, 23–37. https://doi.org/10.1080/0734578X.2018.1482186.
De Reu, J., Bourgeois, J., Bats, M., Zwertvaegher, A., Gelorini, V., De Smedt, P., Chu, W., Antrop, M., De Maeyer, P., Finke, P., Van Meirvenne, M., Verniers, J., Crombé, P., 2013. Application of the topographic position index to heterogeneous landscapes. Geomorphology 186, 39–49. https://doi.org/10.1016/j.geomorph.2012.12.015.
Detailed Geological Map of Poland, 2019. Sheet: Zawoja (1031). National Geological Institute – National Research Institute, Warsaw. https://geolog.pgi.gov.pl/#name=kob30dg043 (Accessed on 29 March 2022).
Doane, T.H., Edmonds, D., Yanites, B.J., Lewis, Q., 2021. Topographic roughness on forested hillslopes: A theoretical approach for quantifying hillslope sediment flux from tree throw. Geophys. Res. Lett. 48 https://doi.org/10.1029/2021GL094987.
Dunn, O.J., 1964. Multiple comparisons using rank sums. Technometrics 6, 241–252. https://doi.org/10.1080/00401706.1964.10490181.
Dyderski, M.K., Pawlik, Ł., 2021. Drivers of forest aboveground biomass and its increments in the Tatra Mountains after 15 years. Catena 205, 105468. https://doi.org/10.1016/j.catena.2021.105468.
Embleton-Hamann, C., 2004. Processes responsible for the development of a pit and mound microrelief. Catena 57, 175–188. https://doi.org/10.1016/j.catena.2003.10.017.
Evans, J.S., 2021. spatialEco. R package version 1.3-6. https://github.com/jeffreyevans/spatialEco.
Forest Survey, 2021. Babia Góra National Park Forest Database, unpublished data available at the Babia Góra NP Directorate, Zawoja, Poland.
Freeland, T., Heung, B., Burley, D.V., Clark, G., Knudby, A., 2016. Automated feature extraction for prospection and analysis of monumental earthworks from aerial LiDAR in the Kingdom of Tonga. J. Archaeol. Sci. 69, 64–74. https://doi.org/10.1016/j.jas.2016.04.011.
Gabet, E.J., Reichman, O.J., Seabloom, E.W., 2003. The effects of bioturbation on soil processes and sediment transport. Annu. Rev. Earth Planet. Sci. 31, 249–273. https://doi.org/10.1146/annurev.earth.31.100901.141314.
Gabet, E.J., Perron, J.T., Johnson, D.L., 2014. Biotic origin for Mima mounds supported by numerical modeling. Geomorphology 206, 58–66. https://doi.org/10.1016/j.geomorph.2013.09.018.
Gallaway, J.M., Martin, Y.E., Johnson, E.A., 2009. Sediment transport due to tree root throw: integrating tree population dynamics, wildfire and geomorphic response. Earth Surf. Proc. Land. 34, 1255–1269. https://doi.org/10.1002/esp.1813.
Geoportal, 2022. Data to download - DEM measurment data (LiDAR point cloud). Retrieved in October 2021. https://mapy.geoportal.gov.pl/imap/Imgp_2.html.
Granero, G., Godone, D., 2013. Comparisons between different interpolation techniques. Int. Arch. Photogram. Remote Sens. Spat. Inf. Sci. XL-5/W3, 139–144. https://doi.org/10.5194/isprsarchives-XL-5-W3-139-2013.
Guyot, A., Hubert-Moy, L., Lorho, T., 2018. Detecting neolithic burial mounds from LiDAR-derived elevation data using a multi-scale approach and machine learning techniques. Remote Sensing 10, 225. https://doi.org/10.3390/rs10020225.
Hellmer, M.C., Rios, B.A., Ouimet, W.B., Sibley, T.R., 2015. Ice storms, tree throw, and hillslope sediment transport in northern hardwood forests: sediment transport by tree throw during icestorms in temperate forests. Earth Surf. Proc. Land. 40, 901–912. https://doi.org/10.1002/esp.3690.
Holeksa, J., Woźniak, G., 2005. Biased vegetation patterns and detection of vegetation changes using phytosociological databases. a case study in the forests of the Babia Gora National Park (the West Carpathians, Poland). Phytocoenologia 35, 1–18. https://doi.org/10.1127/0340-269X/2005/0035-0001.
Hollander, M., Wolfe, D.A., 1973. Nonparametric Statistical Methods. John Wiley & Sons, New York, pp. 115–120.
Holm, S., 1979. A simple sequentially rejective multiple test procedure. Scand. J. Stat. 6, 65–70.
Howey, M.C.L., Sullivan, F.B., Tallant, J., Kopple, R.V., Palace, M.W., 2016. Detecting precontact anthropogenic microtopographic features in a forested landscape with Lidar: a case study from the Upper Great Lakes Region, AD 1000–1600. PLoS ONE 11, 1–11. https://doi.org/10.1371/journal.pone.0162062.
Hsu, W.-C., Shih, P.-T.-Y., Chang, H.-C., Liu, J.-K., 2015. A study on factors affecting airborne LiDAR penetration. Terrestrial Atmos. Oceanic Sci. 26, 241. https://doi.org/10.3319/TAO.2014.12.02.08(EOSI).
IMWM - NRI – Institute of Meteorology and Water Management – National Research Institute, 2022. Meteorological survey – observational data. https://dane.imgw.pl/data/dane_pomiarowo_obserwacyjne/dane_meteorologiczne/.
Jane, G.T., 1986. Wind damage as an ecological process in mountain beech forests of Canterbury, New Zealand. N. Z. J. Ecol. 9, 25–39.
Kooch, Y., Hosseini, S.M., Mohammadi, J., Hojjati, S., 2012. Effects of uprooting tree on herbaceous species diversity, woody species regeneration status and soil physical characteristics in a temperate mixed forest of Iran. J. For. Res. 23 https://doi.org/10.1007/s11676-012-0236-6.
Kooch, Y., Zaccone, C., Lamersdorf, N.P., Tonon, G., 2014. Pit and mound influence on soil features in an Oriental Beech (*Fagus orientalis* Lipsky) forest. Eur. J. Forest Res. 133, 347–354. https://doi.org/10.1007/s10342-013-0766-2.
Książkiewicz, M., 1971. Explanations for the Detailed Geological Map of Poland 1:50 000. Sheet Zawoja (1031). Geological Publishing House, Warsaw. http://bazadata.pgi.gov.pl/data/smgp/arkusze_txt/smgp1031.pdf (In Polish).
Liang, F., Du, Y., 2013. An automated method to extract typical karst landform entities from contour lines on topographic maps. Proc. Geomorphometry 46–49.
Liang, F., Du, Y., Ge, Y., Li, C., 2014. A quantitative morphometric comparison of cockpit and doline karst landforms. J. Geogr. Sci. 24, 1069–1082. https://doi.org/10.1007/s11442-014-1139-6.
Liechty, H.O., Jurgensen, M.F., Mroz, G.D., Gale, M.R., 1997. Pit and mound topography and its influence on storage of carbon, nitrogen, and organic matter within an old-growth forest. Can. J. For. Res. 27, 1992–1997. https://doi.org/10.1139/x97-168.
Lyford, W.H., 1966. Mound and pit microrelief in relation to soil disturbance and tree distribution in New Brunswick, Canada. Harvard Forest Paper 15, 1–18.
Meng, X., Kooijman, A.M., Temme, A.J.A.M., Cammeraat, E.L.H., 2022. The current and future role of biota in soil-landscape evolution models. Earth Sci. Rev. 226, 103945 https://doi.org/10.1016/j.earscirev.2022.103945.
Meyer, M.F., Pfeffer, I., Jürgens, C., 2019. Automated detection of field monuments in digital terrain models of Westphalia using OBIA. Geosciences 9, 109. https://doi.org/10.3390/geosciences9030109.
Mohamed, M., 2020. Classification of landforms for digital soil mapping in urban areas using LiDAR data derived terrain attributes: A case study from Berlin, Germany. Land 9, 319. https://doi.org/10.3390/land9090319.
Moore, I.D., Grayson, R.B., Ladson, A.R., 1991. Digital terrain modelling: A review of hydrological, geomorphological, and biological applications. Hydrol. Process. 5, 3–30. https://doi.org/10.1002/hyp.3360050103.
Niculiță, M., 2020. Geomorphometric methods for burial mound recognition and extraction from high-resolution LiDAR DEMs. Sensors 20, 1192. https://doi.org/10.3390/s20041192.
Ocko, S.A., Heyde, A., Mahadevan, L., 2019. Morphogenesis of termite mounds. Proc. Natl. Acad. Sci. 116, 3379–3384. doi: 10.1073/pnas.1818759116.
Patil, I., 2021. Visualizations with statistical details: the "ggstatsplot" approach. J. Open Source Software 6, 3167. doi: 10.21105/joss.03167.
Pawlik, Ł., 2013. The role of trees in the geomorphic system of forested hillslopes — a review. Earth Sci. Rev. 126, 250–265. https://doi.org/10.1016/j.earscirev.2013.08.007.
Pawlik, Ł., Harrison, S.P., 2022. Modelling and prediction of wind damage in forest ecosystems of the Sudety Mountains, SW Poland. Sci. Total Environ. 815, 151972 https://doi.org/10.1016/j.scitotenv.2021.151972.
Pawlik, Ł., Kasprzak, M., 2015. Electrical resistivity tomography (ERT) of pit-and-mound microrelief, Mt Rogowa Kopa case study, the Stołowe Mountains, SW Poland. Landform Analysis 29, 41–47. https://doi.org/10.12657/landfana.029.006.
Pawlik, Ł., Kasprzak, M., 2018. Regolith properties under trees and the biomechanical effects caused by tree root systems as recognized by electrical resistivity tomography (ERT). Geomorphology 300, 1–12. https://doi.org/10.1016/j.geomorph.2017.10.002.
Pawlik, Ł., Migoń, P., Owczarek, P., Kacprzak, A., 2013. Surface processes and interactions with forest vegetation on a steep mudstone slope, Stołowe Mountains, SW Poland. Catena 109, 203–216. https://doi.org/10.1016/j.catena.2013.03.011.
Pawlik, Ł., Migoń, P., Szymanowski, M., 2016. Local-and regional-scale biomorphodynamics due to tree uprooting in semi-natural and managed montane forests of the Sudetes Mountains, Central Europe. Earth Surface Processes and Landforms 41 (9), 1250–1265. https://doi.org/10.1002/esp.3950.
Pawlik, Ł., Musielok, Ł., Migoń, P., Wrońska-Wałach, D., Duszyński, F., Kasprzak, M., 2017. Deciphering the history of forest disturbance and its effects on landforms and soils – lessons from a pit-and-mound locality at Rogowa Kopa, Sudetes, SW Poland. Bull. Geogr. Phys. Geogr. Ser. 12, 59–81. https://doi.org/10.1515/bgeo-2017-0006.
Pawlik, Ł., Samonil, P., Malik, I., Kroh, P., Ślęzak, A., Daněk, P., 2019. Geomorphic edge effects in response to abiotic and anthropogenic disturbances in forest ecosystems of the Gorce Mountains, Western Carpathians. Catena 177, 134–148. https://doi.org/10.1016/j.catena.2019.02.013.
Phillips, J.D., Marion, D.A., Turkington, A.V., 2008. Pedologic and geomorphic impacts of a tornado blowdown event in a mixed pine-hardwood forest. Catena 75, 278–287. https://doi.org/10.1016/j.catena.2008.07.004.
Phillips, J.D., Šamonil, P., Pawlik, Ł., Trochta, J., Daněk, P., 2017. Domination of hillslope denudation by tree uprooting in an old-growth forest. Geomorphology 276, 27–36. https://doi.org/10.1016/j.geomorph.2016.10.006.
Pingel, T.J., Clarke, K.C., McBride, W.A., 2013. An improved simple morphological filter for the terrain classification of airborne LIDAR data. ISPRS J. Photogramm. Remote Sens. 77, 21–30. https://doi.org/10.1016/j.isprsjprs.2012.12.002.
Podobnikar, T., Vrečko, A., 2012. Digital elevation model from the best results of different filtering of a LiDAR point cloud: high quality DEM from LiDAR data. Trans. GIS 16, 603–617. https://doi.org/10.1111/j.1467-9671.2012.01335.x.
Putz, F.E., 1983. Treefall pits and mounds, buried seeds, and the importance of soil disturbance to pioneer trees on Barro Colorado Island, Panama. Ecology 64, 1069–1074. https://doi.org/10.2307/1937815.
Riley, S.J., DeGloria, S.D., Elliot, R., 1999. A terrain ruggedness index that quantifies topographic heterogeneity. Int. J. Sci. 5 (1–4), 23–27.
Pike, R.J., Evans, I.S., Hengl, T., 2008.Geomorphometry: a Brief Guide. In: Hengl, T. and Reuter, H.I. (Eds.), Geomorphometry: Concepts, Software, Applications. Developments in Soil Science, Vol. 33. Elsevier, pp. 1–28. doi: 10.1016/S0166-2481(08)00001-9.
Riley, M.A., 2009. Date Automated Detection of Prehistoric Conical Burial Mounds From LIDAR Bare-Earth Digital Elevation Models. Northwest Missouri State University Maryville, Maryville, MO, USA (Master thesis).
Roussel, J.-R., Auty, D., Coops, N.C., Tompalski, P., Goodbody, T.R.H., Meador, A.S., Bourdon, J.-F., de Boissieu, F., Achim, A., 2020. lidR: An R package for analysis of

Airborne Laser Scanning (ALS) data. Remote Sens. Environ. 251, 112061 https://doi.org/10.1016/j.rse.2020.112061.
Rutkiewicz, P., Malik, I., Wistuba, M., Sady, A., 2017. Charcoal kilns as a source of data on the past iron industry (an example from the River Czarna valley, Central Poland). Environ. Socio-economic Stud. 5, 12–22. https://doi.org/10.1515/environ-2017-0012.
Šamonil, P., Antolík, L., Svoboda, M., Adam, D., 2009. Dynamics of windthrow events in a natural fir-beech forest in the Carpathian mountains. For. Ecol. Manage. 257, 1148–1156. https://doi.org/10.1016/j.foreco.2008.11.024.
Šamonil, P., Král, K., Hort, L., 2010a. The role of tree uprooting in soil formation: a critical literature review. Geoderma 157, 65–79. https://doi.org/10.1016/j.geoderma.2010.03.018.
Šamonil, P., Tejnecký, V., Borůvka, L., Šebková, B., Janík, D., Šebek, O., 2010b. The role of tree uprooting in Cambisol development. Geoderma 159, 83–98. https://doi.org/10.1016/j.geoderma.2010.06.020.
Šamonil, P., Schaetzl, R.J., Valtera, M., Goliáš, V., Baldrian, P., Vašíčková, I., Adam, D., Janík, D., Hort, L., 2013. Crossdating of disturbances by tree uprooting: can treethrow microtopography persist for 6000 years? For. Ecol. Manage. 307, 123–135. https://doi.org/10.1016/j.foreco.2013.06.045.
Šamonil, P., Valtera, M., Schaetzl, R.J., Adam, D., Vašíčková, I., Daněk, P., Janík, D., Tejnecký, V., 2016. Impacts of old, comparatively stable, treethrow microtopography on soils and forest dynamics in the northern hardwoods of Michigan, USA. Catena 140, 55–65. https://doi.org/10.1016/j.catena.2016.01.006.
Schaetzl, R.J., Johnson, D.L., Burns, S.F., Small, T.W., 1989. Tree uprooting: review of terminology, process, and environmental implications. Can. J. For. Res. https://doi.org/10.1139/x89-001.
Schaetzl, R.J., Burns, S.F., Small, T.W., Johnson, D.L., 1990. Tree uprooting: review of types and patterns of soil disturbance. Phys. Geogr. 11, 277–291. https://doi.org/10.1080/02723646.1990.10642407.
Schaetzl, R.J., Follmer, L.R., 1990. Longevity of treethrow microtopography: implications for mass wasting. Geomorphology 3, 113–123. https://doi.org/10.1016/0169-555X(90)90040-W.
Schelhaas, M.-J., Nabuurs, G.-J., Schuck, A., 2003. Natural disturbances in the European forests in the 19th and 20th centuries. Glob. Change Biol. 9, 1620–1633. https://doi.org/10.1046/j.1365-2486.2003.00684.x.
Schneider, A., Takla, M., Nicolay, A., Raab, A., Raab, T., 2015. A template-matching approach combining morphometric variables for automated mapping of charcoal kiln sites. Archaeological Prospection 22, 45–62. https://doi.org/10.1002/arp.1497.
Skentos, A., 2017. Topographic Position Index based landform analysis of Messaria (Ikaria Island, Greece). Acta Geobalcanica 4, 7–15. doi: 10.18509/AGB.2018.01.
Stepinski, T.F., Ghosh, S., Vilalta, R., 2006. Automatic recognition of landforms on Mars using terrain segmentation and classification. In: Todorovski, L., Lavrač, N., Jantke, K.P. (Eds.), Discovery Science, Lecture Notes in Computer Science. Springer Berlin Heidelberg, Berlin, Heidelberg, pp. 255–266. doi: 10.1007/11893318_26.
Strzyżowski, D., Fidelus, J., Żelazny, M., 2016. Geomorphological changes within a hillslope caused by a windthrow event in the Tatra Mountains, southern Poland. Geografiska Annaler: Ser. A, Phys. Geogr. 98, 347–360. https://doi.org/10.1111/geoa.12141.
Strzyżowski, D., Fidelus-Orzechowska, J., Żelazny, M., 2018. Sediment transport by uprooting in the forested part of the Tatra Mountains, southern Poland. Catena 160, 329–338. https://doi.org/10.1016/j.catena.2017.09.019.
Tarolli, P., Sofia, G., Calligaro, S., Prosdocimi, M., Preti, F., Dalla Fontana, G., 2015. Vineyards in terraced landscapes: new opportunities from Lidar data. Land Degrad. Dev. 26, 92–102. https://doi.org/10.1002/ldr.2311.
Trepińska, J., Kowanetz, L., 2000. Dependence of wind direction and speed on the topography in the western part of the Beskidy Mountains. Prace Geograficzne 105, 165–182.
Trier, Ø.D., Pilø, L.H., 2012. Automatic detection of pit structures in airborne laser scanning data: automatic detection of pits in ALS data. Archaeol. Prospect. 19, 103–121. https://doi.org/10.1002/arp.1421.
Trier, Ø.D., Cowley, D.C., Waldeland, A.U., 2019. Using deep neural networks on airborne laser scanning data: results from a case study of semi-automatic mapping of archaeological topography on Arran, Scotland. Archaeol. Prospect. 26, 165–175. https://doi.org/10.1002/arp.1731.
Ulanova, N.G., 2000. The effects of windthrow on forests at different spatial scales: a review. For. Ecol. Manage. 135.
Valtera, M., Schaetzl, R.J., 2017. Pit-mound microrelief in forest soils: review of implications for water retention and hydrologic modelling. For. Ecol. Manage. 393, 40–51. https://doi.org/10.1016/j.foreco.2017.02.048.
Wężyk, P. (Ed.), 2015. Podręcznik dla uczestników szkoleń z wykorzystania produktów LiDAR. Główny Urząd Geodezji i Kartografii, Warszawa (In Polish). http://www.gugik.gov.pl/_data/assets/pdf_file/0019/23752/PODRECZNIK_ISOK_wyd.2.pdf.
Wu, Q., Liu, H., Wang, S., Yu, B., Beck, R., Hinkel, K., 2015. A localized contour tree method for deriving geometric and topological properties of complex surface depressions based on high-resolution topographical data. Int. J. Geogr. Inf. Sci. 29, 2041–2060. https://doi.org/10.1080/13658816.2015.1038719.
Wypych, A., Ustrnul, Z., Schmatz, D.R., 2018. Long-term variability of air temperature and precipitation conditions in the Polish Carpathians. J. Mountain Sci. 15, 237–253. https://doi.org/10.1007/s11629-017-4374-3.
Zhang, K., Chen, S.-C., Whitman, D., Shyu, M.-L., Yan, J., Zhang, C., 2003. A progressive morphological filter for removing nonground measurements from airborne LIDAR data. IEEE Trans. Geosci. Remote Sens. 41, 872–882. https://doi.org/10.1109/TGRS.2003.810682.

Załącznik nr 9
do pisma okólnego nr 2
Prorektora ds. nauki i finansów
z dnia 19 lutego 2024 r.

Sosnowiec, 06-08-2025 r.
miejscowość, data

...Janusz Godziek.....
imię i nazwisko kandydata

OŚWIADCZENIE OSOBY UBIEGAJĄCEJ SIĘ O WŁASNYM WKŁADZIE W POWSTAWANIE PRACY

Oświadczam, że w pracy:

Godziek J., Pawlik Ł., Buma B., 2025: The Mapping and Analysis of the Infrequent, Large-Scale Blowdown Event in the Colorado Front Range. Land Degradation & Development, 36(10), 3604-3620. https://doi.org/10.1002/ldr.5623

(autorzy, rok wydania, tytuł, czasopismo lub wydawca, tom, strony)

mój udział polegał na zastosowaniu metody analizy wektorów zmian (changevectoranalysis, CVA) do kartowania wiatrowałów powstałych we wrześniu 2020 r. w Górach Skalistych w Kolorado z wykorzystaniem zdjęć satelitarnych Sentinel 2, automatyzacji ww. analiz poprzez utworzenie skryptu w języku programowania R (załącznik do artykułu), analizie danych meteorologicznych dotyczących epizodu wiatrowego który spowodował powstanie badanych wiatrowałów,prowadzeniu prac terenowych - pomiarów wykrotów, pisaniu całości tekstu artykułu (poza częścią dyskusji), przygotowaniu wszystkich rycin do artykułu.

Janusz Godziek
.....
podpis

Załącznik nr 9
do pisma okólnego nr 2
Prorektora ds. nauki i finansów
z dnia 19 lutego 2024 r.

Sosnowiec, 06-08-2025 r.
miejscowość, data

...Janusz Godziek.....
imię i nazwisko kandydata

OŚWIADCZENIE OSOBY UBIEGAJĄCEJ SIĘ O WŁASNYM WKŁADZIE W POWSTAWANIE PRACY

Oświadczam, że w pracy:

Godziek J., 2024: Root plates of uprooted trees– Automatic detection and biotransport estimation using LiDAR data and field mapping. International Journal of Applied Earth Observation and Geoinformation, 131, 103992. https://doi.org/10.1016/10.1016/j.jag.2024.103992

(autorzy, rok wydania, tytuł, czasopismo lub wydawca, tom, strony)

mój udział polegał na opracowaniu i testowaniu metody wykrywania wykrotów w oparciu o dane LiDAR oraz ich pochodne (numeryczne modele terenu, numeryczne modele pokrycia terenu), automatyzacji ww. metody poprzez utworzenie skryptu w języku programowania R (załącznik do artykułu),prowadzeniu prac terenowych - pomiarów wykrotów, pisaniu całości tekstu artykułu, przygotowaniu wszystkich rycin do artykułu.

Janusz Godziek
.....
podpis

Załącznik nr 9
do pisma okólnego nr 2
Prorektora ds. nauki i finansów
z dnia 19 lutego 2024 r.

Sosnowiec, 06-08-2025 r.
miejscowość, data

...Janusz Godziek.....
imię i nazwisko kandydata

OŚWIADCZENIE OSOBY UBIEGAJĄCEJ SIĘ O WŁASNYM WKŁADZIE W POWSTAWANIE PRACY

Oświadczam, że w pracy:

Godziek J., Pawlik Ł. 2023: Indicators of wind-driven forest disturbances–pit–mound topography, its automatic detection and significance. Catena, 221, 106757. https://doi.org/10.1016/j.catena.2022.106757

(autorzy, rok wydania, tytuł, czasopismo lub wydawca, tom, strony)

mój udział polegał na opracowaniu i testowaniu metody wykrywania topografii kopców i zagłębień w oparciu o wysokorozdzielcze numeryczne modele terenu utworzone w oparciu o dane LiDAR, automatyzacji ww. metody poprzez utworzenie skryptu w języku programowania R (załącznik do artykułu), pisaniu tekstu artykułu (cały tekst poza częścią rozdziału 2), przygotowaniu rycin do artykułu.

Janusz Godziek
.....
podpis

A STATEMENT OF THE APPLICANT'S CO-AUTHOR OF THEIR CONTRIBUTION TO THE WORK

Boulder, U.S, date 14 May 2025

Brian Buma, PhD

University of Colorado Denver
Associate Professor of Research

Department of Integrative Biology

STATEMENT

I declare that for the following work:

Godziek J., Pawlik Ł., Buma B., 2025: The Mapping and Analysis of the Infrequent, Large-Scale Blowdown Event in the Colorado Front Range. Land Degradation & Development. https://doi.org/10.1002/ldr.5623

My participation consisted of identifying and facilitating research site identification and access, helping design the study in terms of fieldwork and statistical analysis, and editing and providing comments on the writing and publication process. I had an advisory role throughout the project which was led by Janusz Godziek.

.....

Signature of the co-author of the publication

*applies to co-authors

Załącznik nr 10
do pisma okólnego nr 2
Prorektora ds. nauki i finansów
z dnia 19 lutego 2024 r.

OŚWIADCZENIE

WSPÓŁAUTORA OSOBY UBIEGAJĄCEJ SIĘ O WŁASNYM WKŁADZIE W POWSTAWANIE PRACY

Miejsce Sosnowiec, dnia 30-05-2025 r.

Łukasz Pawlik
Imię i nazwisko współautora publikacji

Uniwersytet Śląski,
Wydział Nauk Przyrodniczych,
Instytut Nauk o Ziemi
Afiliacja

OŚWIADCZENIE

Oświadczam, że w pracy:

Godziek J., Pawlik Ł., Buma B., 2025: The Mapping and Analysis of the Infrequent, Large-Scale Blowdown Event in the Colorado Front Range. Land Degradation & Development.

Mój udział polegał na edycji całego tekstu, wkładu w pisaniu części tekstu do dyskusji, oraz kierowaniu projektem naukowym obejmującym badania opisane w tej pracy.

Łukasz Pawlik
.....

Podpis współautora publikacji

Załącznik nr 10
do pisma okólnego nr 2
Prorektora ds. nauki i finansów
z dnia 19 lutego 2024 r.

OŚWIADCZENIE

WSPÓŁAUTORA OSOBY UBIEGAJĄCEJ SIĘ O WŁASNYM WKŁADZIE W POWSTAWANIE PRACY

Miejsce Sosnowiec, dnia 30-05-2025 r.

Łukasz Pawlik
Imię i nazwisko współautora publikacji

Uniwersytet Śląski,
Wydział Nauk Przyrodniczych,
Instytut Nauk o Ziemi
Afiliacja

OŚWIADCZENIE

Oświadczam, że w pracy:

Godziek J., Pawlik Ł. 2023: Indicators of wind-driven forest disturbances–pit–mound topography, its automatic detection and significance. Catena, 221, 106757. https://doi.org/10.1016/j.catena.2022.106757

Mój udział polegał na wykonaniu testów statystycznych zmiennych terenowych (ryciny znajdują się w materiałach dodatkowych do artykułu), edycji tekstu wstępu, edycji i pisaniu części tekstu rozdziału 2, edycji i pisaniu części tekstu dyskusji, oraz kierowaniu projektem naukowym obejmującym badania opisane w tej pracy.

Łukasz Pawlik
.....

Podpis współautora publikacji